



ScuDo

Scuola di Dottorato ~ Doctoral School
WHAT YOU ARE, TAKES YOU FAR



Doctoral Dissertation
Doctoral Program in Electrical, Electronics and Communications Engineering
(33th Cycle)

A novel electrical conductive resin for stereolithographic 3D printing

Giorgio Scordo

Supervisors

Prof. C.F. Pirri
Prof. M. Cocuzza

Doctoral Examination Committee:

Prof.
Prof.
Prof.

Politecnico di Torino
April, 2021

Per Aspera Ad Astra

.....
Giorgio Scordo
Turin, April, 2021

Summary

Additive manufacturing (AM) or 3D printing, is a three-dimensional fabrication technique in which a model designed by Computer Aided Design (CAD) is built layer-by-layer. The fabrication technologies based on AM are able to make complex geometries that cannot be created using traditional manufacturing process (i.e., forging, injection molding, etc.).

Nowadays scientific and industrial applications on 3D printing is rapidly growing up and, in parallel, is increasing the interest to develop novel printable materials especially for stereolithography (SL). The SL resins are epoxy or acrylate based monomers/oligomers, which undergo a cationic or radical photopolymerization. Inside those resins some fillers, e.g. carbon or silver nanoparticles, metal powders or composite polymers, are added to increase the electrical conductive properties.

One of the most employed conductive polymers, which registered great interest in recent years, is the poly(3,4-ethylenedioxythiophene):poly(styrenesulfonate) PEDOT:PSS called CleviosTM PH1000. Its optical transparency, tuneable electrical conductivity and high flexibility, make this copolymer one of the most used from energy storage devices to electrochemical sensors. In this work, an electrically conductive resin based on acrylate matrix was developed, studied and characterized using the PEDOT:PSS particles precipitated from CleviosTM PH1000.

First steps consisted in understanding the composition of the CleviosTM PH1000, and the possibilities to remove the PSS group using different treatments. Afterward, the dispersion of the PEDOT:PSS particles inside a Poly(ethylene glycol) diacrylate (PEGDA) resin was optimized and the surfactant and

PEDOT:PSS concentration to achieve a stable conductive resin for SL was studied.

The main part of the PhD research activity was dedicated to characterize the PEGDA:PEDOT resin and explore the possible applications in energy storage devices, gas sensing and finally for cell culture devices.

The PhD research activity on High Performance & Smart Manufacturing has been held at the Materials and MicroSystems Laboratory of Politecnico di Torino (ChiLab).

Contents

1. Additive manufacturing	1
1.1 Introduction.....	1
1.2 Additive Manufacturing technologies	1
1.3 Additive Manufacturing applications in micro&nanofabrication	4
1.4 Light-cured printers	4
2. Photopolymers	8
2.1 Introduction.....	8
2.2 Photopolymerization	9
2.3 Conductive polymer.....	10
2.4 PEDOT:PSS.....	11
2.5 Photocurable conductive resin	12
3. PEGDA:PEDOT conductive resin.....	14
3.1 Stereolithography printing machine.....	14
3.2 Photoinitiator concentration.....	16
3.3 Electrical measurement setup	18
3.4 Filler preparation.....	19
3.5 Suspension study.....	21
3.6 Percolation threshold	23
3.7 Fourier transform infrared spectroscopy analysis.....	25
3.8 RAMAN spectroscopy.....	27
3.9 Field emission scanning electron microscope characterization	31
3.10 Printing parameters optimization.....	33
3.11 Mechanical characterization	35
3.12 Contact Angle	38
3.13 In vitro cell tests.....	40
4. Effect of volatile organic compounds adsorption on 3D printed PEGDA:PEDOT for long-term monitoring devices.....	44
4.1 Introduction.....	44
4.2 CMD fabrication.....	45
4.3 Results.....	46

5. Organic Electrochemical Transistors based on PEGDA 575 and treated PEDOT:PSS.....	53
5.1 Introduction.....	53
5.2 3D OECT Fabrication.....	54
5.3 Results.....	56
6. 3D Printed energy storage device based on PEGDA and treated PEDOT:PSS blend.....	58
6.1 Introduction.....	58
6.2 3D Print device	59
6.3 Results.....	62
7. Conclusions.....	66
8. References.....	70

List of Tables

Table 1: Relevant optical characteristics of selected galvanometric scanner are reported

Table 2: Pattern test on PEGDA 575 with 1% wt. of PI, 5% wt. of DMSO and 45% wt. of treated PEDOT:PSS

Table 3: State-of-the-art of 3D-printed cumulative adsorption materials for acetone and ethanol vapor. TPU: thermoplastic polyurethane polymer; PC: polycarbonate; PEDOT:PSS: poly(3,4-ethylenedioxythiophene) polystyrene sulfonate; PVDF: poly(vinylidene fluoride); MWCNT: multi-walled carbon nanotubes; rGO: graphene oxide; CNFs: carbon nanofibers; FDM: fused deposition modeling; SL: stereolithography.

List of Figures

Figure 1: Classification of AM processes.[14].....	2
Figure 2: Vat photopolymerization: a) DLP in which a layer of resin is cured by a pattern generated using a projector, b) and SL where the pattern is produced by a scanning laser beam.	5
Figure 3: The first SL system launched in 1987.[41].....	5
Figure 4: Flow chart of the stereolithography building process.[40].....	6
Figure 5: Customised SLA printing machine: A) SLA mechanical system, B) SLA components. C) SLA printer completed enclosure.	15
Figure 6: Synthesis routes, nanospheres, nanoplates, nanoprisms, nanorods.[56].....	9
Figure 7: A) Thiophene chemical structure. B) PEDOT:PSS chemical structure	12
Figure 8: PEGDA 575 with 1, 0.5, 0.1, 0.01 % wt. of photoinitiator from right to left.....	17
Figure 9: Young modulus of PEGDA 575 with different PI concentrations. .	18
Figure 10: A) PDMS mold for samples preparation. B) PEGDA 575 with 1% wt. PI samples and 5 min under UV light (365 nm) C) PEGDA with 35% wt. of treated PEDOT:PSS samples. D) Electrical measurement setup connected to potentiodynamic current/voltage instrument.....	19
Figure 11: Overnight deposition of PEDOT:PSS slurry in H ₂ SO ₄ (0.5 M). ...	20
Figure 12: Conductivity comparison of PEGDA 575 with 1% wt. of PI, 5% wt. and 45% wt. of treated PEDOT:PSS that was suspended with two different solvents.	20
Figure 13: Rheological characterization: dynamic viscosity study of TritonX-100 (Tx), Dimethylformamide (DMF) and Dimethylsulfoxide (DMSO) at 5% wt. Blend composition: PEGDA 575 with 1% wt. of PI and 50% wt. of treated Clevios™ PH1000.	22
Figure 14: Surfactant study for PEGDA 575 with 1% wt. of PI and 50% wt. of treated PEDOT:PSS.....	23
Figure 15: Conductivity of the PEGDA 575 with 1% of PI, 5 % wt. of DMSO and 45% wt. of treated PEDOT:PSS samples at different treated PEDOT:PSS contents.....	24
Figure 16: FT-IR spectroscopy of PEGDA 575 with 1% wt. of PI and A) 0% wt. B) 25% wt. C) 35% wt. D) 45% wt. of treated PEDOT:PSS	26

Figure 17: Conversion yield of PEGDA 575 with 1% wt. of PI as a function of treated filler concentration. Data was obtained by FT-IR spectroscopy analysis on 3D printed models before and after the UV process.....	27
Figure 18: Conformation evolution scheme of PEDOT:PSS caused by acid treatment.	28
Figure 19: Raman spectra of A) pristine filler (Clevios™ PH1000) and B) treated filler.....	29
Figure 20: Raman spectrum of PEGDA 575 with 1% wt. of PI, 5% wt. of DMSO and 45% wt. of treated PEDOT:PSS.....	30
Figure 21: (A, B) FESEM images of pristine PEDOT:PSS at two different magnifications. (C, D) FESEM images of treated PEDOT:PSS at the same two magnifications. In the inset of Figure 21B higher magnification FESEM of PEDOT:PSS is reported, while the inset of Figure 21D is a STEM HAADF image of PEDOT:PSS after acidic treatment.	32
Figure 22: FESEM images of: A) treated Clevios™ PH1000 B) PEGDA 575 with 1% wt PI, 5% wt. of DMSO and 45% wt. of treated PEDOT:PSS.	32
Figure 23: Shows two samples: A) optimal resin parameters (2000 mm/s laser scan velocity, 50 mW laser power), while. B) the printed layer in the worst case (500 mm/s laser scan velocity, 75 mW laser power).	33
Figure 24: Conductive PEGDA 575 and 45% wt. of treated PEDOT:PSS 3D printed test samples: (A) Ring chain, (B) micro and macro walls structures combined with holes and undercuts (printing parameters: 50 mW\mm ² laser power, 2000 mm\s scan velocity) and (C) 3D layout.	35
Figure 25: Samples for mechanical tests of PEGDA 575 and 45% wt. of treated PEDOT:PSS with A) 45% wt. B) 35% wt. C) 25% wt.....	36
Figure 26: Stress-strain diagrams for different samples with PEGDA 575 with 1% of PI and (red line)0%, (pink)25%, (green line)35%, (azure line)45% wt. of treated PEDOT:PSS.....	37
Figure 27: Young modulus values of PEGDA 575 with 1% of PI and 25%, 35%, 45% wt. of treated PEDOT:PSS.	38
Figure 28: Side view of sessile drop technique A) PEGDA 575 with 1% of PI. B) PEGDA 575 (1% wt. of PI + 5% wt. of DMSO) with 45% wt. of treated PEDOT:PSS.....	39
Figure 29: Contact angle measurement on PEGDA 575 with 1% wt. of PI and PEGDA 575 with 1% wt. PI, 5% wt. of Dimethyl sulfoxide and 45% wt. of treated PEDOT:PSS.	40
Figure 30: Swelling ratio of PEGDA 250 with 45% wt. of treated PEDOT:PSS.....	41

Figure 31: MTT assay on PEGDA 250 and different content of treated PEDOT:PSS; the results was obtained using the 570 nm wavelength subtracting the background (650 nm).	43
Figure 32: CAD drawing of double helix device. A) General view showing the pads for contact during electrical measurement; B) Top 3D view; C) Lateral 3D view; D) Prospective 3D view	45
Figure 33: 3D printed double helix structure based on PEGDA 575 with treated PEDOT:PSS blend (SL parameters 50 mW laser power, 2000 mm/s scan velocity).	46
Figure 34: Conductivity of PEGDA and treated PEDOT:PSS subjected to a 10 minutes acetone exposure after different drying times.	47
Figure 35: Conductivity of PEGDA 575 and 45% wt. of treated PEDOT:PSS for different exposure times to ethanol and acetone vapors.	48
Figure 36: Normalized resistance variation of double helical samples versus acetone and ethanol exposure times.....	49
Figure 37: A) Resistance of 3D printed double helical device under acetone exposure B) Resistance of 3D printed parallelepiped design under acetone exposure.....	50
Figure 38: A) Raman spectra of PEGDA 575 with 45% wt. of treated PEDOT:PSS samples exposed to acetone vapors for 0, 10, 20, 30, 60 and 120 minutes; B) Conductivity and % quinoid value as a function of the vapor exposure time.	51
Figure 39: Computer-Aided Design drawing of the OECT to be printed.....	54
Figure 40: 3D printed OECT. (A) Device after printing; (B) microscope image of the channel (700 μm wide); (C) section view of the 700 μm wide channel design; (D) SEM image of the same section view reported in (C); (E) SEM image of the PEGDA:PEDOT resin polymerized.	55
Figure 41: (a) Calibration curve for dopamine sensing by a Poly(ethylene glycol) diacrylate 575 and treated PEDOT:PSS using a 3D Organic Electro-Chemical Transistors; (b) typical transfer curves measured at different dopamine concentrations ($[\text{DA}] = 0, 10 \mu\text{M}, 100 \mu\text{M}, 1 \text{mM}$ and 5mM , error bars are standard deviations) and (c) universal curve obtained by merging transfer curves in (c) upon shifting them along the V_{gs} axis.	56
Figure 42: 3D printed disks of PEGDA 250 with 1% wt. PI and 35% wt. of treated PEDOT:PSS with thickness A) 1.5 mm B) 1 mm C) 0.7 mm.	59
Figure 43: A) coin cell B) BioLogic with 2 points connection provides the lowest connection impedance.	60

Figure 44: fabrication steps of 3D-IDE: A) Pt-IDE sputtered on alumina. B) 3D-IDE printed with PEGDA 250 and treated PEDOT:PSS. C) 3D-MSD device.	61
Figure 45: 3D-MSD device based on PEGDA 250 and 35% wt. of treated PEDOT:PSS.....	62
Figure 46: Cyclic voltammograms collected in 0.1 M H ₂ SO ₄ as a function of scan rate 10 mV/s; A) current density B) areal capacitance.	63
Figure 47: CV curves of printed 3D-MSD measured at different scan rates of 10, 20, 50, 100 mV/s.....	64
Figure 48: GCD curves of 3D-MSD based on PEGDA 250 and treated PEDOT:PSS at current densities of 0.5, 1 and 2 mA/cm ²	65

Chapter 1

Additive manufacturing

1.1 Introduction

Manufacturing technologies can be actually divided in three groups: “Subtractive Manufacturing”, such as etching, milling or erosion, “Formative Manufacturing”, such as casting or forging, and finally “Additive Manufacturing” like filament deposition, laser sintering and stereolithography.[1][2]

In particular, “Additive Manufacturing” (AM) is a fabrication approach to make 3D physical objects using a layer-by-layer deposition through material extrusion, vat photo-polymerization, powder bed fusion or material jetting.[3][4]

Is not exactly clear when the first patented concept about the AM was initially claimed. However, in 1952 Kojima[5] demonstrated the benefits of layered manufacturing processes. Subsequently, between 1960 and 1980 a large number of patents and demonstrations was produced[6][7] to confirm the idea of producing a 3D object using a layer-by-layer deposition.

“Rapid Prototyping” or “Generative Manufacturing” was the name of the AM approach when started to enter the market around 1987, however the first systems becoming accessible only early 1990.[8][9]

The AM technologies have radically changed the approach of the standard manufacturing industries producing high levels of design complexity, device customization and production flexibility.

1.2 Additive Manufacturing technologies

Actually, with the modern 3D printing technology is possible to print different types of materials like thermoplastics, metals, ceramics and graphene-based composite materials.[10][11] The advanced technology based on 3D printing can revolutionize industries and change the production systems. In fact,

using the 3D printing technology it will be possible to increase the production speed while reducing manufacturing costs, because the production system will be located near the consumer, allowing for a more sustainable, rapid, and flexible manufacturing process.

Nowadays a large number of 3D printing technologies are present on the market. Depending on the printing process these technologies can be classified in four groups (Figure 1): binding (material jetting or binder jetting), fusion (selective laser sintering or selective laser melting), fusion and solidification (fused deposition modelling) and polymerization based (vat polymerization).[12][13][6]

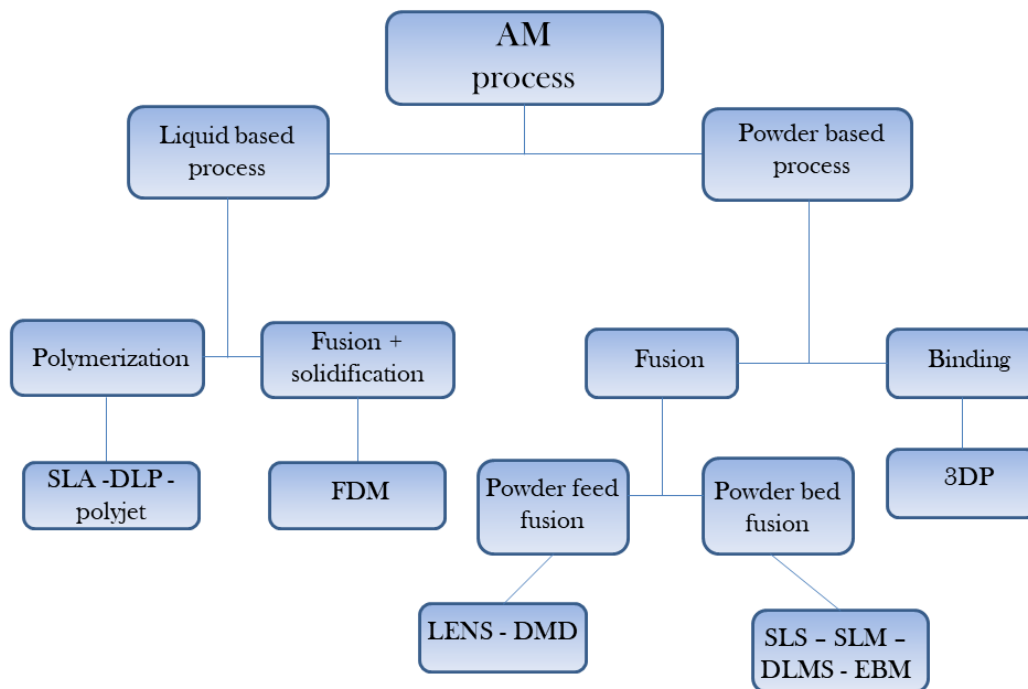


Figure 1: Classification of AM processes.[14]

According to ASTM Standards, binder material jetting is defined as a 3D printing process in which drop by drop powder material is selectively deposited and melted using a binder polymer.[14] The main components in this equipment are the printhead and the ultraviolet lamp. The first is used to dispense small droplets of a polymers, ceramics, composites, biological and hybrid materials that are solidified, building a part layer-by-layer using a photopolymer binder.[15] This technology offers the advantage of fast-build speeds, but with a low accuracy and mechanical properties as some other additive processes.[16]

The main technology used in aerospace and automotive industries is based on powder bed fusion process.[17] This technique allows melting or fusing the material powder together using an electron beam or laser source. For these reasons a huge number of systems, i.e. the electron beam melting (EBM), selective laser sintering (SLS), selective laser melting (SLM) and selective heat sintering (SHS) printing techniques, are present in literature.[18][19] Another

similar 3D printing process is based on directed energy deposition. In this case a nozzle that can move in multiple directions ejects metal powder that is melted by a laser source.[20] Usually this technology is used to repair or add additional material to existing parts. For powder bed fusion processes no post-processing is required to remove the excess material and no support structures because the excess powder in each layer constitutes as a support to the piece under construction.

One of the most important 3D print technologies is based on material extrusion (or fusion and solidification process) as the Fused Deposition Modelling (FDM), which is the first historic example of a material extrusion system. With this technique is possible to extrude, using a narrow nozzle, different types of thermoplastic materials. With these technologies is possible to print a wide range of thermoplastic polymers: polyphenylsulfone (PPSF), polycarbonate (PC), acrylonitrile butadiene styrene (ABS), and Polylactic acid (PLA). Furthermore the 3D printing extrusion is employed to print multi-materials like food or living cells.[21] The printing extrusion process is able to fabricate functional parts, easily and safely with good mechanical properties and high reproducibility.[22] For these advantages, the extrusion process holds the great part of 3D printing market with a very low production cost.

The vat polymerization is the last main class of 3D printing techniques that uses photo-reactive polymers which are cured with a light source.[23] There are two main, versatile and cost efficient 3D printing techniques in vat polymerization: the stereolithography (Stereolithography Laser Apparatus – SLA) and the Digital Light Processing (DLP). Both exploit a photosensitive resin that is mixed with a specific photoinitiator, dyes, pigments or other fillers and a specific laser source to print complex forms with an excellent resolution as compared to other printing techniques.

1.3 Additive Manufacturing applications in micro&nanofabrication

In the last 10 years several new additive manufacturing technologies have been proposed to support micro and nanofabrication.[24][25]

The integration of micro and nanotechnology with AM has the potential to overcome some of the technological limitations of standard fabrication systems. Indeed, it's possible to develop a new generation of devices combining new 3D printing physical methods and composite smart materials.[26] For example, printed electronic and optoelectronic devices using a direct ink writing system.

Another interesting field is the sensing domain i.e. creating an embedded capacitive[27] or strain[28] or chemical sensor.[29][30][31] All these approaches employed different AM technologies types showing the possibility to improve some limits in the standard 2D systems.

Furthermore the conductive performance of energy storage devices such as batteries and supercapacitors, can be improved modifying the architecture of the electrodes active surface.[32][33][34]

Combining AM and Micro&Nanotechnologies it is possible to provide a better mimic of cell microenvironment for biomicrofluidics and tissue engineering.[35][36][37]

Despite various literature examples of connection between AM (allowing to reduce design and manufacturing costs) and Micro&Nanotechnology (able to improve devices performances), we are still far away from the commercial success of 3D printing applied to Micro&Nanotechnology.

1.4 Light-cured printers

The vat polymerization is a 3D printing technique where a photopolymer resin contained in a tank is selectively cured by UV light. In vat polymerization the excess material needs to be rinsed off after the printing process, moreover it is useful to perform a second curing phase under ultraviolet light or oven at 40° C to fix the polymer structure.

The stereolithography apparatus (SLA or SL) and the DLP (Digital Light Processing) are the main printing techniques belonging to vat polymerization (Figure 2). Actually, SL and DLP offer the best compromise between surface quality and printing resolution in AM field.

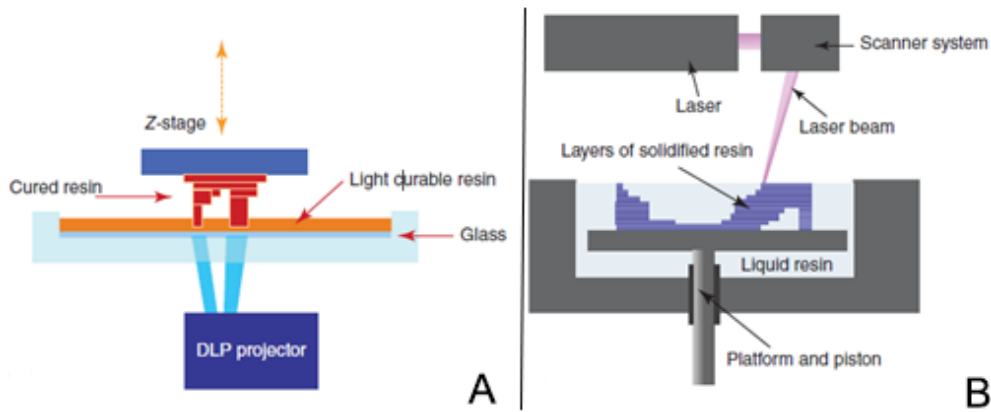


Figure 2: Vat photopolymerization: A) DLP in which a layer of resin is cured by a pattern generated using a projector, B) and SL where the pattern is produced by a scanning laser beam.

The stereolithography process involves a layer-by-layer curing of a photopolymer using a laser source. Between each layer the build platform submerges deeper into the resin tank and after a laser scan across its surface inducing a photopolymerization process.

One of the first patent that describes the SL process was issued by Kodama in 1981; he showed the possibility to print a 3D model in layered stepped stages using a photocurable polymer.[38] In this automatic system, applying a physical mask or moving an optical fiber using a plotter stage it was possible to direct the laser spot onto the vat surface.

The SL print process was invented by Chuck Hall in 1983 (Figure 3).[39][40] The Hall's machine sweeps a laser above the surface of a tank where a UV photocurable polymer becomes hard.

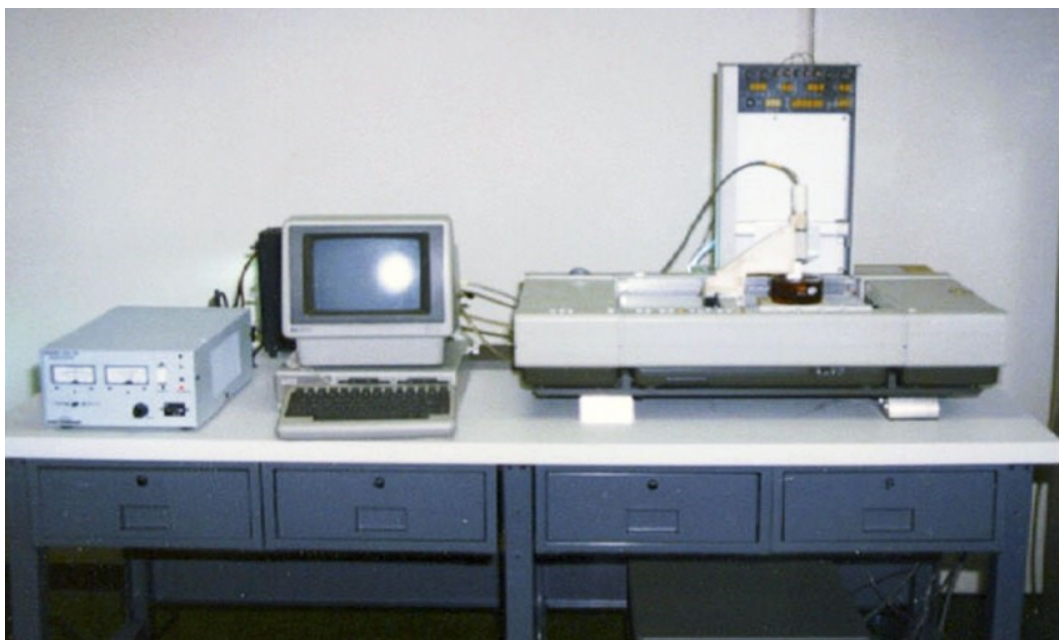


Figure 3: The first SL system launched in 1987.[41]

In SL, the laser energy induces a chemical reaction, bonding a huge number of monomers producing a hard cross-linked polymer. Each sweep of the laser traces the contour of planar section layer-by-layer. After each laser step, a motorized printing area is lowered a fraction of a millimetre in a resin tank. Then a few microns of fresh resin is spread on previously polymerized structure. In Figure 4 a simplified workflow of the SL printer is reported.

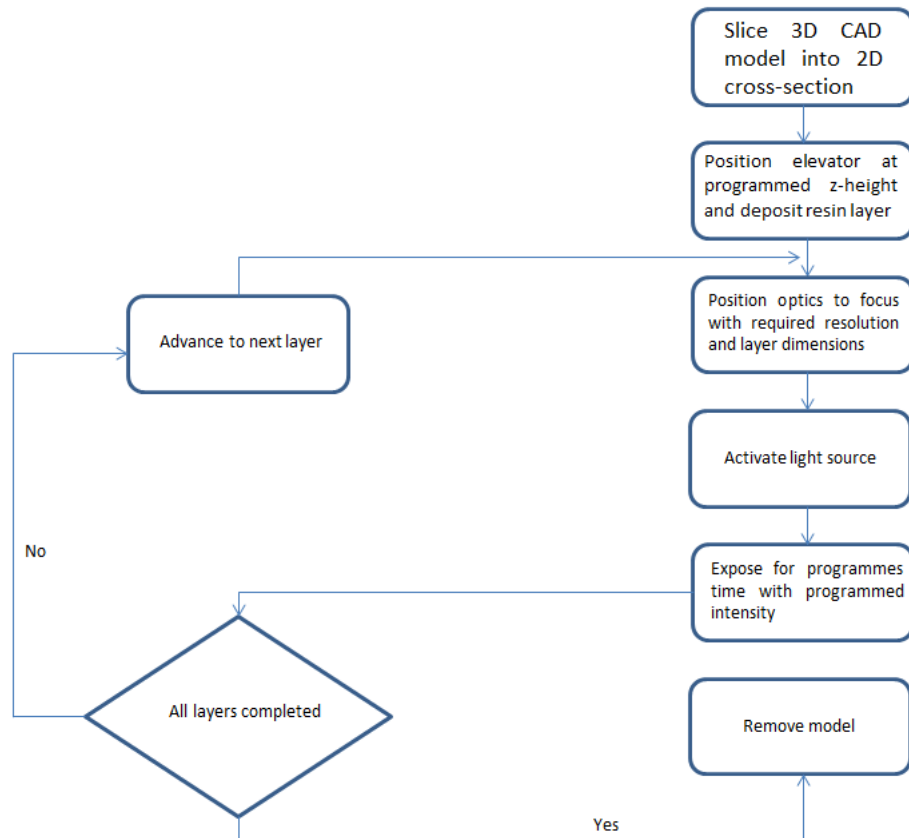


Figure 4: Flow chart of the stereolithography building process.[40]

In 1987, Ciba and the Hall’s company produced the first generation of acrylate resins that represent the largest part of the current market of 3D printing resins.[42][43]

The Digital Light Processing technology uses a light source positioned below the resin tank containing the photopolymer liquid. Layer-by-layer, few microns of fresh photopolymer cover the cured structures after each consecutive immersion of the platform into the resin vat.

In 1996 the first DLP concept was proposed by Nakamoto and Yamaguchi using physical masks.[44] One year later, employing a liquid crystal display (LCD) as the dynamic mask generator, a new DLP system was developed by Bertsch.[45]

Actually the DLP system uses a digital micromirror device (DMD[®]) to project a 2D image inside the resin tank; with this type of light source the whole layer is simultaneously cured in a few seconds.

Although the DLP technologies offer a good compromise between time and surface quality, it has still several disadvantages i.e. the rheology of the suspension, the cleaning process and the resolution quality.[46][47]

The main difference between DLP and SL is the type of light source which can be a projector or a laser beam. The SL technology uses ultraviolet (UV) laser and material is cured point by point, while the DLP technology uses a light projector and at the same time, a single layer is cured.

In vat polymerization the surface profile, the size of the minimum feature and the printing time are strictly related to the employed light source. For this reason the SL technology can produce parts with high surface quality with micron resolution.[48]

Chapter 2

Photopolymers

2.1 Introduction

Polymers are molecules made up by the repetition of some simpler units called monomers. Polymers are classified in two big classes: natural and synthetic. Natural polymers like proteins, polysaccharides, nucleic acids, natural rubbers, cellulose, etc. result from natural biosynthesis. Synthetic polymers are chemicals based on crosslinkable monomers, like saturated macromolecules (i.e., thermoplastics) or unsaturated polymers (i.e., rubbers). In this case the macromolecule used derived from petroleum oil.[49][50]

Actually the blend polymer is one of the most interesting class of polymer. Blend polymers are a combination of two or more constituent materials/polymers, which can have notably different physical or chemical properties. In general, they are made with a matrix/bulk and a filler, which however cannot be distinguished at macroscopic level. Many different types of fillers are present in literature[51] and a large part of them are used to enhance mechanical or physical properties of the matrix.

Using inorganic or organic nanomaterials (filler) it is possible to change the polymer microstructure, increasing or decreasing specific blend properties.

The most common nanomaterials classification is based on their different shapes, i.e. nanofiber, nanoflake, nanorod, nanofilm, and nanocluster types[52][53] Figure 5.

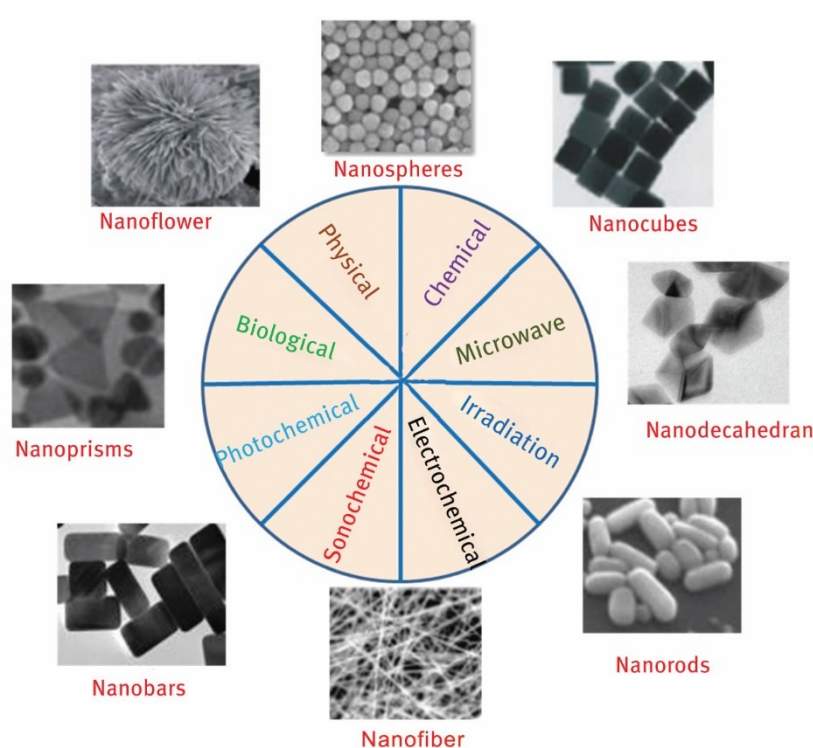


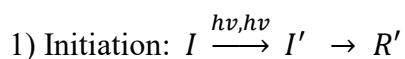
Figure 5: Synthesis routes, nanospheres, nanoplates, nanoprisms, nanorods.[54]

2.2 Photopolymerization

All the objects produced by SL process are based on a photocurable resin. Typically, these materials consist of acrylate polymers (epoxy or oxetane hybrid formulations) which can be combined with other functional materials obtaining a blend polymer. The photopolymerization is a light-induced reaction. In this process an appropriate photoinitiator (PI), that is able to adsorb a specific frequency of the light energy, converts a monomer solution into a solid polymer. The PI is a light-sensitive material that has a good thermal stability, and it's able to produce an active specie under visible, UV or infrared light irradiation.[55] Based on the nature of generated active species (radicals or cations) the PI are subdivided into two corresponding main classes.

Usually the PI has a high quantum yield in the generation of the active moieties and is highly soluble inside of polymer matrix.[56]

The free-radical photopolymerization mechanism can be summarised according to the following three different reactions:



Initiation: the free-radical initiator (I) is activated with light ($h\nu$) and the monomer is induced to form an active specie (R').

2) Propagation: $R' + M \rightarrow RM' \xrightarrow{M} RMM \dots \rightarrow RM'$

Propagation: the initiator fragment reacts with a monomer molecule (M') to form the first active product (RM'_n) that is capable of being polymerized. Then the other monomers continue to add in the same manner (RMM) resulting in the formation of macroradicals, which are end-active polymers.

3) Termination: $RM'_n + RM'_m \rightarrow RM'_{n+m} R$

Termination: is the final step during which the growth center ($RM'_{n+m}R$) is deactivated and the final polymer molecules are formed.

After the photopolymerization a postcuring of the sample is usually performed through UV light, rather than heat, to complete the reaction and favour solvents evaporation.

Depending on the specific requirements i.e. material's properties, feature definition, resolution and surface topologies, is necessary to choose carefully matrix, filler and photoinitiator.

2.3 Conductive polymer

Conductive polymers (CP) are one of the most important classes of organic polymers able to conduct electricity. Initially the conductive polymers was composite materials and they were obtained by adding carbon black or acetylene black to natural rubber, later introducing metallic powders in plastics. Subsequently the effect of more parameters which are able to influence the CP properties was studied, i.e. concentration of conducting filler, filler matrix interaction, mixing effect and charge transport.[57][58][59] A large plethora of nanoparticles in CP blend was study i.e. CNTs[60], graphene[60], graphene oxide[61], metal nanoparticles[62] and a new class of intrinsically conductive polymers (iCP).[63]

The first synthesized iCP was polythiophene and polyphenylene in the Plastics Research Laboratory of BASF in Germany. These polymers showed electrical conductivities of up to 0.1 S/cm.[64]

The conjugated polymers such as polyaniline(PANi), polythiophenes (PTs), and polyacetylenes in pristine state are insulators or semiconductors and their electrical conductivity is around 10^{-10} to 10^{-5} S/cm.[65][66]

The iCP properties can be controlled changing the preparation methods or the nature of inorganic materials embedded inside.

The iCP can be synthesized chemically or electrochemically. The first synthesis method either use addition polymerization or condensation polymerization and provides several different ways to synthesize a variety of iCPs. The chemical synthetization also allows the scale-up synthesis of these

polymers. However, electrochemical synthesis is relatively straightforward and, therefore, commonly used for manufacturing iCPs.[67] Furthermore the polymers conductivity can be enhanced by chemical or electrochemical doping (p-doping(oxidation) or n-doping(reduction)).[68] In particular for polyacetylene the conductivity could be increased by several orders of magnitude by "doping," using an addition of electron acceptors (p-type) such as iodine or arsenic pentafluoride and by the addition of electron donors (n-type), such as sodium or sodium naphthalide.[69]

2.4 PEDOT:PSS

Thiophene (TH) is an electron-rich aromatic ring and belongs to heterocyclic compound family. A TH ring, with the formula C_4H_4S , contains five membered ring made up of one sulphur as heteroatom (Figure 6). The first chemical preparation of unsubstituted polythiophene (PT) (with low molecular weight) was achieved in 1980 by two groups[70][71] using a policondensation reaction; however the product reaction was found to be insoluble[72][73]. Subsequently the poly3,4-ethylenedioxythiophene (PEDOT), which is one of the most important PT polymers, was developed by BASF in 1991.[74] Furthermore the polymers containing thiophenes are able to convert the cyclohexadiene from quinoidal to a benzene structure when the benzenoid thiophene is oxidized.[75] This means that the conductive structure will be very energetically stable.

The PEDOT (doped with $FeCl_3$) gave a conductivity around 0.62 S/cm and a good chemical stability, however it was mostly still insoluble.[76] The water solubility has been achieved using a chemical polymerization in poly(styrenesulfonic acid) (PSS) solution. With this synthesis process, a PEDOT:PSS water emulsion was obtained.[77] This polymer blend show conducting grains in a PSS matrix (Figure 6).[78]

The main application of PEDOT:PSS is in electronic devices such as transparent electrodes for electrostimulation or sensing. A large variety of bio-electrode coatings, electrochemical sensors and supercapacitor have been widely investigated in recent decades.[76]

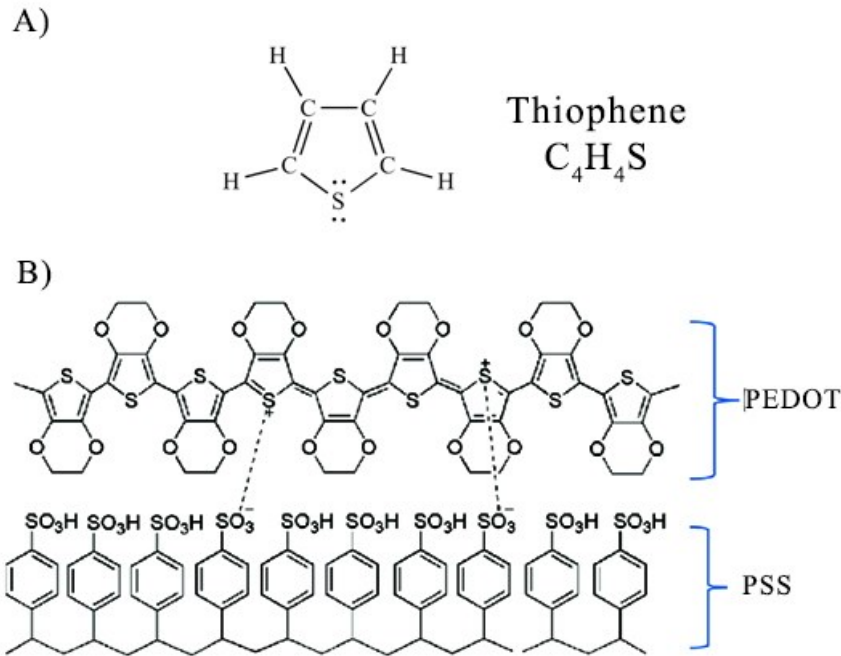


Figure 6: A) Thiophene chemical structure. B) PEDOT:PSS chemical structure

2.5 Photocurable conductive resin

Although a plethora of conductive polymer composites (CPCs) are reported in literature, in SL field there are not many examples. Actually the matrix polymers are poly-acrylate derivatives, where the C=C bonds in vinyl groups crosslink with different monomers, and the electrically conductive fillers usually are organic materials or conductive polymers or metal nanoparticles.[79]

Carbon-based materials are functional nanofillers that have been widely studied in many fields. The allotropic conductive forms of carbon have several applications in the SL printing.[80][81][82] The most exploited are carbon nanotubes (CNT)[83][84] or multi wall carbon nanotubes (MWCNTs)[85][86]. A MWCNTs mass fraction of about 0.2 wt. % allows an electrical conductivity of 0.01 S/cm, however, the achieving material has a fragile behaviour.[87]

Usually other fillers are metal particles i.e. silver nanoparticles (AgNPs), which can be mixed[14] or local synthesized [15] on different materials, making stretchable three-dimensional circuits or electrical track, with a conductivity around 125 S/cm. Though this material have interesting electrical properties this technology is very expensive and require an ad-hoc setup.[88]

Metal alloys such as palladium/silver-copper (PdCu)/(AgCu)[89] and metal oxides nanoparticles like barium titanate (BaTiO₃)[90] are also employed to induce conductive pathways on the final object. In this case the conductivity achieved with these nanomaterials is around 5,84 kS/cm however this production process requires a strong chemical etching and multiple fabrication steps.

Nowadays conductive polymers (iCP) as pyrrole, aniline or thiophene derivatives can be integrated in not conductive materials during the SL process. The polypyrrole (PPy) is embedded in urethane dimethylacrylate[91][92] polymer obtaining 0.01 S/cm. Also the Polyaniline (PANI) polymer that can be conjugated with poly vinyl alcohol (PVA)[93] or gelatine methacrylate (GelMA) to get a conductive material granting 17 S/cm.[94][95] Although PEDOT:PSS is widely used for different applications like solar energy[93], tissue engineering[93] and sensing[96] there are not examples in literature of PEDOT:PSS based blend polymers for SL application.

In this PhD thesis a photocurable resin based on PEDOT:PSS was developed using a Poly(ethylene glycol) diacrylate (PEGDA) matrix.

Chapter 3

PEGDA:PEDOT conductive resin

3.1 Stereolithography printing machine

In this work an open source stereolithography machine (Figure 7)[97] was used, where the printing area, the laser scan velocity, the energy and other optical and electronic parameters can be customised. Furthermore, in this equipment is possible to change the resin vat and the working area (Figure 7). Actually, the maximum printable area is $170 \times 200 \text{ mm}^2$. Furthermore, the printer is equipped with a recoater to remove the resin excess on the working area (Figure 7).

Two important parameters control the printing process: power and velocity of the laser beam scan. The modulation of these two parameters allows the polymerization of many photoresins with different resolution.

The SL optical path is composed by a laser source, a beam expansion section, a galvanometric scanner and a theta-lens.

In details, the system is equipped with a 405 nm laser source with a maximum power of 120 mW. The minimum and maximum laser speeds are 0.5 mm/s and 2000 mm/s respectively.

The beam expander is placed after the laser source and it's able to expand an input light beam depending on its expansion factor driven by the characteristics of the two constituting lenses. A $5\times$ expansion was chosen for this printer to obtain 7.5 mm diameter spot size at the galvanometric head input.

The system used to position the laser beam on a 2D plane is a galvanometric laser scanner, which is able to rotate two flat mirrors of a desired angle value (Figure 7). Some details about the galvanometric scanner are reported in table 1.

Mechanical data:

Min spot diameter (μm)	~ 80
Beam displacement (mm)	12.4
Weight (kg)	Approx 0.8
Dimension (L \times W \times H (mm))	100.0 \times 77.0 \times 77.5

Dynamic data:

Acceleration time (ms)	0.23
Writing speed (mm/s)	2000

Table 1: relevant optical characteristics of selected galvanometric scanner are reported.

In this 3D printer the theta-lens was necessary to focus the laser beam at the focal point. The theta-lens is a precise telecentric lens which minimizes the distortion and makes a laser beam incident almost perpendicularly to the working area. Indeed, the theta-lens ensures that the focal point is always positioned in the working plane and perpendicular to the objective's optical axis.

In the employed printer a theta-lens focal of 260 mm was used to focalize the spot on the resin level.[98]

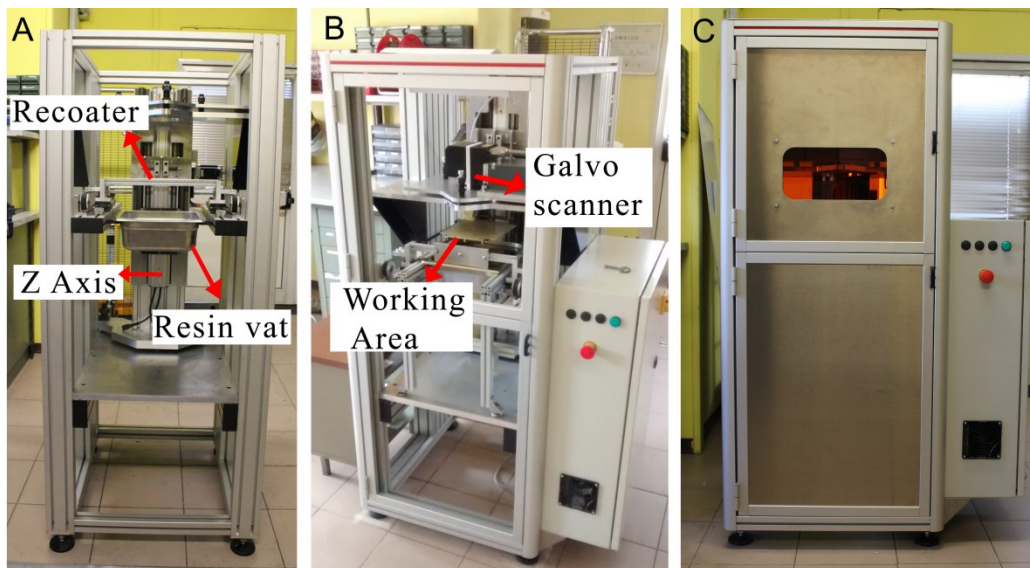


Figure 7: Customised SLA printing machine: A) SLA mechanical system, B) SLA components. C) SLA printer completed enclosure.

3.2 Photoinitiator concentration

The viscosity of the liquid resin is strictly correlated molecular weight of the monomer used. Often the resin with high molecular weight has a high viscosity. For SL printer the high resin viscosity does not allow a uniform level on the top of the printing plates. On the other hand, if the viscosity is too low, the resin thickness will not be enough for the curing process. In some cases it is possible to adjust the resin viscosity using a proper diluent such as 1,6-Hexanediol diacrylate(HDDA), Propoxylated Neopentyl Glycol Diacrylate(NPG2PODA)[99] or poly(ethylene glycol) methyl ether methacrylate(PEGMEMA).[100] However, it is necessary to choose a proper photocurable polymer as a function of the SL printer.

In this work the Poly(ethylene glycol) diacrylate (PEGDA) with a molecular weight of 575 kDa or 250 kDa and the Irgacure 819 were chosen as bulk material and photoinitiator (PI) respectively. The matrix and the PI was purchased from Millipore Sigma (Burlington, MA, USA).

The Irgacure 819 or bis(2,4,6-trimethylbenzoyl)phenylphosphane oxide is one of the most used photoinitiators under which the UV light (the maximum absorption is at 370 nm [101]) source allows networks to form via free radical polymerization.[102]

Initially, the minimum concentration of PI inside the bulk matrix was studied preparing three different PEGDA 575 matrices with four different percentages of PI that are usually used in literature.[103][104] Previous research has established the possibility to modulate the mechanical properties of the matrix using different PI ratios. Using low or high concentrations, it is possible to obtain rigid[25] or flexible[26] materials.

Four PI quantities were employed as percentage of the PEGDA 575 mass: 0.01, 0.1, 0.5 and 1% wt. The mixing process was performed with a digital sonifier at 30 kHz (Branson PG), working in impulse mode at 35% amplitude for 15 minutes. To keep the mixture at a low temperature, it was cooled with ice water.

Samples were then printed using a SL printer (Chapter 3.1) with 5 mW laser power and 2000 mm/s laser scan velocity (Figure 8).

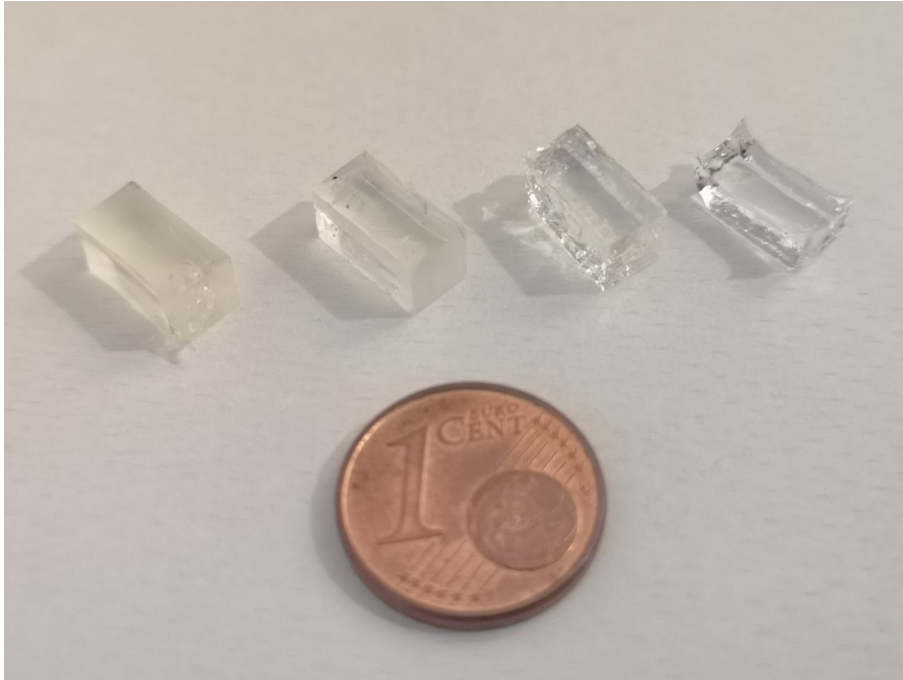


Figure 8: PEGDA 575 with 1, 0.5, 0.1, 0.01 % wt. of photoinitiator from right to left.

Mechanical measurements were performed using an Instron 3366 dynamometer (Instron Corporation, Norwood, US) equipped with a load cell of 500 N. All the tests were performed at room temperature using a crosshead speed of 1 mm/min. Three samples were tested for each IP concentration and their initial dimensions were $20 \times 10 \times 0.3 \text{ mm}^3$. In Figure 9, the Young modulus of PEGDA 575 with the different amounts of PI (0.01, 0.1, 0.5, 1% wt.) is reported. Increasing the PI concentration causes an increase in crosslink density and correspondingly higher material rigidity.

Therefore, the final material with less than 0.5% wt. of PI is crumbly and difficult to handle, while with 0.5 or 1% wt. the material has a stable Young modulus around 21 MPa and is mechanically consistent.

For all the following experiments, the maximum PI concentration, i.e. 1% wt. was chosen to obtain a hard PEGDA 575 after the printing process.

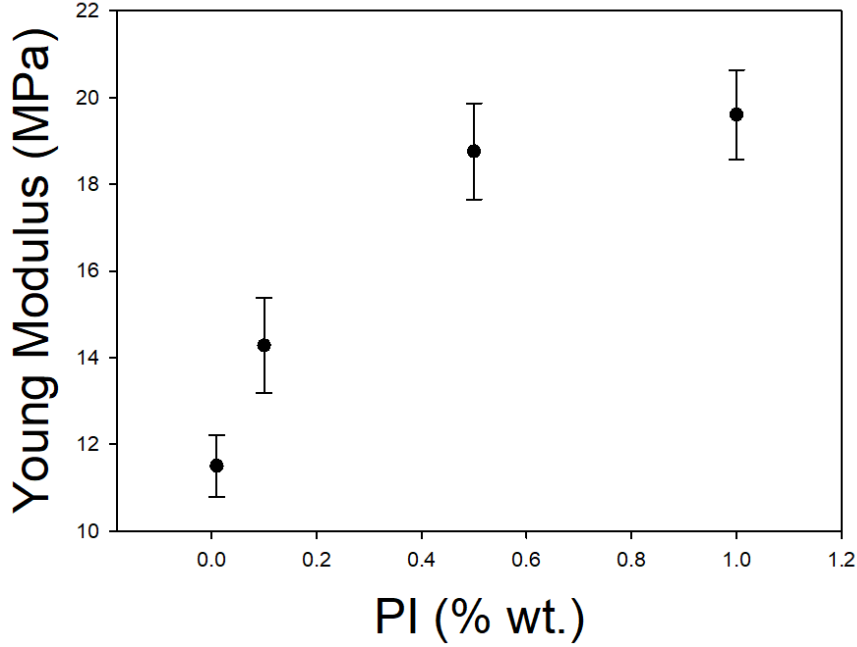


Figure 9: Young modulus of PEGDA 575 with different PI concentrations.

3.3 Electrical measurement setup

In this work, some samples ($0.5 \times 0.5 \times 1 \text{ cm}^3$) were produced using a PDMS mold (Figure 10A). Figure 10B shows the PEGDA 575 samples and Figure 10C shows three samples of PEGDA 575 with 1% wt. PI and 35% wt. of treated PEDOT:PSS.

The curing was performed with a UV lamp (Hamamatsu LIGHTNINGCURE Spot light source LC8) with an emission wavelength of 365 nm for 5 minutes.

For all of the following experiments reported in this work, a potentiodynamic current/voltage instrument (Keithley 6430 Cleveland, US) was used to measure the material resistivity. The material resistivity ρ ($\Omega \cdot \text{cm}$) was calculated following equation 1 where ‘R’ is the ohmic resistance, ‘A’ the cross-section area (0.25 cm^2) and ‘ ℓ ’ the sample length (1 cm).

$$\text{Eq. 1} \quad \rho = \frac{R \cdot A}{\ell}$$

Before the electrical measurement, the two opposite smallest faces of the block sample were homogeneously covered with a silver conductive ink (RS Pro Silver Conductive Adhesive Paint). After the ink dried and 11 current/voltage values were acquired by applying a voltage from -1 V to $+1 \text{ V}$ Figure 10D.

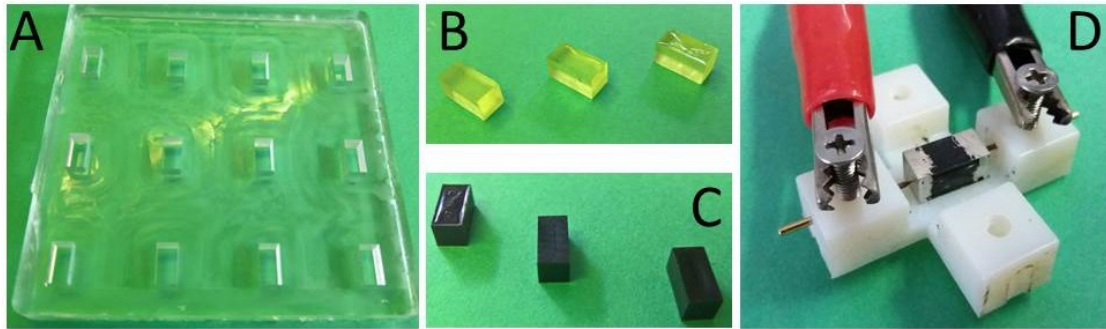


Figure 10: A) PDMS mold for samples preparation. B) PEGDA 575 with 1% wt. PI samples and 5 min under UV light (365 nm) C) PEGDA with 35% wt. of treated PEDOT:PSS samples. D) Electrical measurement setup connected to potentiodynamic current/voltage instrument.

3.4 Filler preparation

In this work the PEDOT:PSS (Clevios™ PH 1000, Heraeus) was chosen as conductive filler to develop an innovative printable conductive blend for SL 3D printing.

A huge number of published studies about the H₂SO₄ bath treatment as one of the most efficient methods to increase the conductivity of PEDOT:PSS. [105][106][107][108] Using an acid treatment it was possible to decrease the coulombic interaction between the positively charged PEDOT and the negatively charged PSS. Furthermore, it allows a conductivity enhancement of Clevios™ PH1000 because some PSS groups are removed[109][110] and the PEDOT chains undergo a structural modification (from random to linear arrangements Chapter 3.8).[111]

For this reason the Clevios™ PH1000 was mixed with an H₂SO₄ solution (0.5 M) over night, obtaining a treated PEDOT:PSS slurry (Figure 11).

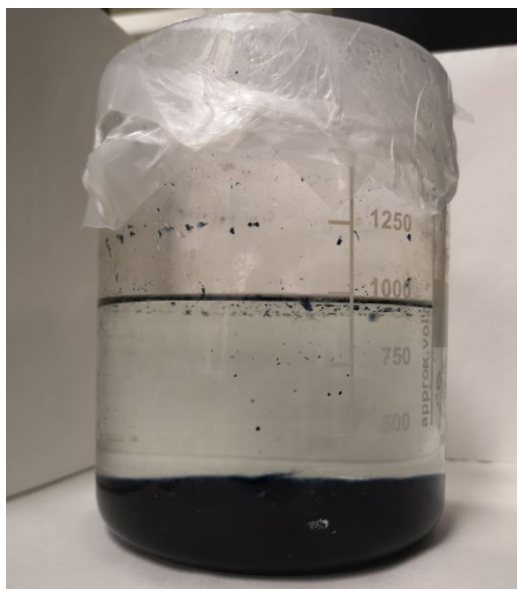


Figure 11: Overnight deposition of PEDOT:PSS slurry in H₂SO₄ (0.5 M).

After the sulphuric treatment is necessary to wash the PEDOT:PSS slurry. Ethanol and sulphuric acid (0.5 M) solvents were compared to enhance the purification and particles splitting up. An ultrasound titanium horn was used in pulse mode (5 seconds ON and 5 seconds OFF) with 65% to 70% of amplitude (Digital Sonifier, Model 250, Branson Ultrasonics Corporation, Danbury).

PEGDA 575 with 1% wt. of PI and 45% wt. of treated PEDOT:PSS fractionated using ethanol or H₂SO₄ provide 1×10^{-2} S/cm and 1×10^{-3} S/cm respectively (Figure 12). Then the ethanol was chosen as the appropriate solvent to purify the treated PEDOT:PSS, because it's low density helps to better suspend the filler particles.

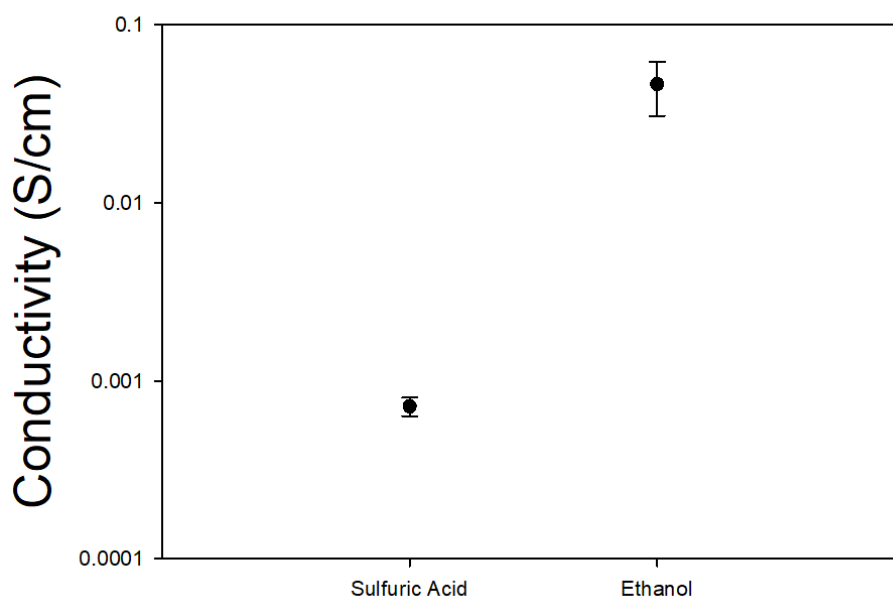


Figure 12: Conductivity comparison of PEGDA 575 with 1% wt. of PI, 5% wt. and 45% wt. of treated PEDOT:PSS that was suspended with two different solvents.

After, it was diluted in ethanol and centrifuged for 15 minutes at 4000 rpm. The supernatant was removed using a Pasteur pipette and treated PEDOT:PSS was obtained. The maximum filler fraction achieved with this protocol is around the 39.6% wt. of the initial weight of Clevios™ PH1000.

In the end, the treated PEDOT:PSS was mixed to PEGDA 575 with 1% wt. of PI under magnetic stirring at 600 rpm for 5 minutes.

3.5 Suspension study

To achieve a uniform blend dispersion, it is necessary to have a similar polarity with filler and matrix.[112][113] Furthermore, the blend polarity influences the viscosity and the blend homogenization. A high or low viscosity cannot allow a homogeneous recoating and spreading of the liquid resin on the SL working area.

To stabilize the filler suspension in matrix with high molecular weight, it can be helpful to use some surfactant inside the resin.

PEGDA has a negative low charge polarity.[114][115] The PEDOT:PSS polymer has the EDOT grains that are positively charged and the PSS “shells” are negatively charged.[116] The PEGDA and treated PEDOT:PSS without the acid and ultrasound treatment are immiscible and produce a two-phase system[117], because they have two different phases: PEGDA was fluid in a water solution, while the treated Clevios™ PH1000 was a semisolid phase.

In other studies, many examples can be found of the mixture of resins with ceramic powders[118][119] or generally with nanoparticle dispersions.[120] In most of these approaches some dipolar aprotic surfactants or solvents have been used to enhance dispersion, stabilize and retard the precipitation process. A large plethora of polar solvents for PEDOT:PSS is available in literature.[121] In this work, two solvents and one surfactant were tested at the same concentration reported in literature i.e. 5% wt. The solvents and surfactant investigated were Dimethylformamide (DMF)[122][123], Dimethylsulfoxide (DMSO)[124][125] and TritonX-100 (Tx)[120][126] respectively. A Rheometer (Physica MCR-301, Anton Paar GmbH) helped determining the viscosity on three resin samples having the same PEGDA 575 (with 1% wt. of PI) and treated PEDOT:PSS ratio (1:1) without the ultrasound treatment. In this experiment the PEGDA 575 matrix and conductive filler had the same ratio because we wanted to investigate the maximum concentration that was possible to disperse inside the resin. Furthermore, in this experiment we tested the possibility of using the pure treated PEDOT:PSS fraction without the ultrasound treatment to achieve a conductive blend with a simplified process.

The viscosity measurements were performed at room temperature for all the experiments. The shear rate was varied from 0 to 100 s^{-1} and the rheometric profile of viscosity vs shear rate of 3 samples were used to evaluate the resins

spreadability. The results show a shear thinning behaviour, which is well described by a power law model $\eta(\dot{\gamma})=m(\dot{\gamma})^{n-1}$ (dashed lines in Figure 13). Here are the equation results:

(Eq. 2)	DMF	$\eta(\dot{\gamma})= 127.1 (\dot{\gamma})^{-1.06}$
	Tx	$\eta(\dot{\gamma})= 72.7 (\dot{\gamma})^{-0.98}$
	DMSO	$\eta(\dot{\gamma})= 28.4 (\dot{\gamma})^{-0.88}$

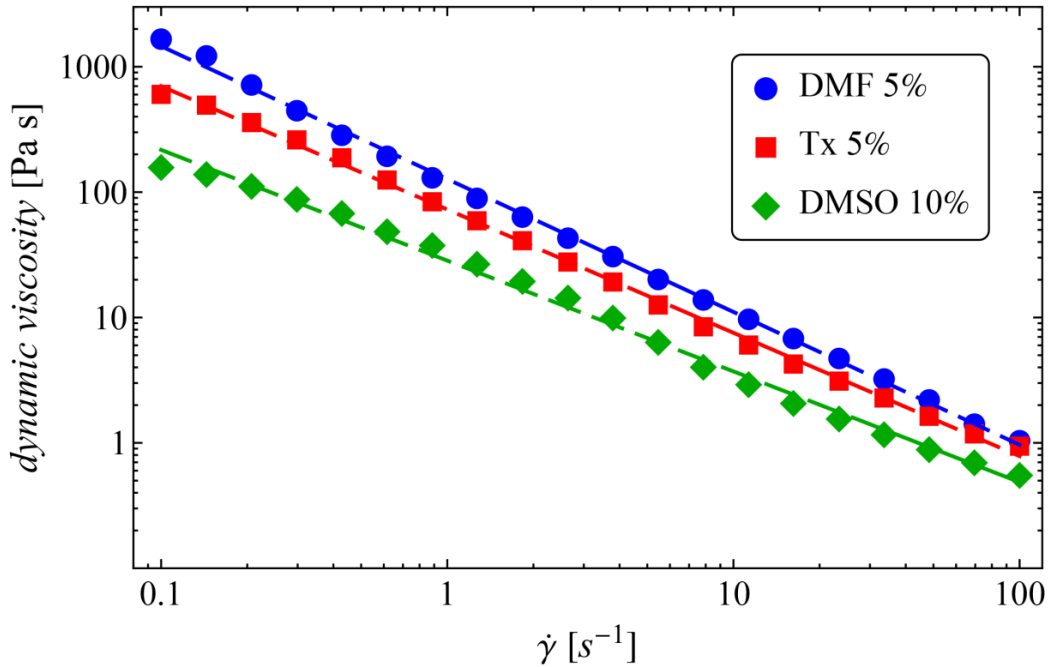


Figure 13: Rheological characterization: dynamic viscosity study of TritonX-100 (Tx), Dimethylformamide (DMF) and Dimethylsulfoxide (DMSO) at 5% wt. Blend composition: PEGDA 575 with 1% wt. of PI and 50% wt. of treated Clevios™ PH1000.

For the SL printer it is necessary to have a blend resin with low viscosity. In this way there will be a perfect uniform layer on the working plate during the printing process. Comparing the equation results in Figure 13, the blend with the lowest viscosity, at the same shear stress $\dot{\gamma}$ conditions, was obtained with DMSO. For this reason, the DMSO was chosen as the appropriate suspension solvent.[127]

Subsequently, the stability of the resin blend was investigated. Four resin blend samples with different DMSO ratios were prepared (1, 5, 10 and 15% wt. in 10 mL). Figure 14 shows the results of this experiment after 90 minutes.

Using a large amount of DMSO (10% wt. or 15% wt.), a significant fraction of resin was separated due to a possible overcome of critical micelle concentration (cmc) of surfactants that forces the particles to collapse and aggregate producing an unstable suspension.[128][129] While with low concentration (1% wt. or 5% wt.), the PEGDA 575 and treated PEDOT:PSS resin was stable for more than 90 minutes. Indeed, we found that the 5% wt. DMSO

resin stability was preserved up to 48 h and, even after sedimentation, a simple mixing (500 rpm for 5 minutes with a magnetic stirrer) was sufficient to regenerate a stable suspension. Furthermore, the resin with 5% wt. of DMSO showed a good printability with respect to the 1% wt.

Thus, the experiment suggests that 5% wt. is the optimum concentration of DMSO needed to create a hydrophobic environment around the treated PEDOT:PSS chain to stabilize the collapsed form.

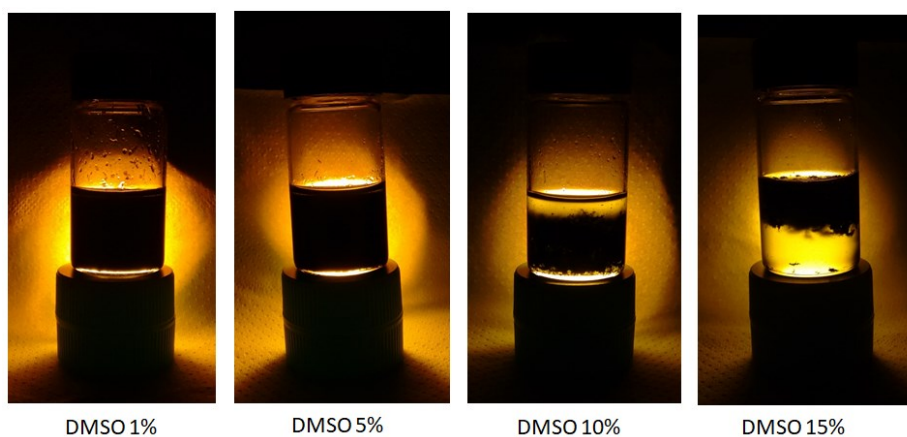


Figure 14: Surfactant study for PEGDA 575 with 1% wt. of PI and 50% wt. of treated PEDOT:PSS.

3.6 Percolation threshold

The percolation threshold filler concentration was investigated considering the blend resin composed by PEGDA 575 with 1% wt. of PI, treated PEDOT:PSS with the ultrasound treatment and DMSO 5% wt.

The electrical conductivity of the blend resin containing different percentages of treated PEDOT:PSS is shown in Figure 15. As a general trend, the electrical conductivity variation versus the conductive filler loading followed a sigmoidal curve. In the beginning, a small PEDOT:PSS content yields a high resistivity, but adding small fractions of treated PEDOT:PSS, we obtained an asymptotic trend of the curve. We observed that the material conductivity become high at ~25% wt. of filler loading, which a corresponding conductivity of 0.08 S/cm. This is consistent with the value of percolation threshold (v_c) that is estimated from a differential analysis on the fitting curve ($R^2 = 0.95$, $v_c = 0.25$). In this study, the percolation threshold was significantly higher when compared to other literature values around 0.02 or 0.05.[130][131] The reason lies in the size (length or diameter) of the employed filler (linear or complex chain).

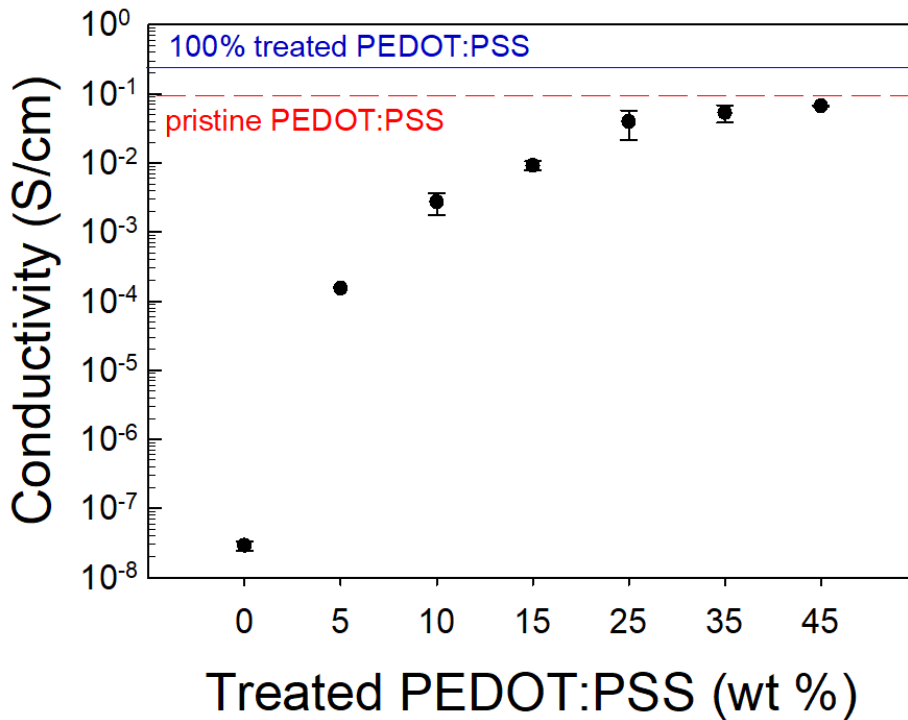


Figure 15: Conductivity of the PEGDA 575 with 1% of PI, 5 % wt. of DMSO and 45% wt. of treated PEDOT:PSS samples at different treated PEDOT:PSS contents.

Above 25% wt. treated PEDOT:PSS in PEGDA 575, the blend resin conductivity increased monotonically and the highest conductivity of 0.06 S/cm was attained at 45% wt. of filler.

This highest amount of filler was close to maximum conductivity values (Figure 15) of treated PEDOT:PSS and pristine PEDOT:PSS material. Furthermore, a filler fraction percentage greater than 45% wt. would undesirably affect the mechanical behaviour of the resin and ultimately hinder its printability due to the high ratio of treated filler that increased the viscosity.

Therefore, PEGDA 575 with 45% wt. of treated PEDOT:PSS proved to be the best compromise between conductivity and printability.

3.7 Fourier transform infrared spectroscopy analysis

The micro or nanofillers can powerfully influence the UV curing process of photocurable blend. Indeed the size and shape of the filler fraction can induce a light scattering and shielding centres, which change the maximum cured thickness of the resin and the curing degree.[132][133]

The PEGDA:PEDOT resin photocuring conversion was checked by Fourier transform infrared (FT-IR) spectroscopy, using a Thermo Scientific™ Nicolet™ iS50 spectrometer (Madison, USA) in Attenuated Total Reflectance (ATR) mode. All spectra were taken by an accumulation of 32 scans with a resolution of 4 cm^{-1} , in the spectral range of $4000\text{--}600\text{ cm}^{-1}$. The quantification of the FT-IR peak areas was carried out with Thermo Scientific™ OMNIC™ Software. In particular, the decreasing of the absorption band area related to the reactive functionality (stretching of C=C acrylic group of PEGDA centred at 1635 cm^{-1})[134][135] was monitored. Specifically, the conversion yield was calculated from the ratios between the areas of this band and those at 1720 cm^{-1} , assigned to the C=O carbonyl group[136] before and after polymerization, as reported in Equation 3.[137]

$$\text{Eq. 3} \quad \text{Conversion (\%)} = \left(1 - \frac{A/A_{ref}}{A_0/A_{0,ref}}\right) \cdot 100$$

Where A_0 and A are the area of the absorption band of the reactive functionality before and after curing, respectively, while $A_{0,ref}$ and A_{ref} are the areas of the C=O peak before and after curing, respectively.

FT-IR analyses were performed on the flat surface of 3D printed samples in the form of small cubes of 1 cm^3 . Spectra were acquired on at least three different spots of a sample under the same conditions to confirm the reproducibility of the results. Finally, the average conversion value and the standard deviation were calculated and reported.

The photocuring reaction conversion of the PEGDA:PEDOT resin was evaluated by FT-IR spectroscopy in ATR mode, as a function of treated PEDOT:PSS concentration. A spectrum for each sample (i.e. liquid resin formulation, 3D printed solid sample and 3D printed solid sample after post-curing) is reported in Figure 16A, B, C, D as an example.

Observing the spectra in Figure 16, it can be clearly noted that the absorption band centered at 1635 cm^{-1} , which is due to the reactive C=C acrylic group of PEGDA 575, decreases with UV irradiation. In fact, such peak is lowered after the 3D printing process, and is further decreased after the post-curing step. FT-IR ATR spectra were used to calculate the UV curing conversion occurring during 3D printing of the PEGDA:PEDOT mixtures, by monitoring the ratio between the areas of the acrylic band and that of the carbonyl group,

centered at 1720 cm^{-1} , before and after UV irradiation. Results (in terms of percentage of acrylic C=C conversion) are reported in Figure 17.

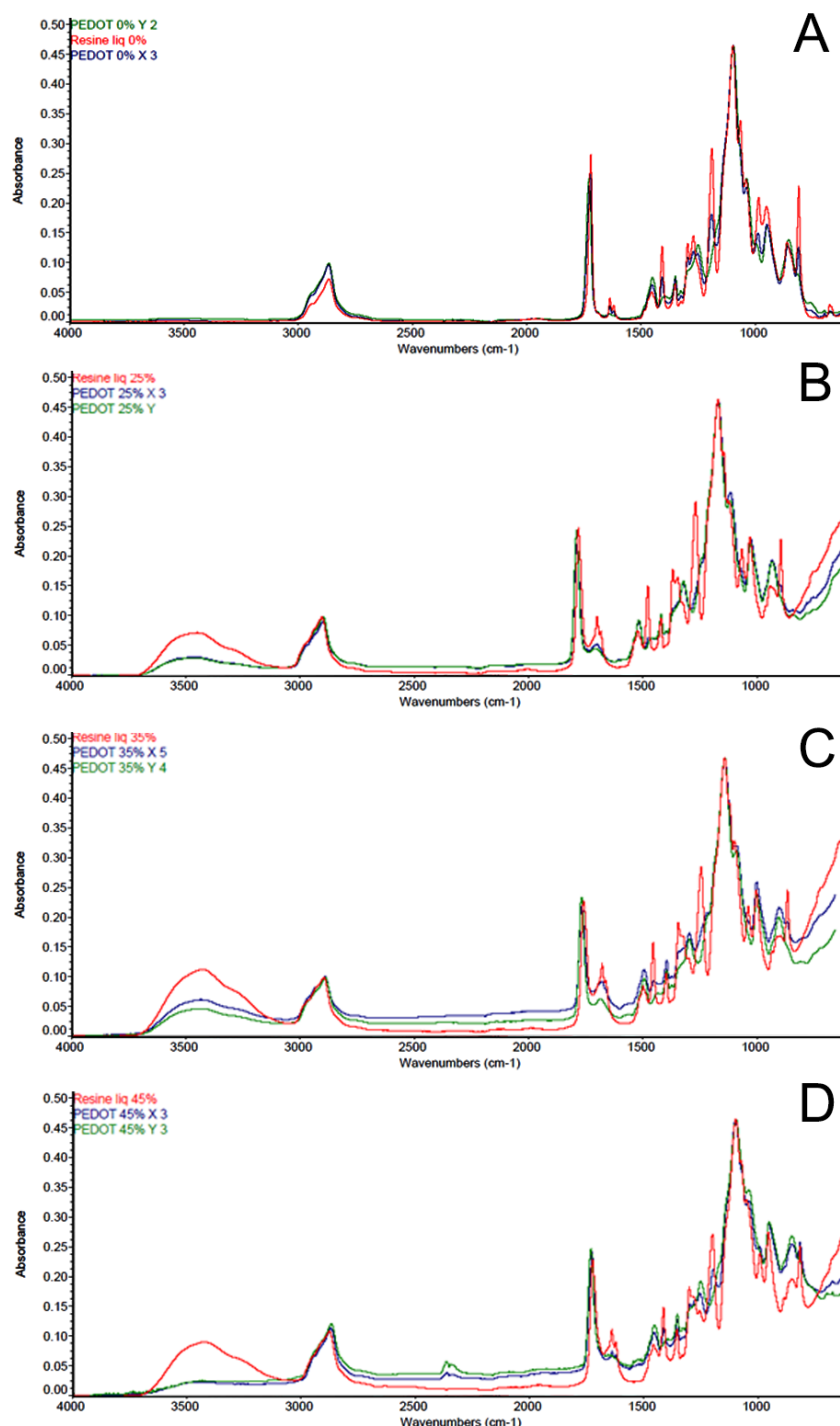


Figure 16: FT-IR spectroscopy of PEGDA 575 with 1% wt. of PI and A) 0% wt. B) 25% wt. C) 35% wt. D) 45% wt. of treated PEDOT:PSS

With the 3D printing process, conversions higher than 50% are obtained. In fact, the resin solidification occurs at UV doses well below full conversion. Thus, while the object shape is set by the initial exposure during 3D printing, conversion can be enhanced or completed by a post-curing step (i.e., an intense,

flood UV exposure). This stage serves multiple purposes, including exhausting any residual initiator and improving the physico-chemical properties and the stability of the 3D printed material. The resin conversion after post-curing is in the range 81–95 % (Figure 17).

The introduction of treated PEDOT:PSS filler slightly reduced the PEGDA 575 conversion, as shown in Figure 16B, C, D. Even if a 10% decrease in the conversion degree of PEGDA 575 is obtained, it can be observed that its value remains constant by varying the filler loading from 25 to 45% wt.

In conclusion, independently on the treated PEDOT:PSS content, highly converted (>80%) samples were obtained after 3D printing and post-curing process: this result highlights the essential role of this processing step in producing reliable and manageable objects.

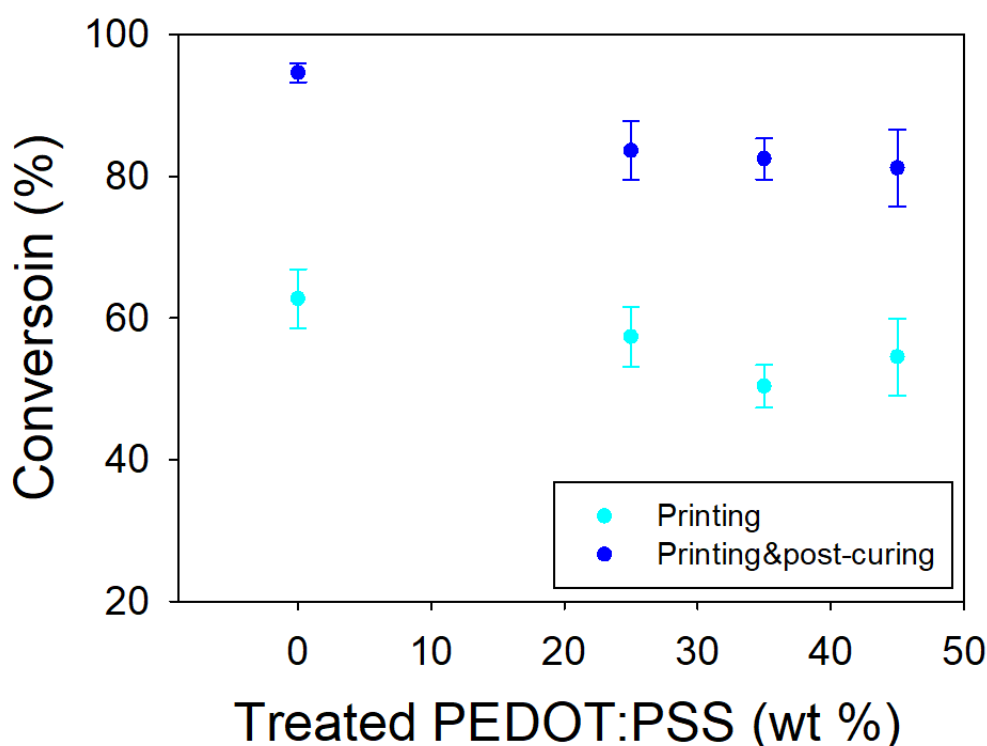


Figure 17: Conversion yield of PEGDA 575 with 1% wt. of PI as a function of treated filler concentration. Data was obtained by FT-IR spectroscopy analysis on 3D printed models before and after the UV process.

3.8 RAMAN spectroscopy

The previously postulated sulphuric treatment is able to replace the negatively charged PSS^- ion with the protonated acids PSSH derivative; in this mode, the PSS phase could be partially separated from the PEDOT chains. This reaction causes a conformational change in the PEDOT which is curled up in a coil structure in the pure PEDOT:PSS film.[138]

The benzoid arrangement provides a coil structure, while the quinoid conformation provides a linear or expanded-coil structure (Figure 18). Then, using a specific treatment is possible to achieve all these structural conformations of PEDOT:PSS.

In the molecular structure transformation, a C–C single bond between two monomers has been replaced by a π bond, as shown in Figure 18. The quinoid conformation allows an extension of poly(3,4-ethylenedioxythiophene) chains, leading to an improved crystallized molecular arrangement.[139]

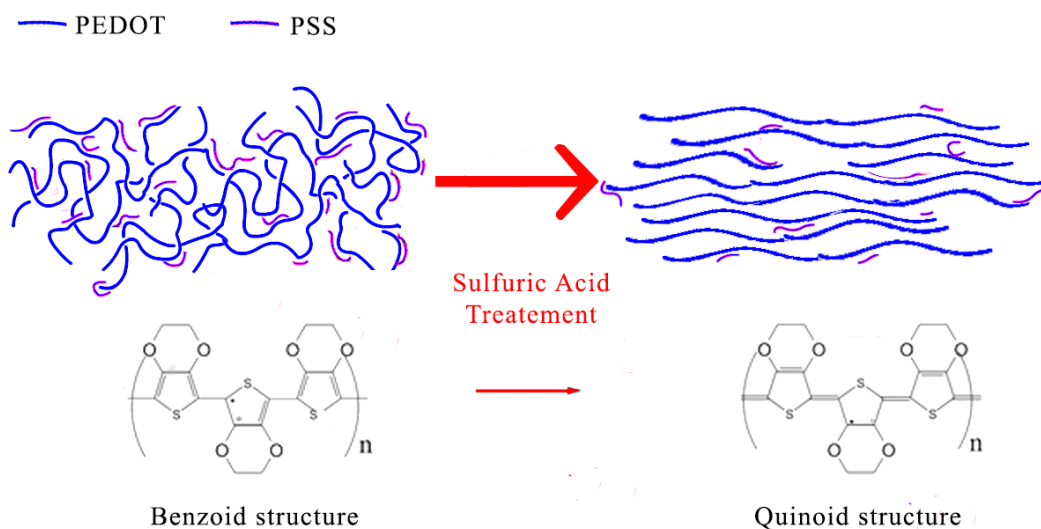


Figure 18: Conformation evolution scheme of PEDOT:PSS caused by acid treatment.

The evaluation of the structural features of the Clevios™ PH1000 and treated PEDOT:PSS samples were conducted through Raman spectroscopy by a Renishaw inVia Raman microscope (Renishaw, UK) equipped with a Leica DMLM microscope with a 50× objective. The spectral resolution of the instrument is 1 cm^{-1} .

Raman spectra for these two materials are deconvolved with Lorentian line functions and are shown in Figure 19A, B. The spectra are acquired between 950 and 1800 cm^{-1} and are normalized to the predominant feature at about 1440 cm^{-1} .

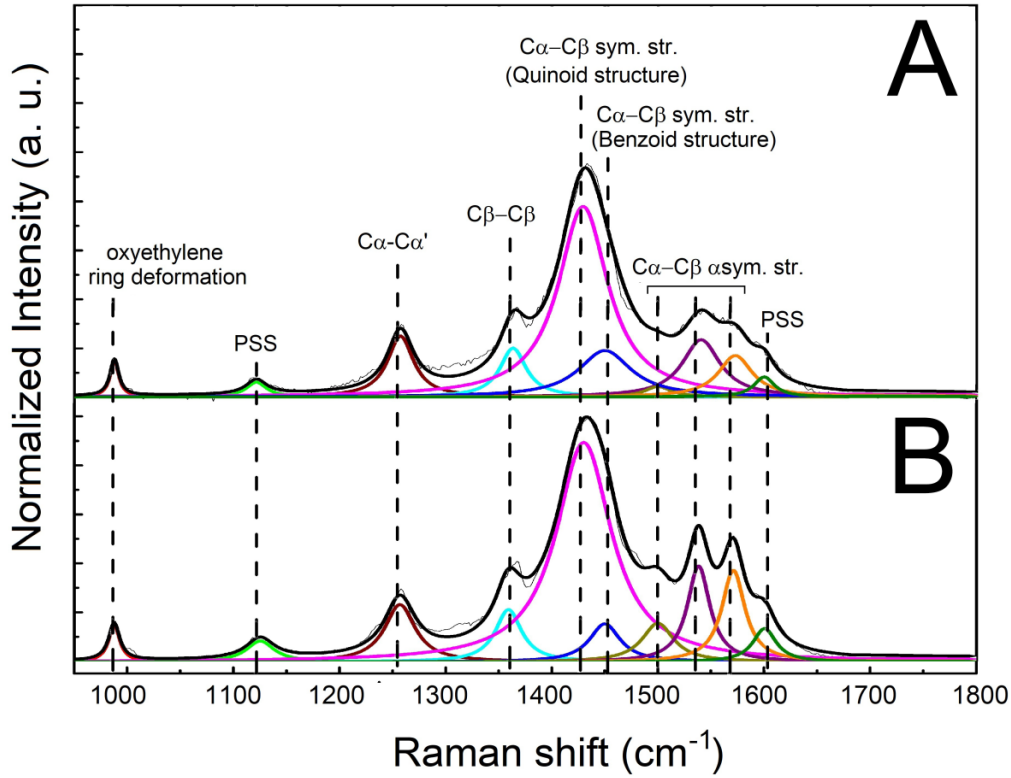


Figure 19: Raman spectra of A) pristine filler (Clevios™ PH1000) and B) treated filler.

As reported in the Figure 19A, except for the features related to PSS at 1120 and 1605 cm^{-1} , all the peaks in the spectrum can be attributed to PEDOT.

The peaks related to PEDOT at 990 , 1270 and 1362 cm^{-1} are assigned to the oxyethylene ring deformation and to the $C\alpha-C\alpha'$ and $C\beta-C\beta'$ inter-ring stretching vibrations, respectively. The bands at 1504 cm^{-1} and 1568 cm^{-1} were attributed to the asymmetric stretching vibrations of the $C\alpha=C\beta$ of thiophene rings in the middle and at the end of PEDOT chains, respectively. The splitting of these two modes produces the broad peak at 1534 cm^{-1} .

Considering that PEDOT chains can be arranged in a coil-like benzoid or in an extended quinoid structure, the features at about 1440 and 1460 cm^{-1} are assigned to the quinoid $C\alpha-C\beta$ and benzoid $C\alpha=C\beta$ symmetric stretching modes. The extended quinoid conformation provides a closer packing of the PEDOT particles[140][141] in which the π -electron delocalization is facilitated and noticeable charge transport properties of the conductive resin can be achieved. Therefore, conformational information of the PEDOT chains can be gained by analyzing the peaks related to the quinoid $C\alpha-C\beta$ and benzoid $C\alpha=C\beta$ symmetric stretching modes. Then, the evaluation of the percentage content of PEDOT in the extended quinoid conformation (% Quinoid), was determined by using equation 4[142]:

$$\text{Eq. 4} \quad \% \text{ Quinoid} = \frac{I_{\text{Quinoid}}}{I_{\text{Quinoid}} + I_{\text{Benzoid}}} \cdot 100$$

The Raman integrated intensity values of the quinoid $C\alpha-C\beta$ and benzoid $C\alpha=C\beta$ symmetric stretching modes were indicated with I_{quinoid} and I_{benzoid} respectively. The % Quinoid values of 83% and 90% were respectively obtained for pristine and treated PEDOT:PSS materials, evidencing that the employed treatment induces the conformational alteration of PEDOT chains from coil-like to linear structures. The molecular arrangement induced in PEDOT:PSS samples by the acidic treatment involves a predominance of PEDOT chains in linear structures; this result is confirmed with FESEM analysis (chapter 3.9).[143]

The protons of H_2SO_4 neutralize some PSS^- ions to $PSSH$, producing the weakening of coulombic interaction with PEDOT grains.[144] As a consequence, the PSS^- units are replaced by $H_2SO_4^-$ as the counter ions, determining a reduction in the number of the PSS^- ions, as indicated by the decreasing ratio value between the integrated area of the peaks related to the $C\alpha=C\beta$ vibrations in the thiophene rings and the bands related to PSS.

The interaction of PEDOT with H_2SO_4 leads to a well phase segregation between poly(3,4-ethylenedioxythiophene) and polystyrene sulfonate, resulting in a rearrangement of the PEDOT polymer chains in a linearly oriented structure (quinoid conformation), which increases the charge transfer among the PEDOT units, leading to a significant enhancement in the electroconductivity.[145]

In the end, a Raman spectrum (with the same operating condition previously reported) of PEGDA 575 with 1% wt. of PI, 5% wt. of DMSO and 45% wt. of treated PEDOT:PSS blend resin was reported in Figure 20. The Raman spectrum of the printed conductive resin exhibits further peaks designated by blue dotted lines and attributable to the PEGDA 575 chains. This finding confirms that the resin is constituted by PEGDA 575 and treated PEDOT:PSS fully mixed together, as indicated by the SEM results (chapter 3.9).

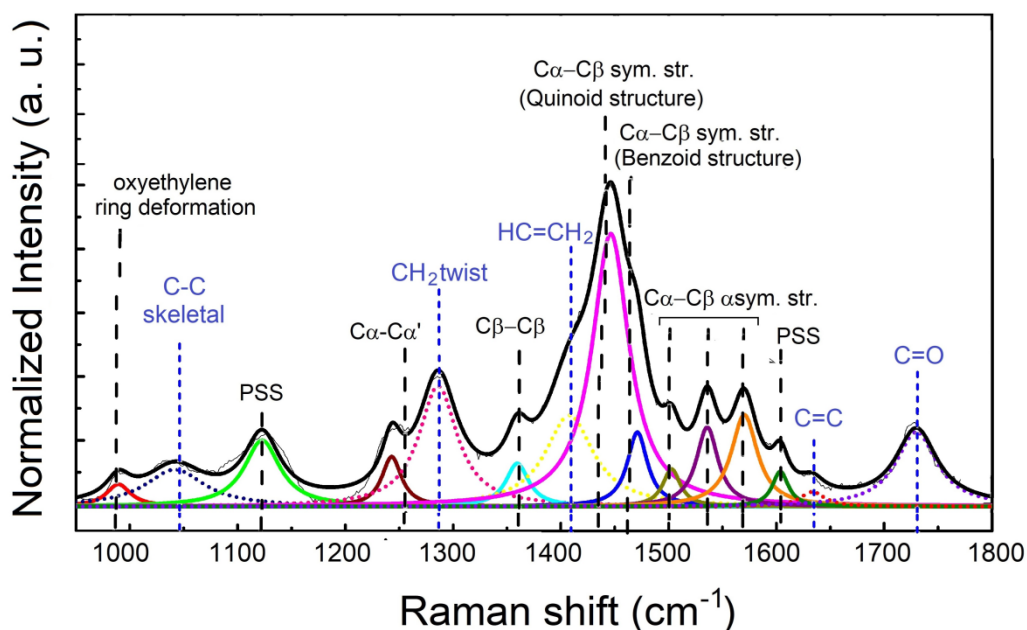


Figure 20: Raman spectrum of PEGDA 575 with 1% wt. of PI, 5% wt. of DMSO and 45% wt. of treated PEDOT:PSS.

With regards to the conductive blend, the %Quinoid value of 88% was calculated (using the previous formula), pointing out that the structural features of the treated PEDOT:PSS particles are maintained after the printing process. This evidence indicates that the printed resin exhibits good electroconductivity properties.

The broad features of the conductive resin blend in the Raman spectra suggest the presence of short PEGDA 575 chains and indicate the formation of amorphous domains.[146] However, an integrated intensity ratio value of 5 between the peaks related to the carbonyl group and the C=C stretching vibrations was calculated, indicating a significant crosslinking of acrylate.[147]

3.9 Field emission scanning electron microscope characterization

Materials with different micro and nanostructures can show different physical and mechanical properties. For this reason, in this study, the first priority was to find the correlation between properties and microstructure. The materials arrangement will determine their behaviour, and the properties of materials can reveal their microstructure.[148][149]

Field emission scanning electron microscope (FESEM) investigations were conducted on the treated PEDOT:PSS samples and the printed PEGDA 575 with 1% wt. of PI, 5% wt. of DMSO and 45% wt. of treated PEDOT:PSS.

The morphological structures of these samples were investigated by field emission scanning electron microscope (FESEM) analysis with ZEISS Merlin and Supra 40 operating at 200kV. For FESEM characterizations, the treated PEDOT:PSS samples were dropped and dried at room temperature on a TEM grid after dilution (1:5) with ethanol to achieve a better material suspension and then improve the quality of high-resolution FSEM imaging.

First, we conducted a morphological comparison of the two samples, pristine and treated CleviosTM PH1000 materials, through electron microscopy. In Figure 21A, B and in Figure 21C, D the FESEM characterization of pristine and treated PEDOT:PSS is reported at two different magnifications respectively. The comparison between Figure 21A, C highlights the morphological change of the filler material after the precipitation process.

In the inset of Figure 21B a higher magnification FESEM of pristine PEDOT:PSS is reported, while the inset of Figure 21D is a high-angle annular dark-field scanning transmission electron microscopy (STEM HAADF) image of CleviosTM PH1000 after acidic treatment, further confirming the crystallization process occurred during the treatment with sulphuric acid.

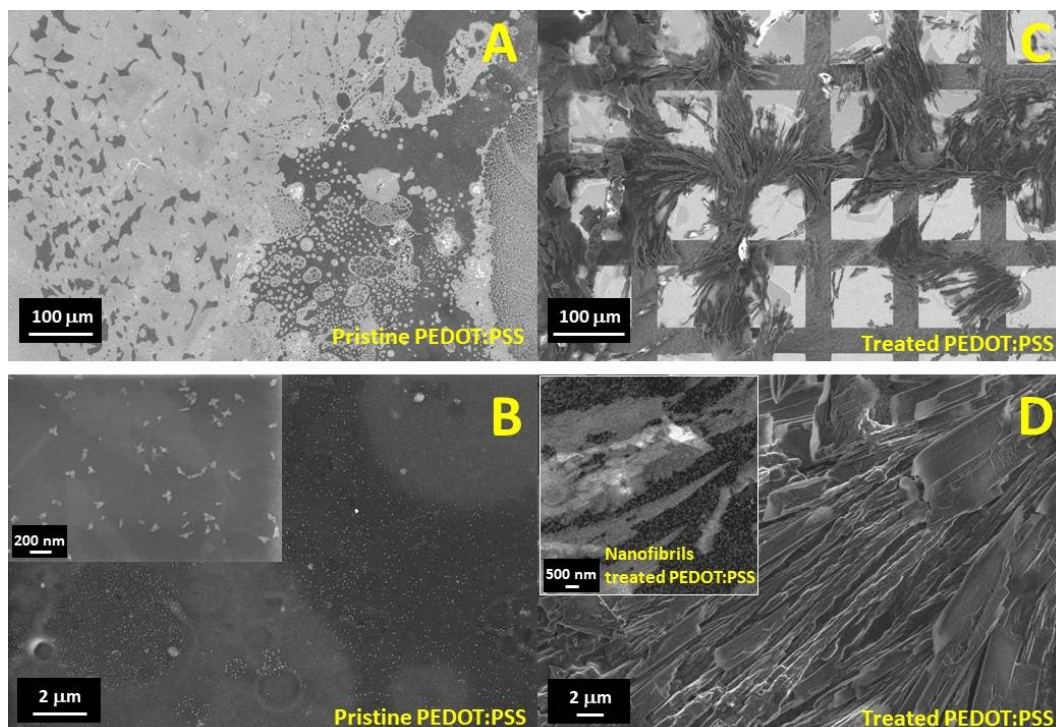


Figure 21: (A, B) FESEM images of pristine PEDOT:PSS at two different magnifications. (C, D) FESEM images of treated PEDOT:PSS at the same two magnifications. In the inset of Figure 21B higher magnification FESEM of PEDOT:PSS is reported, while the inset of Figure 21D is a STEM HAADF image of PEDOT:PSS after acidic treatment.

In the end, an investigation of the morphological features of the treated PEDOT:PSS and the conductive resin based on PEGDA 575 with 45% wt. of treated PEDOT:PSS are respectively reported in Figure 22A, B.

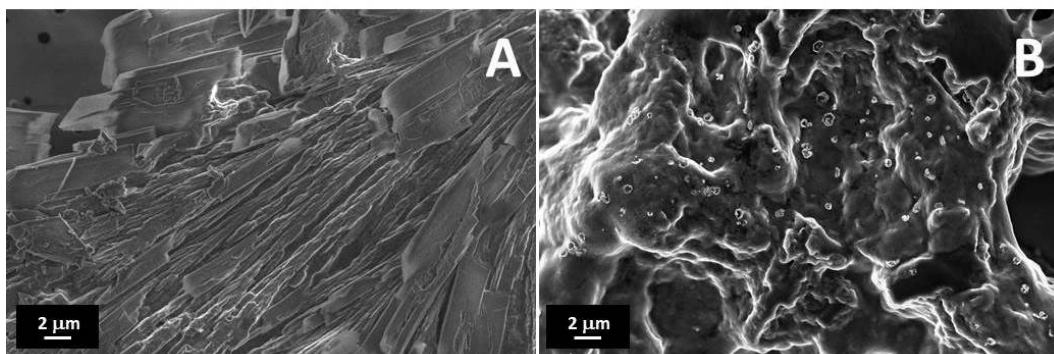


Figure 22: FESEM images of: A) treated Clevios™ PH1000 B) PEGDA 575 with 1% wt PI, 5% wt. of DMSO and 45% wt. of treated PEDOT:PSS.

The Figure 22A, shows a clear evidence of columnar structures formation on treated PEDOT:PSS sample, attributable to the rearrangement of PEDOT:PSS into nanofibrils after H_2SO_4 treatment.[150]

The FESEM image of the PEGDA 575 with 45% wt. of treated PEDOT:PSS resin blend in Figure 22B shows a homogenous morphology of the resin constituted by amorphous domains. Considering that the resin is produced with 45% wt. of treated PEDOT:PSS, the absence of the columnar structures

related to the PEDOT:PSS phase and the uniformity in the morphology of the blend denotes the formation of a mixture without phase separation. Then, it is possible to confirm that the chemical formulation of the resin with 45% wt. of treated PEDOT:PSS is suitable to produce the 3D-printed conductive object with complex geometries.

3.10 Printing parameters optimization

The fruitful additive manufacturing process depends upon the appropriate selection of process factors. Using the optimized printing parameter, it is possible to print devices with complex structure or specific mechanical[151], thermal[152] and conductive[153] properties. Hence, for each type of polymer used in AM it is necessary to find the process variables needed to be controlled and optimized precisely.

Figure 23 shows optical photographs of two samples based on PEGDA 575 with 1% wt. of PI, 5% wt. of DMSO and 45% wt. of treated PEDOT:PSS blend printed under various operating conditions. Figure 23A shows a good geometry obtained by optimum printing conditions since the CAD geometry is fully reproduced with a small error area; instead, a pattern without optimization of printing settings is reported in Figure 23B where it is possible to observe the blend over exposure (red line) and the CAD geometry (green line).

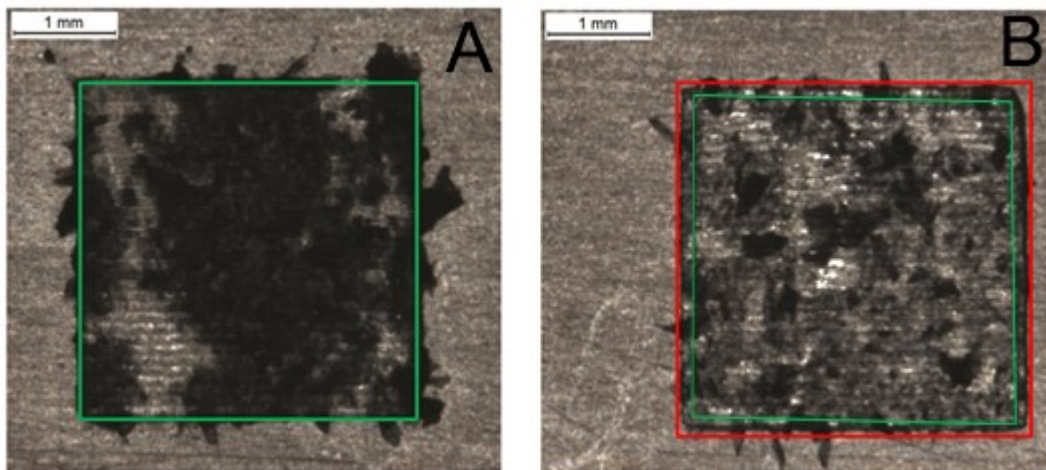


Figure 23: Shows two samples: A) optimal resin parameters (2000 mm/s laser scan velocity, 50 mW laser power), while. B) the printed layer in the worst case (500 mm/s laser scan velocity, 75 mW laser power).

The laser scan velocity and laser power parameters were investigated. Different planar square samples of $3 \times 3 \text{ mm}^2$ were printed using the SL printer (chapter 3.1). The parameters values are reported in Table 2.

The distance of printed lines and the treated PEDOT:PSS particles can be noticed in Figure 23A. In Figure 23, it is possible to understand that the dimension of the particles can directly affect the mechanical behavior of the printed samples.

It can be influenced by many other aspects, such as infill degree, layer thickness, raster angle, or morphological imperfection.

Some samples were printed for each parameter combination and the average area (A) of the polymerized resin was calculated using ImageJ[®] software. Several sample pictures were acquired with a standard optical microscope (Leica Microsystems Heidelberg, Germany). These pictures were uploaded on ImageJ[®] software and the scale bar was set. Then, tracing the sample geometry was determinate the number of pixels inside it and subsequently it was possible measured the samples area.

The area value (A) was used to find the percentage error with respect to the nominal value ($A_{nominal}$), using Equation 5 reported below.

$$\text{Eq. 5} \quad \text{erro \%} = \left(\frac{|A_{nominal} - A|}{A_{nominal}} \right) \cdot 100$$

The percentage error was reported in table 2.

		Laser power density (mW/mm ²)			
		5	25	50	75
Laser scan velocity (mm/s)	500	0.28	5.25	6.51	12.3
	1000	7.97	-	1.13	4.65
	2000	-	-	0.03	8.16

Table 2: percentage error area using PEGDA 575 with 1% wt. of PI, 5% wt. of DMSO and 45% wt. of treated PEDOT:PSS.

Using 50 mW/mm² and 2000 mm/s two complex 3D shapes were printed: the first sample (Figure 24A) is a double ring chain (0.5 mm thickness with 10 mm diameter); the second (Figure 24B) is a conductive 3D microwall (15 mm maximum wall height with 3 mm thickness and 5 mm minimum wall height with 350 μm thickness). After printing and cleaning in 2-propanol, the objects were cured for 10 minutes under a UV lamp. The use of this 3D object demonstrated the suitability of this new resin formulation for SL printing. Moreover with this resin is possible to print complex 3D shapes, beyond the limits of 2D patterning (photolithography, ink-jet printing, aerosol jet printing, etc).

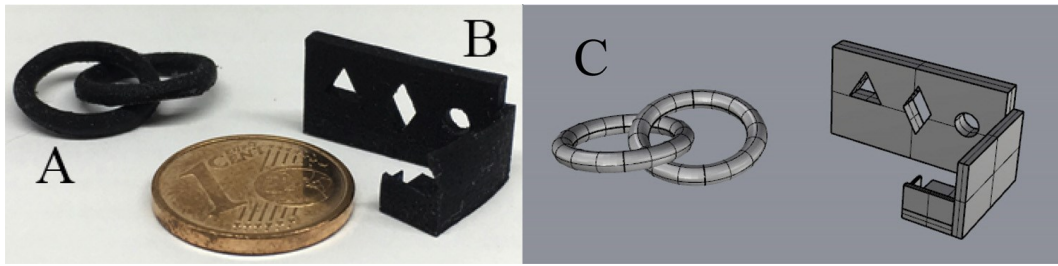


Figure 24: Conductive PEGDA 575 with 1% wt. of PI and 45% wt. of treated PEDOT:PSS 3D printed test samples: (A) Ring chain, (B) micro and macro walls structures combined with holes and undercuts (printing parameters: 50 mW/mm² laser power, 2000 mm/s scan velocity) and (C) 3D layout.

3.11 Mechanical characterization

The fillers presence produces a heterogeneous blend inside a polymeric resin. The resulting blend has widely varying elastic and viscoelastic characteristics.

Unfortunately, a unique approach to measure the rigidity of printed material for photocurable resin is not actually defined. For this reason, compression or tensile tests, with specific handle and models [154][155], are used to measure the Young modulus for 3D printed structures.

With the aim to characterize the elastic behaviour, usually two standard mechanical testing procedures are used, i.e. the ASTM D638[156] or ISO 527-1:2012.[157]

In this work the ISO 527-1:2012 standard guide was used to define the shape and other mechanical test parameters.

A tensile test was then performed on PEGDA 575 with different amounts of treated PEDOT:PSS (0, 25, 35, 45% wt.).

The tensile test was performed by Instron 3366 dynamometer (Instron Corporation, USA) equipped with a load cell of 500 N. The tests were conducted at a crosshead speed of 1 mm/min at room temperature and 3 samples each were used for all the above combinations.

Figure 25 shows the 3D printed samples for the mechanical tests ($1 \times 5 \times 30 \text{ mm}^3$). The PEGDA 575 with 1% wt. of PI and PEGDA 575 with 1% wt. of PI, 5% wt. of DMSO and treated PEDOT:PSS blend showed a brittle material behaviour (Figure 26).

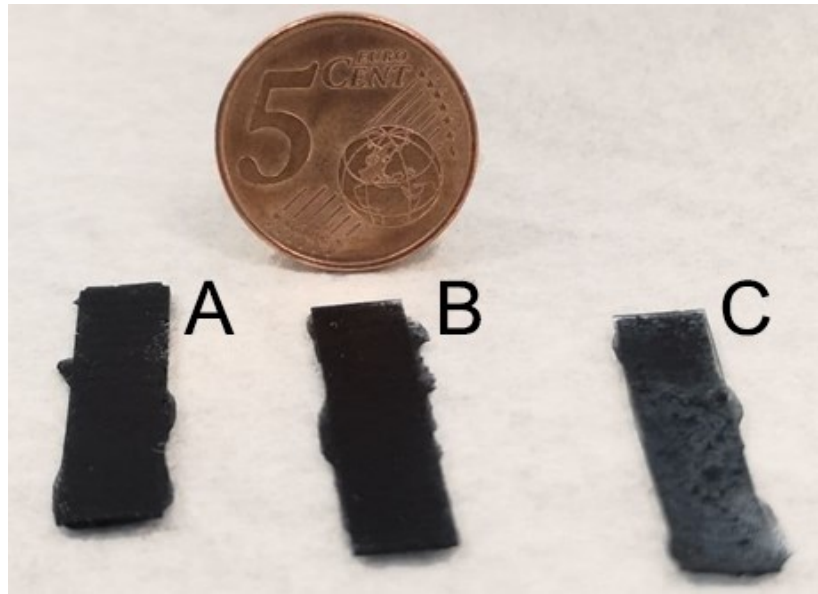


Figure 25: Samples for mechanical tests of PEGDA 575 with 1% wt. of PI and 45% wt. of treated PEDOT:PSS with A) 45% wt. B) 35% wt. C) 25% wt.

Equation 6 is used to calculate the strain (ε),

$$\text{Eq. 6} \quad \varepsilon = \frac{\Delta l}{l_0}$$

where l_0 is the initial height and Δl is the crosshead displacement of the sample. The elongation stress σ (MPa) was considered as the ratio between the applied elongation force (N) and the nominal initial cross section area (mm^2) of the sample.

Figure 26 shows the Young modulus of PEGDA 575 with different percentages of treated PEDOT:PSS. It is well-known that the theoretical and experimental elastic modulus of PEGDA is in the range of 0.19–125 MPa[158][100][159] whereas the PEDOT:PSS (Clevios™ PH1000) shows a Young modulus around 90 MPa.[160]

The elastic modulus of PEGDA and treated PEDOT:PSS is significantly different for each of the percentages tested and it decreases with increasing filler content. For the blend resin, the stress-strain plot shows a linear viscoelastic region where the elastic modulus was calculated.

These results indicate that the samples are becoming less rigid (i.e., failure or breaking apart) as filler percentage increases. It is clear from Figure 26 that the pure PEGDA matrix shows a viscoelastic behaviour[161] moreover, the PEGDA:PEDOT blend shows a brittle behaviour increasing the filler content.[162]

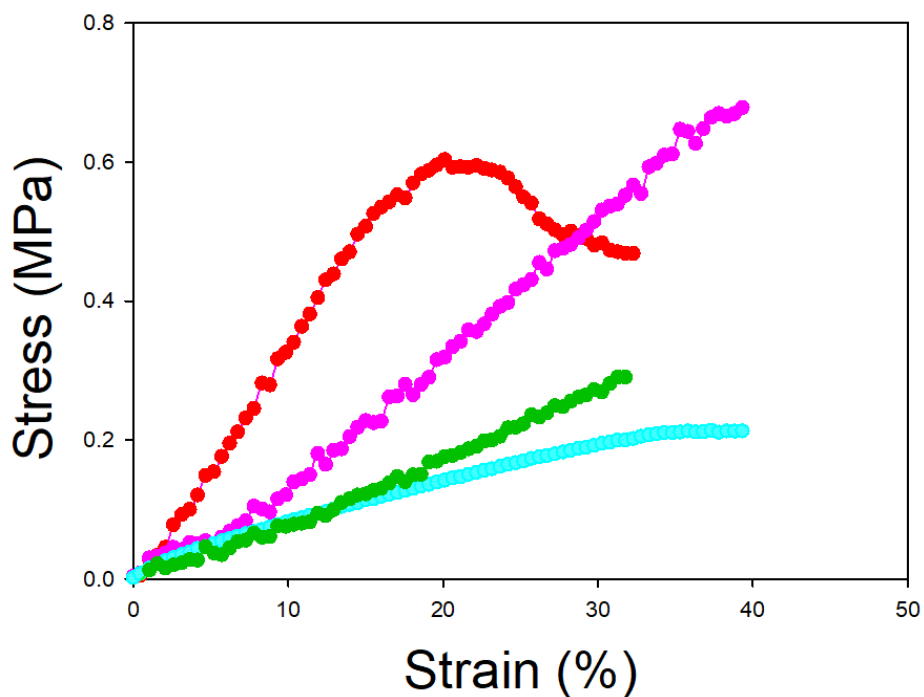


Figure 26: Stress-strain diagrams for different samples with PEGDA 575 with 1% wt. of PI and (red line)0%, (pink)25%, (green line)35%, (azure line)45% wt. of treated PEDOT:PSS.

Figure 27 shows the elastic modulus value of PEGDA 575 with different percentage of treated PEDOT:PSS. Those value were obtained analysing the slope of the regression curve in the linear loading part of the experimental curves.

The results with less percentage of treated PEDOT:PSS show an high material rigidity that is also attributed to the high degree of crosslinking interaction between the PEGDA 575 matrix network.

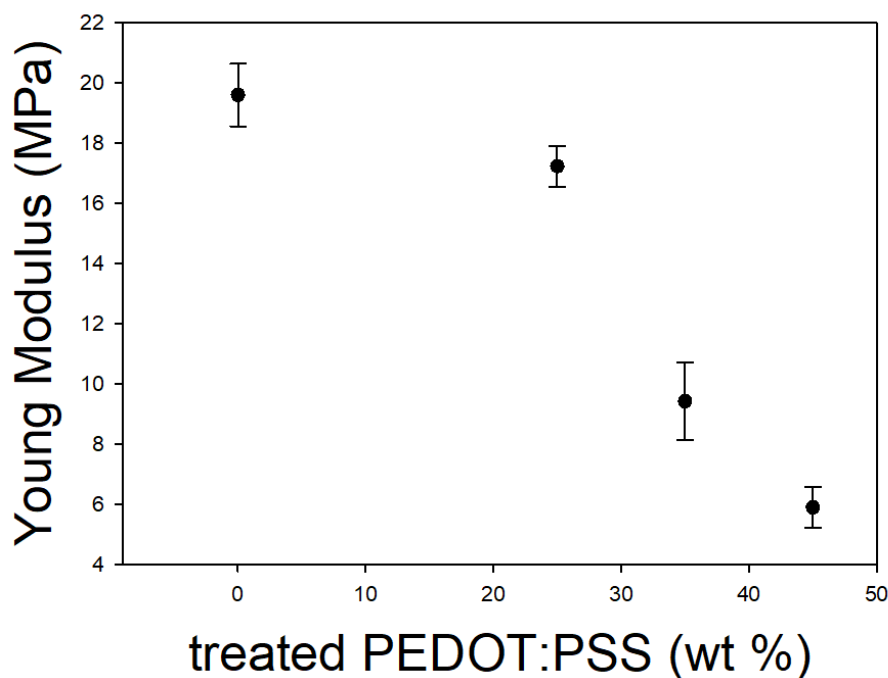


Figure 27: Young modulus values of PEGDA 575 with 1% of PI and 25%, 35%, 45% wt. of treated PEDOT:PSS.

It is clear from the results that the tensile strengths of PEGDA and treated PEDOT:PSS decrease with increasing filler content ratios. This could be explained with two reasons. First, the non-homogeneous matrix network causes a discontinuity of the mechanical property inside the blend. Second, there is a weak adhesion between the acrylate matrix and fillers that leads to possible crack formation points.

The estimated elastic modulus of PEGDA 575 with 1% wt. of PI is 21 MPa while the PEGDA 575 with 1% wt. and 25%, 35%, 45% wt. of treated PEDOT:PSS, was found to be 17.24, 9.41 and 6.02 MPa respectively.

3.12 Contact Angle

Surface characteristics of material such as surface roughness, hydrophilicity/hydrophobicity, charge density and surface energy can be greatly influenced by the filler presence inside the polymer matrix.[163]

One of the most common measurement used to characterize the surface of a new material is the contact angle, which is based on the equilibrium of three phase boundary (usually is a solid-liquid-vapour system).

The PEGDA 575 molecules are neutral and have a randomly-coiled structure. Previous works in literature demonstrated that PEGDA 575 matrix shows a hydrophilic behaviour, indeed the contact angle is 80°.[164][165]

Also for the PEDOT:PSS several different values are reported in literature, in fact it has a contact angles ranging from 10°[166] to 52°.[167]

With this point of view, measurements of contact angles were carried out on 3D printed PEGDA 575 with 1% wt. of PI and PEGDA 575 with 1% wt. of PI, 5% wt. of DMSO and 45% wt. of treated PEDOT:PSS samples. The measurements were performed by sessile drop (SD) technique, where a water drop is placed on a substrate and the static contact angle(SCA) is measured using a camera (Figure 28). The surface wettability can be investigated measuring the static contact angle between the gas–liquid and the solid–liquid boundary. Assuming that the substrate surface is flat and regular, the SCA measured can be determined by Young’s equation(eq7):

$$\text{Eq. 7} \quad \gamma_{SG} = \gamma_{SL} + \gamma_{LG} \cdot \cos \theta_C$$

In this equation the θ_C represents the static contact angle. The interfacial tensions of solid–gas is γ_{SG} , the interfacial of solid–liquid is γ_{SL} and liquid–gas interface is represented by γ_{LG} .

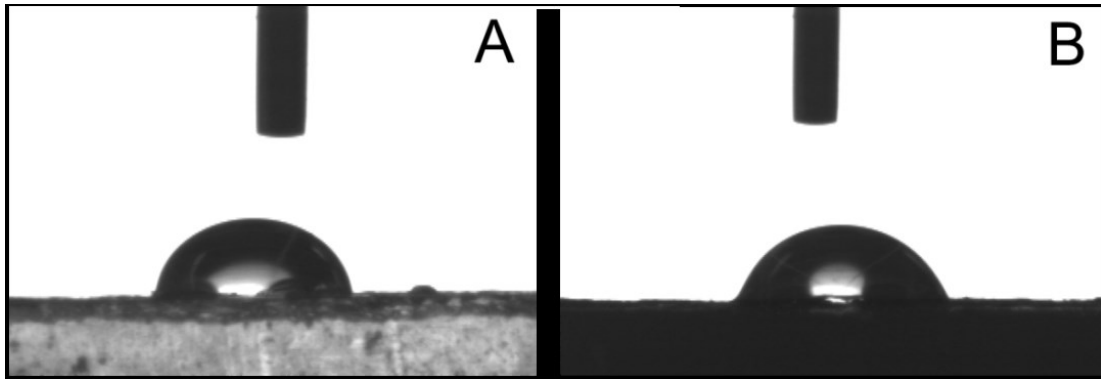


Figure 28: Side view of sessile drop technique A) PEGDA 575 with 1% of PI. B) PEGDA 575 (1% wt. of PI + 5% wt. of DMSO) with 45% wt. of treated PEDOT:PSS.

Measurements were acquired using OCA H200 Dataphysics equipment at room temperature. Contact angle tests were carried out dropping pure water on the 3D printed material surface ($5 \times 5 \times 10 \text{ mm}^3$).

A 1 μL dH_2O water droplet was gently placed by an automatic syringe on the printed material. Using the CCD camera four droplets depositions on different regions of each material were recorded and the contact angle was measured. The Wu correction[168] was implemented for surface energy calculation and the results are reported in Figure 29.

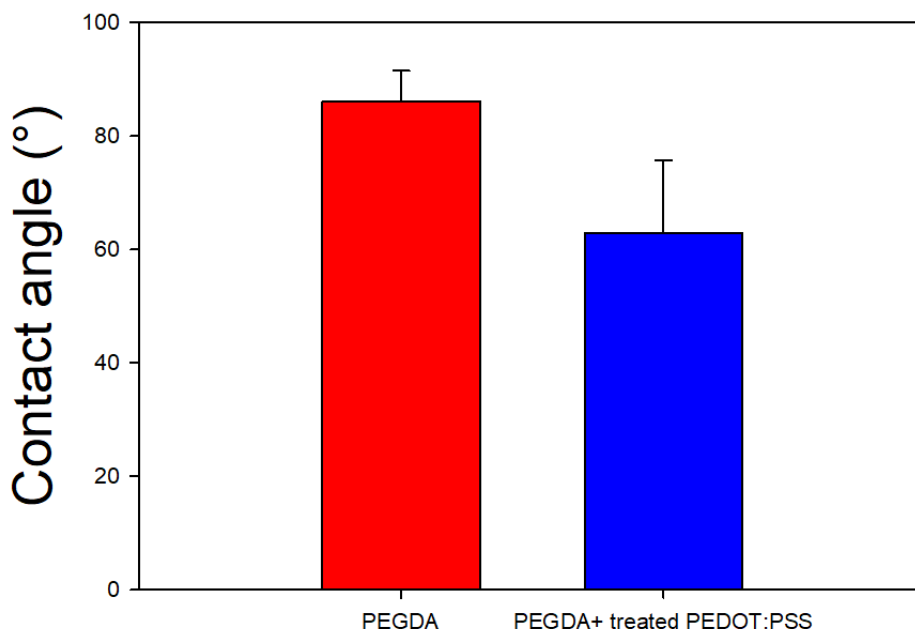


Figure 29: Contact angle measurement on PEGDA 575 with 1% wt. of PI and PEGDA 575 with 1% wt. PI, 5% wt. of Dimethyl sulfoxide and 45% wt. of treated PEDOT:PSS.

The results above presented show the measurements of PEGDA 575 with 1% wt. of PI and PEGDA 575 with 1% wt. PI, 5% wt. of DMSO and 45% wt. of treated PEDOT:PSS by the SD. Indeed for the PEGDA 575 matrix the contact angle is $(86.1 \pm 5.4)^\circ$. The addition of conductive filler inside the matrix makes it less hydrophobic obtaining $(62.9 \pm 12.8)^\circ$; this behaviour is akin to CleviosTM PH1000.[169]

Although the surface irregularity of the 3D printed material on the equilibrium contact angle can be important[170], in this work it was not considered, because there is a strict congruence with other values reported in the literature.[165][164][171]

3.13 In vitro cell tests

Although 3D printing by photopolymerization offers many advantages and could be a very promising technology, it is still limited in the biological applications due to the low biocompatibility of some components.[172] Indeed the resins and photoinitiators used in this field are often toxic and the presence of unreacted products after the polymerization can damage the cell's regulatory mechanisms.[173][174] In addition, SL resins have a three-dimensional network that is able to swell large amounts of water.[175]

For these reasons, the biocompatibility of the composite resins, object of this work, was studied. However, for this analysis it was necessary to use another matrix, such as PEGDA 250, because using a polymer with a shorter chain allows reducing the swelling effect.[176]

Swelling of the PEGDA 250 with treated PEDOT:PSS was characterized. When soaked in a solvent solution, the devices based on PEGDA usually start to absorb the liquid within the polymer matrix.

This process can change the morphological and physical properties of the sample that can produce a cytotoxic effect in cell cultures.

For this reason, the swelling properties of PEGDA 250 and treated PEDOT:PSS were studied. Three disks were immersed in 30 mL water at room temperature. Each sample was gently dried, at different times, using a napkin and the weight was measured.[177] In Figure 30 the normalized mass gain corresponding to water absorption was reported. The maximum mass gain was reached for the PEGDA 250 with treated PEDOT:PSS filler after 9h in dH₂O.

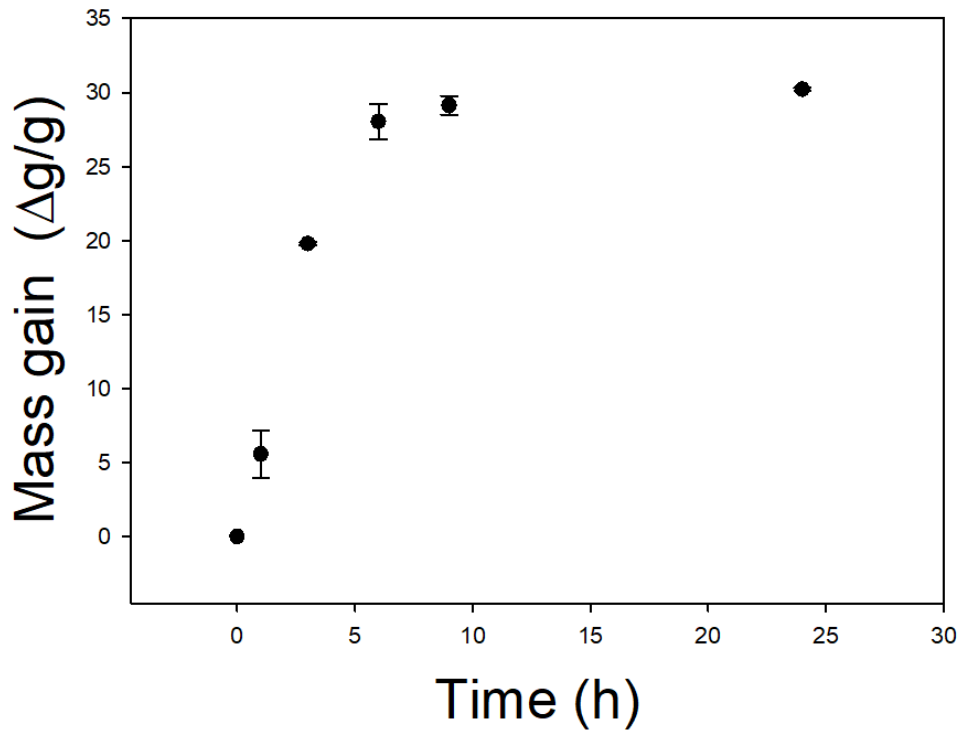


Figure 30: Swelling ratio of PEGDA 250 with 45% wt. of treated PEDOT:PSS

Using this data, the equilibrium mass swelling ratio can be calculated:

$$\text{Eq. 8} \quad Q = \frac{W_s}{W_d}$$

Where W_s and W_d are the highest swelling mass weight and the dry starting samples weight, respectively. The percentage of the equilibrium mass swelling ratio, Q , was calculated around 30%.

In the following, 30 discs (diameter 1 cm and thickness 3 mm) were produced using a PDMS mold and cured under the UV light for 10 min. Subsequently, these samples were cleaned with an ultrasound bath (59 kHz) for 10 minutes in pure ethanol and then dried under UV light for 10 minutes per side. Finally, the samples were soaked overnight in ethanol.

The treated PEDOT:PSS filler was purified to decrease the presence of sulphuric acid and contaminants traces, as reported in the literature[178][179], following the recipe described below:

1. Overnight soaking in 300 mL of ethanol
2. Discard the supernatant after the centrifugation for 10 min at 6000 rpm
3. Ultrasonication for 10 minutes (5s ON and 5s OFF with 70% of amplitude) in ethanol
4. Discard the supernatant after the centrifugation for 10 min at 6000 rpm
5. Stirring in ethanol at 600 rpm for 1h at 120 °C
6. Discard the supernatant after the centrifugation for 10 min at 6000 rpm
7. 3 days in 500 mL of washing buffer ($\frac{3}{4}$ dH₂O + $\frac{1}{4}$ ethanol)
8. Discard the supernatant after the centrifugation for 10 min at 6000 rpm
9. Ultrasonication in continue mode for 15 min with 55% of amplitude
10. Discard the supernatant after the centrifugation for 10 min at 6000 rpm
11. Stirring at 120 °C 1h with 600 rpm
12. Wash the slurry in ethanol and centrifugation for 10 min at 6000 rpm

The lung cancer epithelial cells A549 were chosen to study the in vitro cells test, because they do not retain the structural or functional characteristic of the tissue from which they were derived, subsequently making them good candidates for biocompatibility studies.

For MTT assay, 1.5×10^5 cells were seeded on each disk and incubated in RPMI 1640 at 37 °C. After the incubation time (1 day and 2 days), the DMEM was removed and the same volume of fresh medium and MTT (1 mg/mL dissolved in PBS) were added in each well. Subsequently the multiwell was incubated for 2 h at 37 °C. In the end 250 μ L of MTT solvent (10% SDS, 0.01 M HCl in dH₂O) was added in each well ad it was incubated again for 120 min at 37 °C. The colorimetric signal (absorbance) of the multiwell was read using a Synergy™ Microplate Reader (HTX, BioTek, Winooski, VM, USA) at a wavelength of 570 and 650 nm. The signal intensity is proportional to the number of proliferating cells and it is reported in Figure 31, where the error bars show mean SD.

All the measurements showed no significant differences in cells proliferation after 24h, regardless of the treated PEDOT:PSS amount. This is most likely due to the effectiveness of the filler, which induce a cytotoxic response as clearly represented in Figure 31. The cell viability after 24h was quite similar for all the samples. On the contrary, both Polystyrene and PEGDA 250 control samples clearly exhibited a more pronounced proliferation within cells compared to conductive PEDOT containing samples.

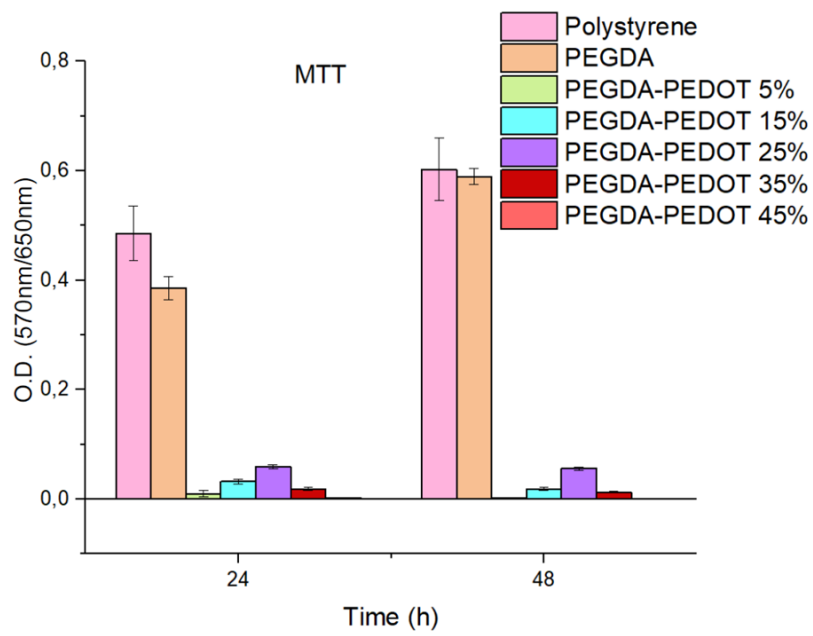


Figure 31: MTT assay on PEGDA 250 and different content of treated PEDOT:PSS; the results was obtained using the 570 nm wavelength subtracting the background (650 nm).

Chapter 4

Effect of volatile organic compounds adsorption on 3D printed PEGDA:PEDOT for long-term monitoring devices

4.1 Introduction

The always-growing number of pathologies due to environmental pollution has led to an enhanced interest on the main sources of exposure that could damage our biological system. This problem especially regards indoor pollution, like factories, laboratories, and so on.[180]

Such indoor pollutants are gases released from solids or liquids with low boiling point (e.g. organic solvents or solid fuels). Generally, these gases are called Volatile Organic Compounds (VOCs).

The electrochemistry was one of the first methods used to monitor the VOCs[181], but actually the cumulative adsorption effects is the most promising method[182] because no specific equipment and technical users are required. There are several types of such devices that can be suitable to verify the presence of organic solvents.[183][184] Some of these cumulative measuring devices (CMD) are able to modify their optical, chemical or electrical properties when exposed to VOCs. Especially the CMD that are able to change their conductivity have more advantages such as a simple measurement setup (for this class is necessary only an ohmmeter to collect the data) and easiness of integration with other systems.[185]

For this reason in the last 10 years more research groups tried the exploitation of conductive polymers in cumulative measuring devices. This approach can represent a auspicious solution to overcome the limitation of standard cumulative devices based on metal oxide, which require high power consumption for preparation and operation.[186]

In this chapter a CMD fabrication by SL 3D printing was studied, using the PEGDA 575 and treated PEDOT:PSS conductive blend system as possible active material for VOCs monitoring devices.

4.2 CMD fabrication

A cumulative measuring device was printed with PEGDA 575 with 1% wt. of PI and 45% wt. of treated PEDOT:PSS.

The CMD shape was designed to achieve a large surface interaction area in a tight volume. With this device we have indirectly demonstrated the possibility to print complex geometries and functional objects. Then a double helical structure was printed as two rods following a 360° turn along an 8 mm height. The circular section rod was 2 mm (Figure 32A), and some tiny temporary support structures were added around the structure Figure 32B, C, D. The structure was also equipped with two squared pads at its extremities to provide an easier contact during conductivity tests.

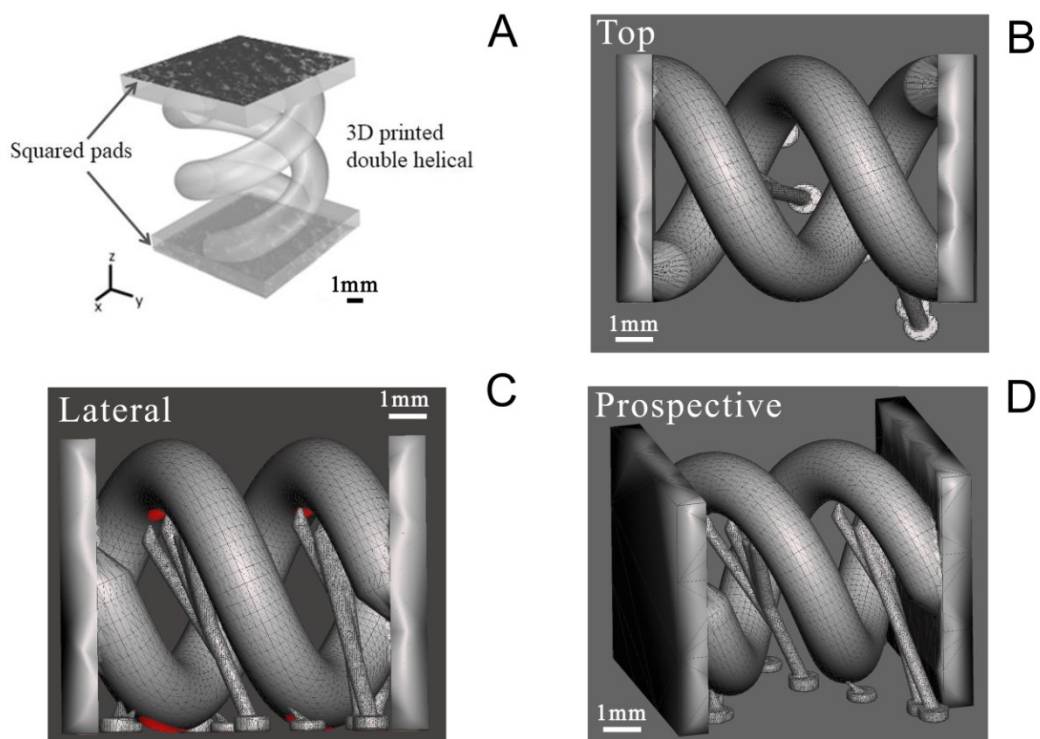


Figure 32: CAD drawing of double helix device. A) General view showing the pads for contact during electrical measurement; B) Top 3D view; C) Lateral 3D view; D) Prospective 3D view

In Figure 33 a double helix device obtained by SL printing is reported; for this device 50 mW and 2000 mm/s as laser power and scan velocity respectively

have been used. After the printing process the CMD was post cured under UV light for 10 minutes. The presence of treated PEDOT:PSS filler does not affect the photocuring ability of PEGDA 575 matrix as to assume defined 3D complex geometries.



Figure 33: 3D printed double helix structure based on PEGDA 575 with treated PEDOT:PSS blend (SL parameters 50 mW laser power, 2000 mm/s scan velocity).

4.3 Results

The double helical sample was exposed in a small gas chamber with a specific organic solvent (ethanol or acetone) in order to accurately assess the effect induced by vapor adsorption on conductive blend.

The surface drying time was defined by performing I/V measurements at controlled times after vapor exposure. The Figure 34 shows the conductivity values (σ) obtained for different drying times after 10 minutes of acetone exposure. The starting reference value of $\sigma \approx 0.055$ S/cm corresponds to the sample's conductivity without any exposure. Generally we can observe that the vapor adsorption induces a conductivity decrease inside the material.

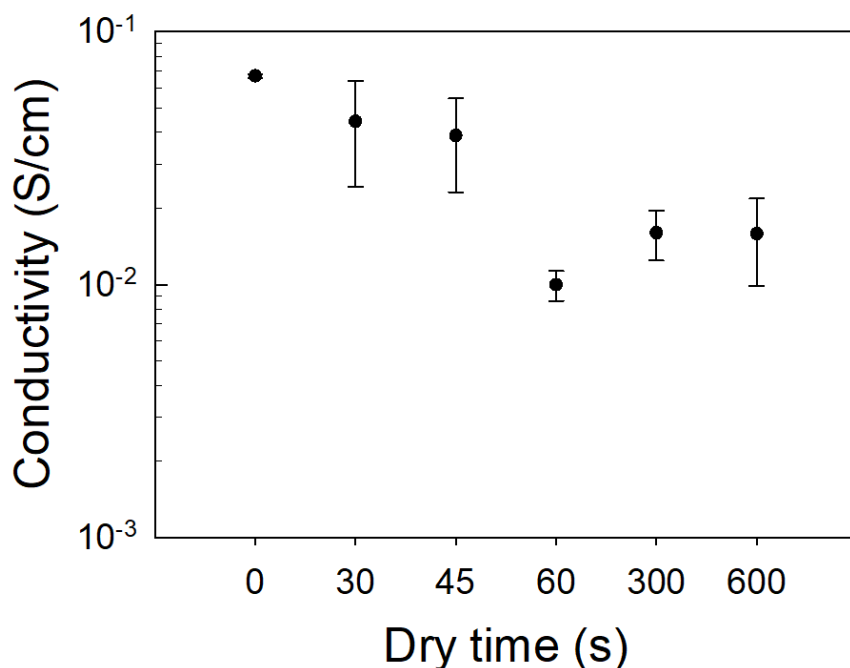


Figure 34: Conductivity of PEGDA and treated PEDOT:PSS subjected to a 10 minutes acetone exposure after different drying times.

The non-reproducible conductivity measurements with a drying time of 30 and 45 seconds are due to a not complete solvent evaporation from the surface of the samples. 60 seconds are needed for the first dry time to achieve a complete solvent evaporation, however it is not a stable value. Instead, a drying time of 300 seconds is the minimum to obtain plateau values and a good agreement between the results of I/V characteristics.

The vapors adsorption effect on PEGDA 575 with treated PEDOT:PSS samples was studied by performing current-voltage measurements after different exposure times to ethanol and acetone vapors (Figure 35). It can be seen from the graph that the conductivity of CMD significantly decreases after 10 minutes of exposure for both types of vapor. However, while acetone vapors cause a fast conductivity reduction with gradually increasing exposure times, the effect of ethanol is more limited. In particular, it can be observed a quasi-constant conductivity condition around 10^{-4} S/cm only after 20 minutes of acetone exposure. In particular, with long exposure times the conductivity changed from $13.7 \cdot 10^{-4}$ to $9.1 \cdot 10^{-4}$ S/cm for 60 and 120 minutes, respectively.

On the contrary, the printed CMD based on treated PEDOT:PSS require a long exposition (60 minutes) to reach a conductivity plateau of $13.5 \cdot 10^{-3}$ S/cm with an ethanol exposure.

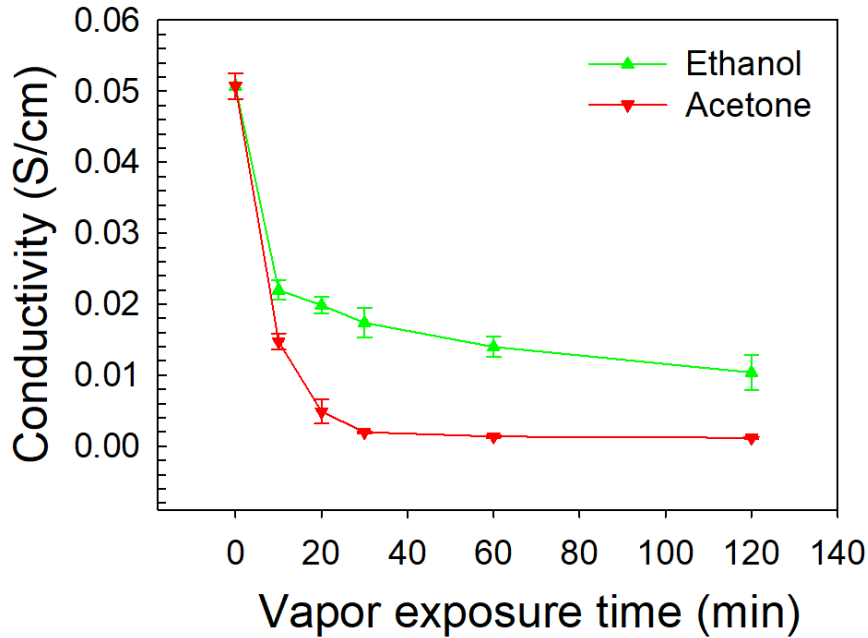


Figure 35: Conductivity of PEGDA 575 and 45% wt. of treated PEDOT:PSS for different exposure times to ethanol and acetone vapors.

The effect of VOCs on this printable conductive resin based on treated PEDOT:PSS is shown in Figure 36, where the normalized resistance variation of the samples versus acetone and ethanol vapor exposure time is reported.

In this case, the curve referred to acetone reaches the saturation after about 20 minutes, while the curve referred to ethanol after 60 minutes.

The continuously conductivity reduction induced by vapors exposure can be explained by the ability of the material to accommodate the vapor molecules. As previously reported in the chapter 3.8 from the structural analysis, the blend network is given by an interplay of PEGDA 575 and treated PEDOT:PSS chains that can be altered by the interaction with vapor molecules. In fact the VOCs penetrating the polymeric network could growth the distance between the treated PEDOT:PSS filler then destroying the conductive pathways they have formed inside the conductive blend.[187] The ethanol adsorption appears slower because this solvent is used during the purification of the pristine Clevios™ PH1000. More probably the charge transport reduction can be attributed to the modification of the PEDOT chains conformation due to interaction with the vapor molecules.[188][189]

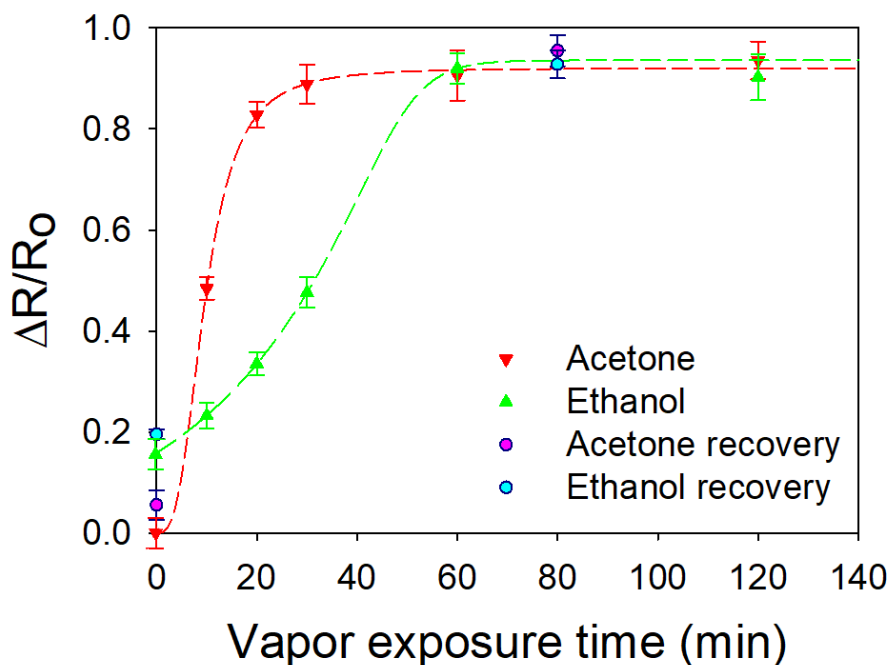


Figure 36: Normalized resistance variation of double helical samples versus acetone and ethanol exposure times.

The recovery capacity of PEGDA 575 and treated PEDOT:PSS was evaluated by subjecting the material to a mild heat treatment of 70 °C for one night at the end of which an electrical characterization was carried out again. After the heat treatment the $\Delta R/R_0$ values approach the normalized resistance variation values collected before acetone and ethanol exposure confirming the recovery behaviour of the produced material.(Figure 36)

Finally, a further characterization was achieved to evaluate the ability of the helicoidal geometry on the adsorption properties of the sample. In Figure 37 the resistance versus time diagram is reported for two different PEGDA 575 and treated PEDOT:PSS samples having the same mass and composition but different shape. In Figure 37A the response for a sample with a double helix structure is shown, while in Figure 37B the result for a sample with a rectangular parallelepiped shape is reported. It is evident how after 30 minutes of acetone exposure, the helical sample shows an increase in resistance about 4 times larger if compared to the rectangular sample, confirming that the greater exposed surface related to the helical structure actually favours the vapor adsorption process in the final material.

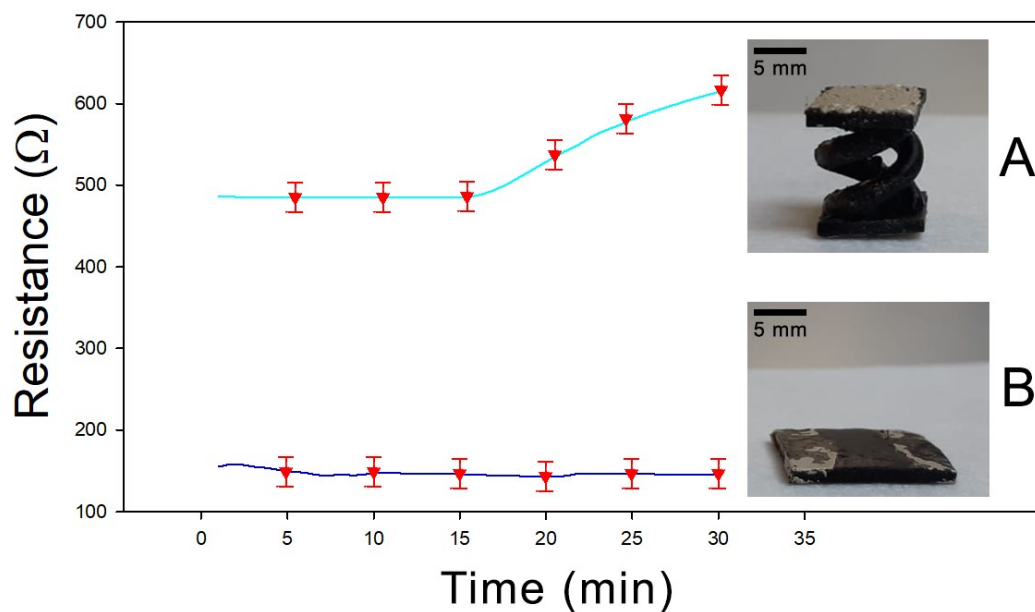


Figure 37: A) Resistance of 3D printed double helical device under acetone exposure B) Resistance of 3D printed parallelepiped design under acetone exposure.

After different solvents exposure the Raman spectra were acquired. The spectra were deconvolved in the region of $1200-1800\text{ cm}^{-1}$ by using Lorentian line functions. In all of these measurements, a broadening of the peaks with the increasing of the exposition time was observed (Figure 38A). Furthermore, it was observed that increasing the exposition time, the integrated intensity values of the peaks related to the $C\alpha = C\beta$ asymmetric stretching vibrations in the thiophene rings decreased.

The vapors exposure produces no substantial changes in the Raman features of PEGDA 575 chains (Figure 38A). In fact, after two hours exposure the signals related to PEGDA 575 are found notably broader and less defined. These results clearly suggest how PEGDA 575 behaves as a stable support matrix for the whole conductive blend.

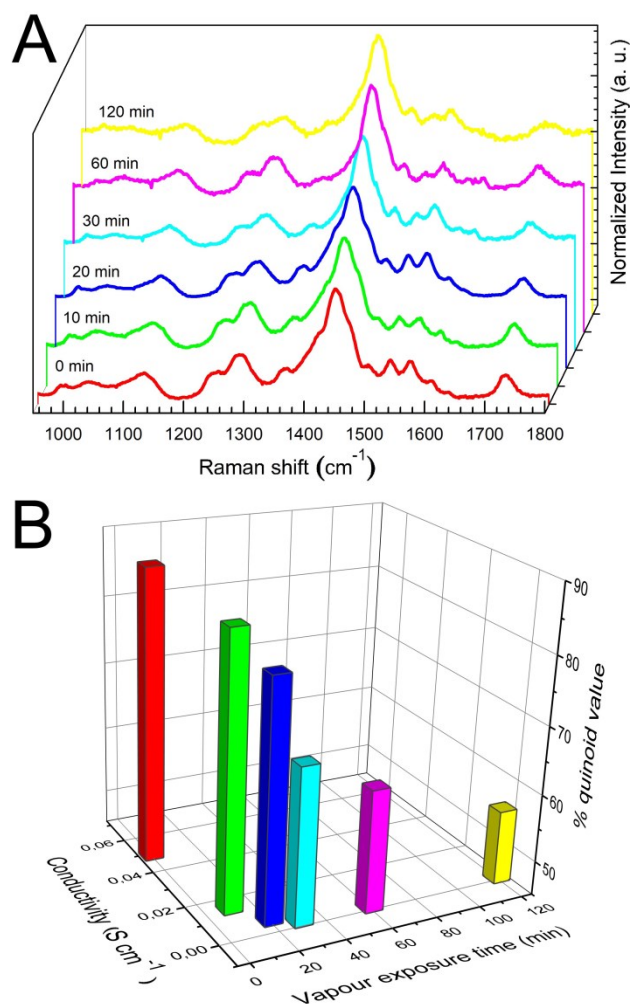


Figure 38: A) Raman spectra of PEGDA 575 with 45% wt. of treated PEDOT:PSS samples exposed to acetone vapors for 0, 10, 20, 30, 60 and 120 minutes; B) Conductivity and % quinoid value as a function of the vapor exposure time.

On the contrary, a large spectral signal variations of PEDOT chains are found as a function of the exposure time to the acetone vapors. To quantify the magnitude of such modifications inside the molecular structure in PEDOT chains, the percentage content of the extended quinoid was determined by using Equation 2.(Chapter 3.8)

The quinoid percentage values of 88, 85, 80, 68, 63 and 56 were obtained after exposure for 0, 10, 20, 30, 60 and 120 minutes, respectively. Observing the percentage decrease of the quinoid conformation in Figure 38B it is possible to confirm that the interaction with the acetone molecules induces a conversion to the benzenoid form of the PEDOT chains. This effect is a probable consequence of the electrostatic interaction between the polar sites of the solvent molecules and the positively charged sites of the oxidized PEDOT chains. The increase in the benzenoid conformation leads to a general lower stacking of the polymer chains responsible for a worsening of the charge transport between these chains. [140][190] The histogram graph in Figure 38B shows the conductivity and % quinoid values both reported as a function of the vapors exposure time.

The monotonic decrease of conductivity and % quinoid confirms the strictly correlation between structural features of treated PEDOT chains and the electrical properties of the whole blend system.

Given the performance exhibited by the PEGDA:PEDOT composite, a possible use as a cumulative measuring device for short-term or single-shot measurements is proposed.[191][192]

In this view, in Table 3 a state-of-the-art review of the most significant results collected for 3D-printed cumulative adsorption materials is shown to highlight the novelty of our achievements.

Printing Technique	Filler	Matrix or Solvent	$\Delta R/R$	Active Area (mm^2)	Ref.
Ink-jet	MWCNT + PEDOT:PSS	dH ₂ O	0.02	1	[186]
Ink-jet	PEDOT:PSS	dH ₂ O	0.03	40	[193]
Ink-jet	Graphene+PEDOT:PSS	dH ₂ O	0.008	3.75	[194]
Ink-jet	CB	TPU	0.2	400	[195]
Ink-jet	rGO	dH ₂ O	0.3	400	[29]
FDM	MWCNT	PVC	3	8.13	[196]
FDM	MWCNT	PVDF	1.3	5.5	[197]
SL	CNFs	Epoxy Resin	0.23	485	[198]
SL	treated PEDOT:PSS	PEGDA	1	540	This work

Table 3: State-of-the-art of 3D-printed cumulative adsorption materials for acetone and ethanol vapor. TPU: thermoplastic polyurethane polymer; PC: polycarbonate; PEDOT:PSS: poly(3,4-ethylenedioxythiophene) polystyrene sulfonate; PVDF: poly(vinylidene fluoride); MWCNT: multi-walled carbon nanotubes; rGO: graphene oxide; CNFs: carbon nanofibers; FDM: fused deposition modeling; SL: stereolithography.

As can be observed from Table 3, a wide variety of materials have been printed by ink-jet technology, whereas MWCNT and PEDOT:PSS-based composite materials have been essentially tested in fused deposition modeling and stereolithography printing production methods. Moreover, it is worth pointing out that the SL approach allows for printing high-surface area, complex architectures with a greater resolution compared to the ink-jet and FDM printing techniques.

As shown in Table 3, the normalized resistance variation of the double helix structure is consistent with the values reported in other works. In particular, among the materials containing PEDOT:PSS filler, the printed PEGDA:PEDOT double helix structure exhibits the highest active area value and an $\Delta R/R$ ratio satisfactory for cumulative adsorption applications.

From this perspective, the coupling of the material and the printing technique adopted in the present work permits one to produce 3D structures with large and complex surface areas, that can be suitably exploited for the assembling of cumulative gas adsorption devices.

Chapter 5

Organic Electrochemical Transistors based on PEGDA 575 and treated PEDOT:PSS

5.1 Introduction

3D Stereolithography (SL), has delivered a new conceptualization of object design and fabrication with more advantages for Organic Electronics field.[199][200]

The possibility to produce three-dimensional devices can offer new solutions and capabilities integration, providing enhancements in many fields of application: energy storage[201], sensors for wearable electronics[202] and biomedical devices for healthcare.[203]

One of the emerging applications based on 3D devices are the Organic Electro-Chemical Transistors (OECTs) that show multifunctional operation in so far as they allow implementing both a transistors-like and a memristive-like response.[204] Actually the largest part of 3D printing methods employed to develop electronic devices offer only 2D structures (e.g. ink-jet[205], aerosol-jet[206]) or 3D device implemented upon multistep processes[207] and by Fused Deposition Modeling (FDM) and micro-dispensing.[208]

On this basis, the present chapter demonstrates that is possible to produce a PEGDA 575 and treated PEDOT:PSS 3D OECT. Furthermore, it was established to be efficient in biosensing applications.

5.2 3D OECT Fabrication

The 3D printing of the OECT with the conductive resin started from a simple geometry to assess the material properties and its suitability for printing a biosensing element. For these reasons, 2 mm long straight channel was designed with 500 μm thickness. At the opposite extremities of the channel two squared contact pads were printed using the same resin.

Initially, with the purpose to miniaturized 3D printed sensors, the 3D OECT was designed to have the smallest channel width reachable.

Therefore, considering the printer lateral resolution (around 80 μm) and the size of treated PEDOT:PSS particles inside PEGDA 575 resin, the smallest channel width was set to be 300 μm , in order to guarantee both accuracy and mechanical stability.

Furthermore, different channel widths were investigated and for this reason a wider channel was also printed (700 μm wide, 2 mm long) to analyze the transistor behavior. An insulating layer was then added to guarantee always the same channel length (2 mm) to be involved in the doping/de-doping process; using this part was also possible ensuring the OECTs response repeatability. On the insulating layer two wells were built to contain an electrolyte volume (~ 175 μL). The 3D printed OECT is reported in Figure 39. The commercial SpotHT resin was used to print the insulating parts while the conductive elements were printed with the Poly(ethylene glycol) diacrylate 575 with treated ClevisTM PH1000 resin. The SpotHT (Spot-A Materials, Barcelona, Spain) is a mixture of PI, aliphatic and urethane acrylates. The viscosity of this commercial resin is 350 mPa·s. The insulating base, the insulating support and the transistor part were 500 μm thick, while the wells barriers were 8 mm high.

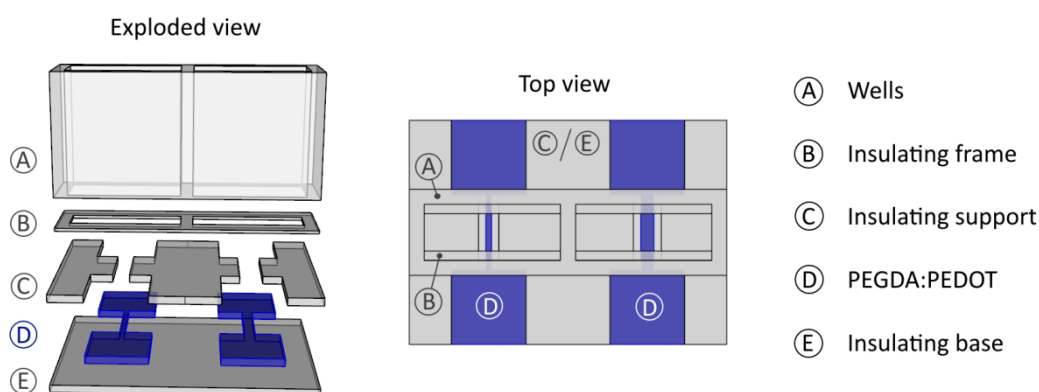


Figure 39: Computer-Aided Design drawing of the OECT to be printed.

The device was post-cured with a thermal treatment to post-process the 3D printed part, as previously reported.[209] This thermal process can induce an annealing of PEDOT:PSS and then improve the 3D OECTs performance.[210]

Printing two different channel widths of 300 μm and 700 μm on the same device demonstrated the printability of the PEGDA 575 and treated PEDOT:PSS resin (Figure 40A).

After the electrical measurement, one of the critical constraint was noticed, actually not related to the SL intrinsic constraint, but rather to the reproducibility of the device response. Indeed, analyzing the 3D printed devices it was observed that the small channel (300 μm) has not a reproducible response like the one with the 700 μm wide channel (Figure 40Figure 39B). Hence, the large channel design was selected as the best performing one in terms of reproducibility. Maybe the amount of active material in the large channel is enough to provide stable electrical signal. However, the increasing of the treated PEDOT:PSS ratio in the resin slightly reduces the printability. Later, to get reproducible and well performing devices the best compromise was achieved using the Poly(ethylene glycol) diacrylate 575 and the 45% wt. of treated PEDOT:PSS and printing a geometry with 700 μm wide channel.

A section of the OECT channel (Figure 40C,D) was observed by Field Emission Scanning Electron Microscopy (FESEM) to check that the insulating SpotHT resin did not accidentally cover the active PEGDA:PEDOT resin, thus passivating it. Indeed, a clear separation between the two resins was observed, as reported in Figure 40D. Finally, through the FESEM imaging is possible observing small flakes (of the order of a few microns) inside the OECT channel, that can be attributed to the treated PEDOT:PSS particles (Figure 40E).

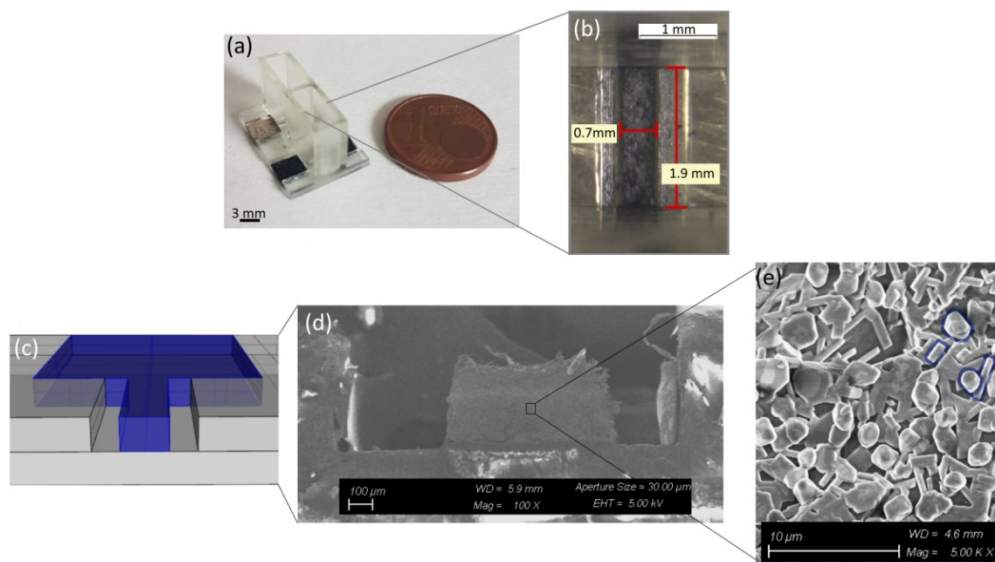


Figure 40: 3D printed OECT. (A) Device after printing; (B) microscope image of the channel (700 μm wide); (C) section view of the 700 μm wide channel design; (D) SEM image of the same section view reported in (C); (E) SEM image of the PEGDA:PEDOT resin polymerized.

5.3 Results

The performances of the composite blend used in OECTs architectures was analyzed in collaboration with the Institute of Materials for Electronics and Magnetism (IMEM-CNR, Parco Area delle Scienze 37/A, 43124 Parma, Italy). This analysis is a noticeable example of 3D OECTs suitability in biological sensing applications. For this purpose, the 3D OECTs efficiency in detecting biomolecules of interest in medicine was tested.

In particular, the detection, by the 3D OECT, of the dopamine (DA) (MW = 189.54 mg/mol, Alfa Aesar) was implemented. Dopamine is a neurotransmitter regulating the correct functioning of several organs and whose loss in some areas of the brain causes, for example, the Parkinson's disease. The dopamine was chosen as a target also because it is an important molecule for biosensing field.[211]–[214]

The calibration curve for DA detection realized using a 3D OECT and calculated from transfer curves is described in Figure 41. Different concentrations of DA ($[DA] = 0, 10 \mu\text{M}, 100 \mu\text{M}, 1 \text{mM}$ and 5mM in PBS 100 mM) were tested and transfer curves from the lower to higher concentrations are reported as an example in Figure 41.

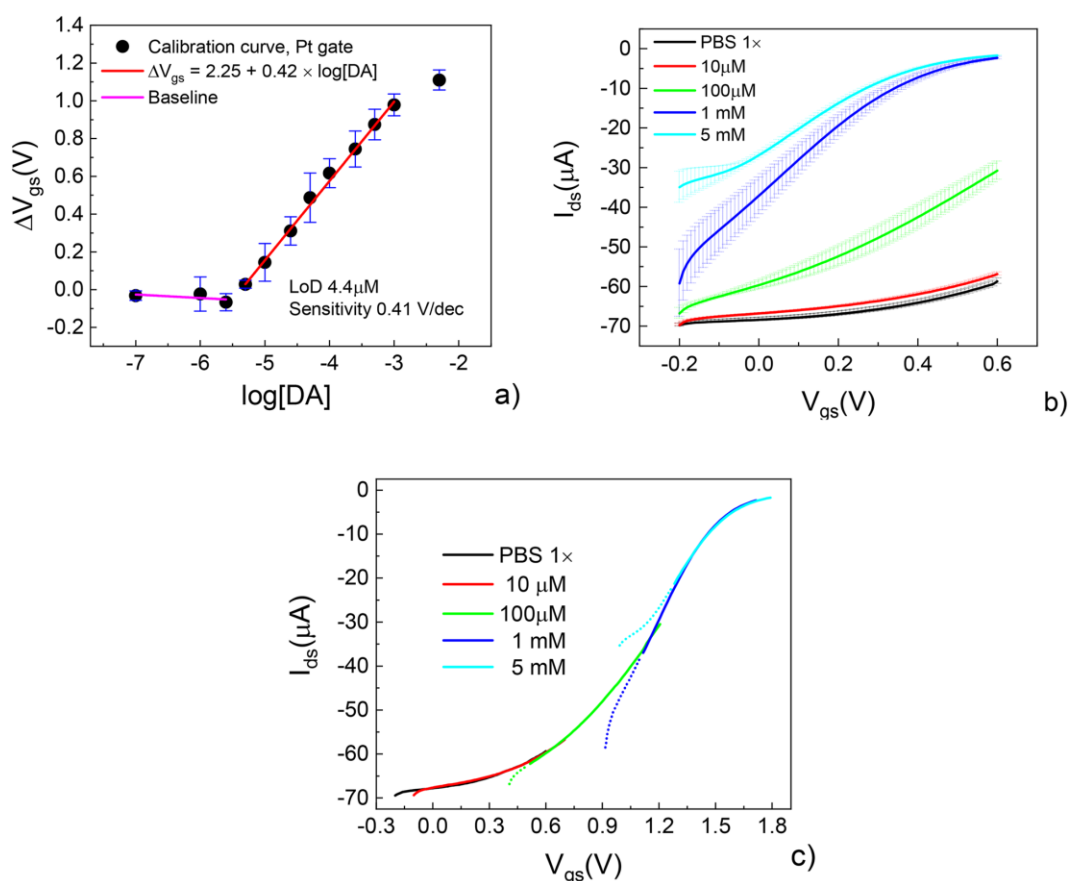


Figure 41: (a) Calibration curve for dopamine sensing by a Poly(ethylene glycol) diacrylate 575 and treated PEDOT:PSS using a 3D Organic Electro-Chemical Transistors; (b) typical transfer curves measured at different dopamine concentrations ($[DA] = 0, 10 \mu\text{M}, 100 \mu\text{M}, 1 \text{mM}$ and 5mM , error bars are standard deviations) and (c) universal curve obtained by merging transfer curves in (b) upon shifting them along the V_{gs} axis.

The large error bars upon averaging repeated measurements can be due to a quasi-reversibility of electrochemical processes in the conductive blend, especially at lower V_{gs} (the baseline current, I_{ds} for $V_{gs} \rightarrow 0$, shifts towards lower values and the largest shift is systematically recorded after the first measurement).

In this experiment the reactivity of catecholamines with a bare Pt electrode was measured, whereas dopamine is expected to be involved in a 2-electrons exchange mechanism with the platinum electrode.[215] The measurement protocol is the same reported in literature.[216] The proposed protocol relies on the fact that the reaction of dopamine at the platinum gate electrode is able to modulate the effective gate voltage ($V_{gs,eff}$) due to an offset voltage (V_{offset}) strictly connected to the analyte concentration. Equation 9 describes this phenomenon [217]:

$$\text{Eq. 9 } V_{offset} = V_{gs,eff} - V_{gs} = \Delta V_{gs} = 2.30 (1 + \gamma) \frac{K_B T}{nq} \log[DA] + \text{cost}$$

where [DA] is the dopamine concentration T is temperature, n is the number of electrons transferred at the gate, K_B is the Boltzmann's constant and γ is the ratio between the capacitances at the gate electrode/electrolyte and electrolyte/active channel interfaces. This equation predicts that a rise of dopamine concentration causes the improvement of V_{offset} that, in turn, suggests a reduction of the channel current.

The device performance can be represented by extracting two factors from the calibration curve, i.e. the Limit of Detection (LoD) and the sensitivity. The first represent the lowest concentration of the analyte that can be reliably detected with this 3D printed sensor. The sensitivity, indeed, describes the smallest analyte concentration able to create a measurable output signal for the sensor. The 3D OECT shows a good sensitivity of 0.41 V/dec. The assessment of ΔV_{gs} by evaluating the shift of transfer curves is predictable to be less effective in determining minor LoDs if compared to its estimation based on real-time measurements, such as the recording of the step-like OECT response upon subsequent additions of the analyte to be detected in an electrolytic reservoir. [218], [219] However, both devices demonstrate a LoD around the micromolar range with a dynamic window varying between the micromolar and the millimolar range of [DA]. The LoDs value obtained with this 3D OECT are in line with the standard unmodified Pt gate electrodes.[213], [216]

Chapter 6

3D Printed energy storage device based on PEGDA and treated PEDOT:PSS blend

6.1 Introduction

Today, the new generation of energy storage systems has stringent requirements in terms of portability, compactness, integration and yield. The common fabrication techniques for energy storage systems are based on complex and multiple processing steps that could limit their possible easy integration in portable devices like smartphones, laptops and so on. 3D-printing technologies can open a new approach to fabrication processing, also because of the large plethora of available material and the possibility to tune their electrical[220], chemical[221], and morphological[222] properties. Furthermore, the 3D electrode provides a large active area giving short diffusion pathways and high conductivity during the ion transport mechanism compared to a standard 2D energy storage device.[223]

Although in the energy storage field there are more examples of 3D supercapacitor, based on filament deposition[224][225], laser sintering[226] or inkjet printing[227][228], there are actually few SL devices that combine different fillers to enhance the charge transfer of the resin. Furthermore, those devices show a low aspect ratio because of the high brittleness of the composite polymer. The main fillers for SL resins used for printing supercapacitors are silver nanowires (AgNW)[229] and multiwall carbon nanotubes (MWCNT)[32][230] or a combination of these materials with other metals or organic polymers, decorating for example the Ag nanoparticles with $\text{Pb}(\text{Zr},\text{Ti})\text{O}_3$.[33]

In this chapter, the possibility of printing 3D micro-supercapacitor (3D-MS) with a SL printer using the PEGDA 250 and treated PEDOT:PSS

conductive resin will be demonstrated. The 3D interdigitated design and production of the electrode arrays were obtained with a spatial micrometric resolution and optimized to improve the electrochemical performances for a 3D-printed micro-supercapacitor. The 3D-MS-C exhibits a promising energy storage and power density, thanks to the exploitation of a tailorable complex 3D design to increase the electrode's active surface.

6.2 3D Print device

The conductive blend based on treated PEDOT:PSS was studied as new printing material for electric double-layer capacitors. Initially, the blend was characterized to determine its electrochemical performance and later a complex 3D-MS-C was fabricated.

The PEGDA 250 with 1% wt. PI was chosen as matrix providing a low swelling effect and the amount of treated PEDOT:PSS was 35% wt.

Different electrode thicknesses were investigated in order to value the influence on the energy density per surface area unit. For this reason, the blend was characterized, using a disk geometry, with different thicknesses: 1.5, 1 and 0.7 mm.

These conductive disks (diameter 1 cm) were printed with a SL machine (Chapter 3.1) using an internal scan velocity of 1800 mm/s and contour scan velocity of 2000 mm/s; the power applied during the printing process for the samples A, B, and C was 50 mW (Figure 42).

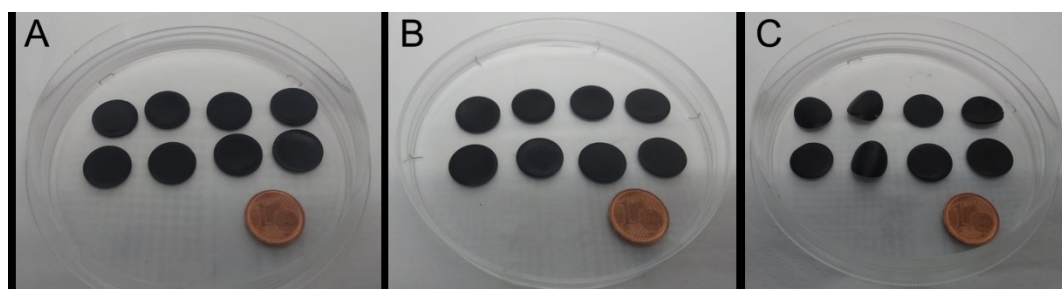


Figure 42: 3D printed disks of PEGDA 250 with 1% wt. PI and 35% wt. of treated PEDOT:PSS with thickness A) 1.5 mm B) 1 mm C) 0.7 mm.

The conductive samples were pressed into a metal disk of 16 mm-diameter and 2 mm thickness under a pressure of 400 MPa (Figure 43A). Conductivity measurement of the disk was performed with two probe connected to a multimeter (BioLogic Potentiostat, Seyssinet-Pariset, France) (Figure 43B).

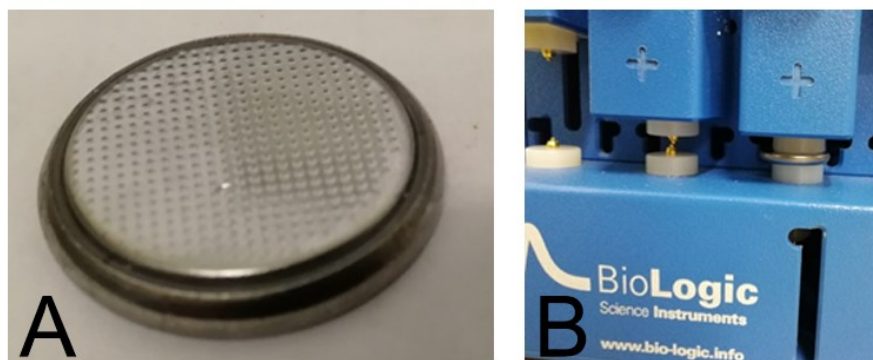


Figure 43: A) coin cell B) BioLogic with 2 points connection provides the lowest connection impedance.

Furthermore, a concept 3D-MSM was designed and printed using the conductive blend. The conductive blend based on treated PEDOT:PSS was also used as a glue layer to fix the 3D-MSM on the metal electrodes. The 3D-MSM was fabricated following the steps in Figure 44.

The fabrication procedure displayed in Figure 44 includes the following steps: (A) a platinum interdigitate electrodes (Pt-IDE) was sputtered on alumina substrate using a hard mask; (B) the 3D-IDE based on PEGDA 250 and 35% wt. of treated PEDOT:PSS was printed with 2000 mm/s and 50 mW; (C) using a spincoater (1000 rpm for 60 s), we obtained a thin layer of PEGDA 250 and treated PEDOT:PSS on a glass slice. Then the 3D-IDE was gently pressed on the glass slice to cover the bottom side with conductive blend. Afterwards, the 3D-IDE and the Pt-IDE were aligned using a microscope and cured under UV light for 5 minutes. Finally, a PDMS chamber was produced to confine the electrolyte gel.

The alignment between the two electrodes was guaranteed by the printer accuracy and the 3D-MSM was assembled at the end of the printing process.

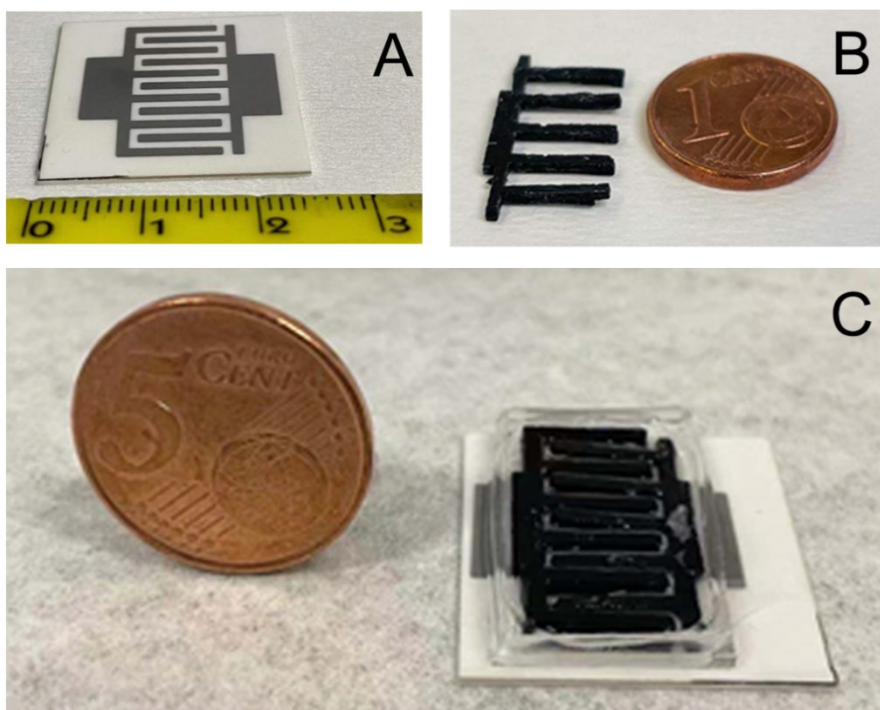


Figure 44: fabrication steps of 3D-IDE: A) Pt-IDE sputtered on alumina. B) 3D-IDE printed with PEGDA 250 and treated PEDOT:PSS. C) 3D-MSD device.

The KCl and the PVA was purchased from Millipore Sigma (Burlington, MA, USA). The molecular weight and the purity for KCl and PVA was 31-50 kDa and 99% respectively. The KCl/PVA hydrogel electrolyte is prepared: Polyvinyl alcohol (PVA) (1.0 g) was dissolved in 10 mL dH₂O with constant mixing at 85 °C for 2 h to form a homogeneous and clear liquid. Then, 10 mL of dH₂O containing KCl (0.1 M) was added to the above solution under continuous mixing until the formation of a gel-like solution. All the experiments reported below were performed using KCl and PVA electrolyte hydrogel.

Figure 45 shows a photograph of one finished MSD device fabricated on the alumina and tested using KCl/PVA as the solid-state gel electrolyte.

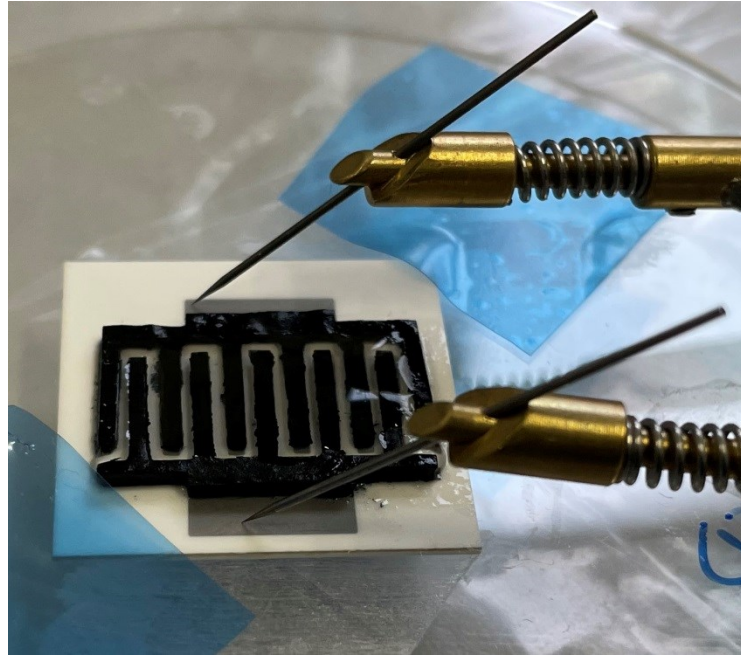


Figure 45: 3D-MSC device based on PEGDA 250 and 35% wt. of treated PEDOT:PSS.

6.3 Results

The electrodes' thickness can be well controlled using the 3D printing technology, because it is possible to increase the final device size layer by layer. The 3D electrodes have a different electrochemical behaviour in comparison to the in-plane, due to the fast ion diffusion through the thick electrode. Furthermore, with 3D electrodes it is possible to increase the surface energy storage capability in a small footprint area.

CV tests were performed to define the capacitance of the printed PEGDA 250 and treated PEDOT:PSS electrodes. All cyclic voltammetry (CV) curves were recorded with an applied potential from 0 to 0.8 V. Then, it is possible to calculate the capacitance using equation 10:

$$\text{Eq. 10} \quad C = \frac{Q_{total}/2}{\Delta V}$$

Where, Q_{total} is the supercapacitor charge, ΔV is the voltage range and C is the capacitance.

The specific capacitance of the 3D-MSC depends on the specific surface area of treated PEDOT:PSS electrodes in contact with the electrolyte. Then the area specific capacitance (C_a) of the supercapacitor can be calculated from the CV curves using equation 11:

$$\text{Eq. 11} \quad C_a = \frac{1}{2 A \left(\frac{\Delta V}{\Delta t}\right) (V_f - V_i)} \int_{V_i}^{V_f} I V dV$$

Where, A is the area of the electrodes, V_f and V_i are the potential limits of the CV curve, $\Delta V/\Delta t$ is the voltage scan rate, and $\int I V dV$ is the area of the CV curve.

From this perspective, three disks with different thickness were studied, characterising their electrochemical performance. In Figure 46A the average current density was 7.5, 10, 15 $\mu\text{A}/\text{cm}^2$ for 700, 1000 and 1500 μm respectively, while the areal capacitance was 15, 20, 30 $\mu\text{F}/\text{cm}^2$ for 700, 1000 and 1500 μm respectively (Figure 46B). Observing the electrochemical trend, it is clear that increasing the electrode thickness makes it possible improving devices performance, achieving a high current density and areal capacitance. Rather Faradaic capacitance can be obtained by the diffusion of electrolyte inside the 3D disk at lower scan rates that aids in the enhancement of charge storage capability.[177]

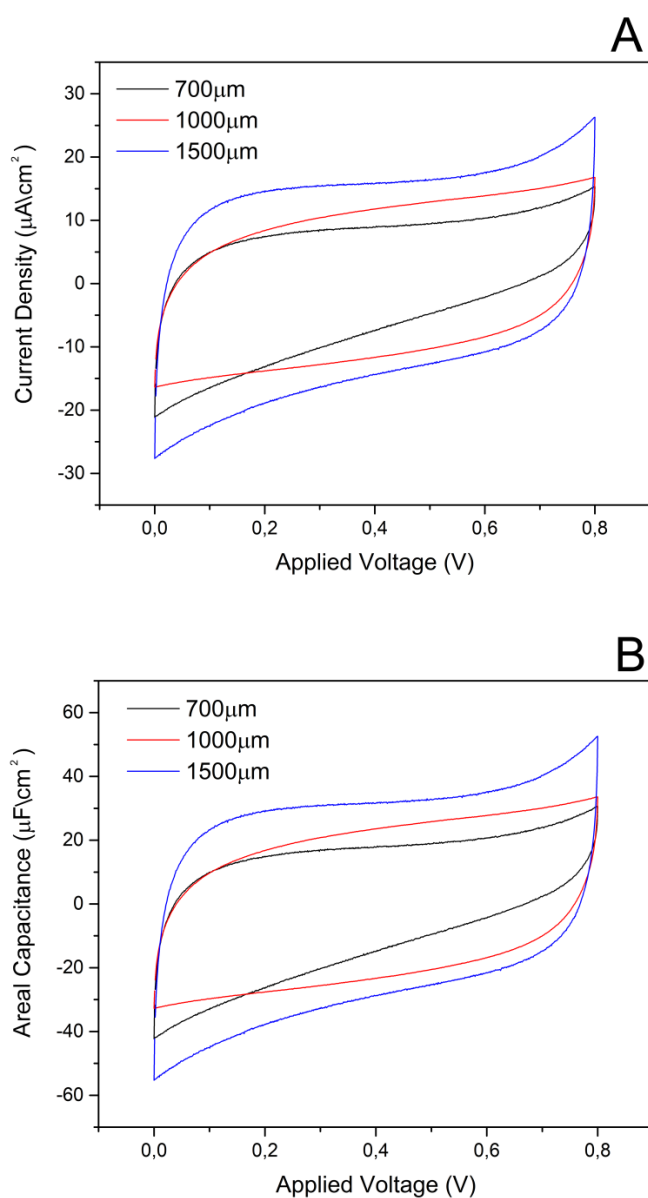


Figure 46: Cyclic voltammograms collected in 0.1 M H_2SO_4 as a function of scan rate 10 mV/s; A) current density B) areal capacitance.

Moreover, for the 3D-MSC the capacitance and the areal capacitance were studied. Figure 47 shows the typical charge-discharge profile of capacitors with a capacitance of 6.31, 3.38, 1.53 and 0.81 mF at scan rates of 10, 20, 50, and 100 mV/s, respectively.

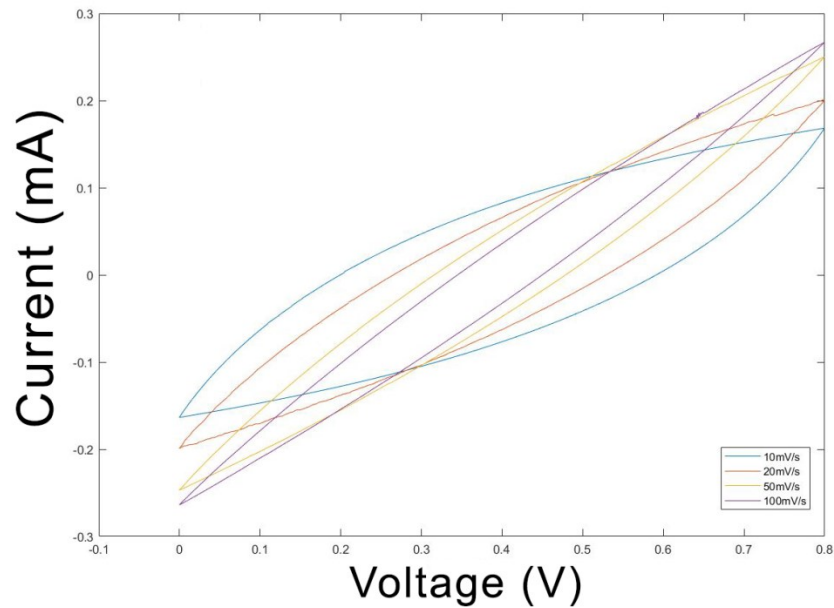


Figure 47: CV curves of printed 3D-MSC measured at different scan rates of 10, 20, 50, 100 mV/s.

The C_a calculated from the CV curves were 2.16, 1.16, 0.52 and 0.28 mF/cm^2 at scan rates of 10, 20, 50, and 100 mV/s, respectively.

Figure 48 displays the galvanostatic charge-discharge (GCD) curves that show a pseudosymmetric response characteristic at different current densities of 0.5, 1, 1.5 and 2 mA/cm^2 , indicating an ideal capacitive behaviour.

It can be seen in Figure 48 that a small internal resistance of the 3D-MSC (IR drop) is present at the beginning of each discharge curves. This IR drop causes the decreasing of capacitance at high discharge rates in the CV investigation.

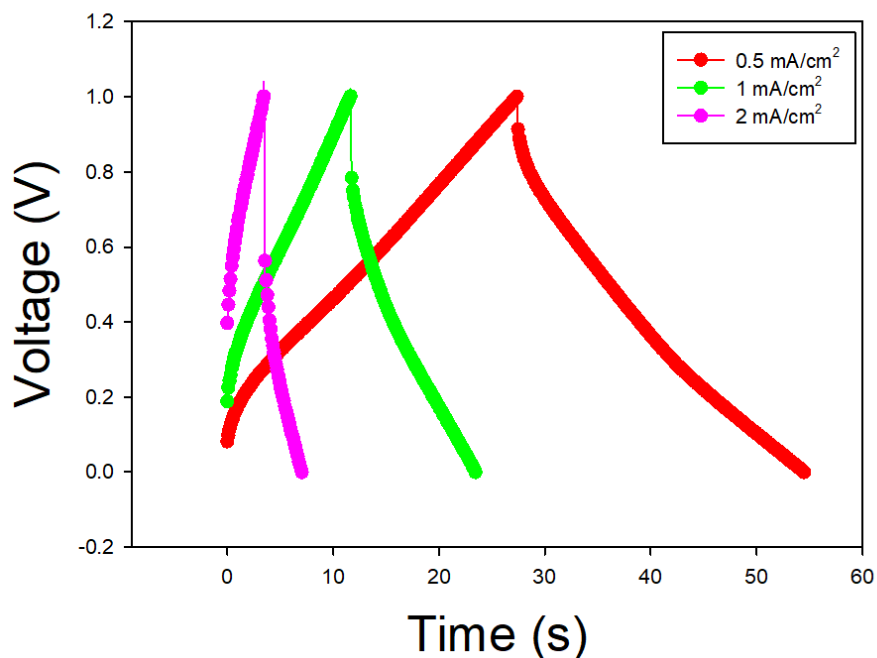


Figure 48: GCD curves of 3D-MSC based on PEGDA 250 and treated PEDOT:PSS at current densities of 0.5, 1 and 2 mA/cm².

The capacitance of 3D-MSC is 200 mF/g (2.16 mF/cm²) and it is consistent with the values reported in the literature.[231] This can be explained by the high specific surface area of 3D-MSC and its design.

Approximately linear charge/discharge curves were acquired as an indicative of good capacitor. Nevertheless, there was high IR drop at the beginning of discharge curve ascribed to the internal resistance i.e. contact resistivity, interfacial resistance from metal to blend and the electrolyte ionic resistance that cannot be negligible.

These results demonstrate that the SL printing technology proposed here permits the current density and areal capacitance of the resultant power device to be simply controlled by modifying the print geometry.

Chapter 7

Conclusions

This work reports on the preparation and application of a new conductive resin for stereolithographic 3D printing based on treated PEDOT:PSS (Clevios™ PH 1000).

With this novel resin formulation, it is possible producing complex 3D-shaped conductive devices by StereoLithography. The preparation steps were adjusted (chapter 3) to achieve a stable and hard resin for SL systems, where the prominent conductivity response of 0.05 S/cm was obtained by a combination of the matrix(PEGDA)/filler(treated PEDOT:PSS) ratio. This composite blend not only keeps relatively good mechanical properties, but also noteworthy electrical conductivity, light weight and good surface wetting properties, thus resulting in a right resin blend fully exploitable and integrable in miniaturized systems like microsensors and microfluidics devices.

The composite blend with PEGDA 575 as the host matrix and PEDOT:PSS as the filler for 3D systems was studied as VOCs adsorbent material (chapter 4). The control of the conductive features of PEDOT:PSS, through suitable chemical treatments, and the identification of its appropriate loading in the host matrix allowed for producing a homogeneous and easily printable resin for the manufacturing of conductive 3D objects with complex and reproducible geometries. These systems have proven to be able to work with chemical vapors in the long term by giving a reliable and noticeable variation of their structural and conductive behaviour. The overall collected results demonstrate that the materials and the manufacturing protocol reported here constitute a proof of principle of the possibility of developing an innovative manufacturing technology for long-term monitoring.

The conductive blend based on treated PEDOT:PSS was demonstrated to maintain performance similar to that of PEDOT:PSS in terms of electrical conductance, bulk ionic diffusion mechanism, gating response in OECTs architectures and, hence, presenting quite good sensing response (chapter 5). 3D OECTs showed an higher sensitivity of 0.41 V/dec toward dopamine detection.

With the 3D OECT we have demonstrated the possibility to use it as biosensors and, hence, in a perspective view, the freeform manufacture enabled by 3D printing paves the way for their incorporation in IoT and smart devices.

Much of the current literature on supercapacitor pays particular attention to the enhancement of the electrochemical performances of material and device using 3D fabrication techniques, which grants several gains in terms of performance, cost and scalability. The 3D devices allow an increase of either the volume of active filler loaded and the active surface area. The 3D supercapacitor provides a fast ion transport through structures with a high specific energy and power densities.

A 3D and stable electrical double layer capacitor, which can be manufactured by SL, has been developed in this study, The overall thickness of the devices can be minimized and their electrochemical behavior was studied (chapter 6). The cycle voltammetry tests exhibit that the 3D-MSCs deliver a specific capacitance of 2.16 mF/cm^2 , suggesting that this resin is a promising candidate for energy storage applications.

This work has successfully characterized and optimized a novel conductive blend based on PEGDA and treated PEDOT:PSS for 3D printing. Of course, the resin alone represents only the first milestone for device development. In fact, its physical properties should be exactly studied and the processing protocols should be engineered obtaining a substantial throughput. The passage from the material production to a practical exploitation often needs some decades. However, this work has successfully demonstrated the potential of this blend as a cumulative measuring device, biochemical sensor and supercapacitor.

Ringraziamenti

In questi anni di dottorato sono venuto a contatto con diverse persone e gruppi di lavoro che mi hanno insegnato molto, sia dal punto di vista scientifico che umano, ed è per questo che vorrei ringraziarli.

In primis, vorrei ringraziare la mia famiglia. Mia nonna, mia madre e mio padre che, con i loro sacrifici, mi hanno dato la possibilità di procedere con gli studi e vivere le mie esperienze lontano dalla mia isola; grazie all'incoraggiamento e conforto di mio fratello con la sua fidanzata (Sebas e Silvia) e delle mie sorelle (Gavinca, Giusi e Miram) sono riuscito ad andare avanti durante il mio percorso in questi anni. Ringrazio anche il ramo della mia famiglia calabrese, in particolar modo mia cugina Cettina, che per me è stata (e continua ad esserlo nella mia memoria) un esempio da seguire.

In seconda battuta è doveroso per me ringraziare due donne stupende che da più di 10 anni mi sono state sempre vicino e con le quali, nonostante le difficoltà e le sfighe cosmiche, sono sempre rimasto unito, senza Miriam e Francesca non sarei stato in grado di sopportare alcune situazioni di questi anni e vivere, allo stesso tempo, momenti ed esperienze uniche.

Un altro ruolo importante è stato svolto in questi anni da quelle persone che non sono effettivamente della mia famiglia ma a cui tengo particolarmente. Ringrazio i miei amici storici: Giorgio, Iolanda, Dody, Frank e Anto, Silvia, Valeria, Marco e Pierpaolo, perché in diversi modi e sotto diversi aspetti hanno sempre trovato la parola giusta al momento giusto. Una particolare menzione merita Swapnil, che ringrazio per tutte le esperienze che abbiamo condiviso nei viaggi in giro per l'Europa e per il grande affetto che ci lega.

Il presente lavoro di dottorato non sarebbe stato possibile senza l'aiuto e il contributo del gruppo Chilab (Valentina, Matteo P., Matteo S. Alberto, Eve, Federica, Giulia, Alessio, Lorenzo, Elena O, Laura Boschis, Simone e Marzia) e del Politecnico di Torino (Paola, Francesca, Andrea, Annalisa&Ignazio, Stefano, Angelica, Pietro, Mauro, Sergio e Luciano), li ringrazio tutti perché in questi anni hanno contribuito a rendere possibile questo progetto di dottorato e sono contento di aver condiviso con loro pubblicazioni, esperimenti, missioni, caffè di dubbia qualità alle macchinette e birre.

Un ringraziamento particolare va dato ai principali promotori del mio dottorato: il Prof. Pirri, il Prof. Cocuzza e la Dott.ssa Monica Barale, che ringrazio per l'aiuto e l'opportunità che mi hanno dato.

Ringrazio il gruppo di Microla per la lavorazione dei campioni e per la progettazione della stampante 3D SL utilizzata per poter sviluppare la resina conduttiva del presente lavoro di tesi.

Non potrò mai dimenticare le mie missioni "sensoriali" presso l'FBK con il gruppo del LaBSSAH (Cristina, Lorenzo e Cecilia). Sono stati per me come dei secondi tutor di dottorato e gli sono veramente grato per l'aiuto e le attività svolte insieme. Tra le problematiche da "dottorando disagiato", le scarpinate attorno alle

belle montagne di Trento, i chip microfluidici e i caffè al bar mi sono sempre sentito parte del gruppo e sento di aver appreso davvero molto grazie a loro.

Anche se non sono stato in grado di coinvolgerli in pieno, vorrei ringraziare il gruppo di Chimica analitica e di Scienza dei materiali di Roma Tor Vergata (Noemi, MariaRita, Rocco, la Prof.ssa Moscone, Giulia, Laura, Fabiana, Emanuela e la Prof.ssa Terranova). Prima di iniziare il dottorato e durante il mio percorso a Torino sono sempre rimasto in contatto con loro. Più di una volta mi sono mancati e più di una volta mi sono stati vicino, sia umanamente che scientificamente; grazie alle analisi eseguite e alle intuizioni di alcune di loro, il presente lavoro è stato migliorato e caratterizzato a 360 gradi.

Una menzione vorrei farla per un gruppo di cui ho particolarmente stima, quello del CNR-IFN di Luca Businaro, Annamaria Gerardino ed Adele de Ninno che, prima di questo dottorato, mi hanno insegnato quasi tutto quello che so nel campo della microfabbricazione.

L'attività di ricerca svolta a Eindhoven nel 2020 è stata interrotta a causa del Covid-19, tuttavia, anche se breve, ci tengo a ringraziare la Prof.ssa Luttge, Rahman e Gülден per la loro disponibilità e per le attività di laboratorio svolte sul progetto Connect; ringrazio anche la mia coinquilina Zhiyi con cui abbiamo affrontato il periodo del lockdown senza perderci d'animo.

La prima persona che ho conosciuto a Torino è stata Andrea e successivamente Francesco, Debora e Laura, con loro ho passato 4 anni a Torino stupendi perché mi hanno fatto sempre sentire come se fossi a casa, sempre pronti per una cena all'improvviso o per una birretta. Hanno sempre trovato il modo di farmi sorridere tra laseroni, frecce scoccate e treni per Silent Hill e per questo li ringrazio.

Infine ringrazio tutte quelle persone che in questi 4 anni mi hanno fatto scoprire Torino e le sue mille sfaccettature. Non pensavo che questa città mi sarebbe piaciuta così tanto e questo lo devo in gran parte al gruppo Golden (Giovanni, Jacopo, Nicola, Lorenzo, Antonio, Filippo, Andrea e Salvatore) con cui ogni venerdì o sabato riuscivamo a staccare il cervello e a divertirci come matti. Grazie a Giulia, Mathieu e Ilaria l'aperitivo del weekend diventava un rito propiziatorio per scacciare i demoni della settimana passata e affrontare con serenità quella successiva. Grazie all'aiuto del mio maestro di tiro con l'arco (Roberto e degli arcieri del CH₄ Sara, Salvatore e Viktor) ed del mio maestro di giardinaggio (Angelo) sono riuscito, a Torino, a trovare il giusto equilibrio tra le mille attività di dottorato e le cose che veramente contano. Ringrazio il mio carissimo amico Pino, con cui abbiamo condiviso gioie e tristezze dovute alla lontananza dalla famiglia; gli ultimissimi ringraziamenti vanno infine al gruppo di volontariato ed in particolare ad Angelo de Carlo e ai tesisti conosciuti durante il percorso di dottorato per il loro affetto e stima (Stefano, Francesca, Matteo e Silvia).

Per Aspera Ad Astra.

References

- [1] T. J. Horn and O. L. A. Harrysson, "Overview of current additive manufacturing technologies and selected applications," *Sci. Prog.*, vol. 95, no. 3, pp. 255–282, Sep. 2012.
- [2] F. Brocal, M. A. Sebastián, and C. González, "Advanced manufacturing processes and technologies," in *Management of Emerging Public Health Issues and Risks: Multidisciplinary Approaches to the Changing Environment*, Elsevier, 2018, pp. 31–64.
- [3] K. S. Prakash, T. Nancharaih, and V. V. S. Rao, "Additive Manufacturing Techniques in Manufacturing -An Overview," in *Materials Today: Proceedings*, 2018, vol. 5, no. 2, pp. 3873–3882.
- [4] T. D. Ngo, A. Kashani, G. Imbalzano, K. T. Q. Nguyen, and D. Hui, "Additive manufacturing (3D printing): A review of materials, methods, applications and challenges," *Composites Part B: Engineering*, vol. 143. Elsevier Ltd, pp. 172–196, 15-Jun-2018.
- [5] L. Yang *et al.*, "Introduction to Additive Manufacturing," Springer, Cham, 2017, pp. 1–31.
- [6] C. K. Chua and K. F. Leong, *3D Printing and additive manufacturing: Principles and applications (with companion media pack) - fourth edition of rapid prototyping*. World Scientific Publishing Co., 2014.
- [7] S. H. Huang, P. Liu, A. Mokasdar, and L. Hou, "Additive manufacturing and its societal impact: A literature review," *International Journal of Advanced Manufacturing Technology*, vol. 67, no. 5–8. Springer, pp. 1191–1203, 16-Jul-2013.
- [8] S. A. M. Tofail, E. P. Koumoulos, A. Bandyopadhyay, S. Bose, L. O'Donoghue, and C. Charitidis, "Additive manufacturing: scientific and technological challenges, market uptake and opportunities," *Materials Today*, vol. 21, no. 1. Elsevier B.V., pp. 22–37, 01-Jan-2018.
- [9] T. Wohlers and T. Gornet, "History of Additive Manufacturing," 2016.
- [10] Y. L. Yap, S. L. Sing, and W. Y. Yeong, "A review of 3D printing processes and materials for soft robotics," *Rapid Prototyping Journal*, vol. 26, no. 8. Emerald Group Publishing Ltd., pp. 1345–1361, 20-Jun-2020.
- [11] M. K. Mohan, A. V. Rahul, G. De Schutter, and K. Van Tittelboom, "Extrusion-based concrete 3D printing from a material perspective: A state-of-the-art review," *Cem. Concr. Compos.*, vol. 115, p. 103855, Jan. 2021.
- [12] J. Y. Lee, J. An, and C. K. Chua, "Fundamentals and applications of 3D printing for novel materials," *Applied Materials Today*, vol. 7. Elsevier Ltd, pp. 120–133, 01-Jun-2017.
- [13] R. Duballet, O. Baverel, and J. Dirrenberger, "Classification of building systems for concrete 3D printing," *Autom. Constr.*, vol. 83, pp. 247–258, Nov. 2017.
- [14] J. P. Moore and C. B. Williams, "Fatigue properties of parts printed by PolyJet material jetting," *Rapid Prototyp. J.*, vol. 21, no. 6, pp. 675–685, Oct. 2015.
- [15] H. Miyanaji, S. Zhang, A. Lassell, A. Zandinejad, and L. Yang, "Process Development of Porcelain Ceramic Material with Binder Jetting Process for Dental Applications," *JOM*, vol. 68, no. 3, pp. 831–841, Mar. 2016.
- [16] F. Liravi, M. Salarian, C. Dal Castel, L. Simon, and E. Toyserkani, "High-speed material jetting additive manufacturing of silicone structures: mechanical characterization," *Prog. Addit. Manuf.*, vol. 4, no. 4, pp. 479–495, Dec. 2019.

- [17] A. A. Martin *et al.*, “Dynamics of pore formation during laser powder bed fusion additive manufacturing,” *Nat. Commun.*, vol. 10, no. 1, pp. 1–10, Dec. 2019.
- [18] S. L. Sing, J. An, W. Y. Yeong, and F. E. Wiria, “Laser and electron-beam powder-bed additive manufacturing of metallic implants: A review on processes, materials and designs,” *Journal of Orthopaedic Research*, vol. 34, no. 3. John Wiley and Sons Inc., pp. 369–385, 01-Mar-2016.
- [19] M. Revilla-León, L. Ceballos, I. Martínez-Klemm, and M. Özcan, “Discrepancy of complete-arch titanium frameworks manufactured using selective laser melting and electron beam melting additive manufacturing technologies,” *J. Prosthet. Dent.*, vol. 120, no. 6, pp. 942–947, Dec. 2018.
- [20] M. A. Melia, H. D. A. Nguyen, J. M. Rodelas, and E. J. Schindelholz, “Corrosion properties of 304L stainless steel made by directed energy deposition additive manufacturing,” *Corros. Sci.*, vol. 152, pp. 20–30, May 2019.
- [21] S. Tabacu and C. Ducu, “Experimental testing and numerical analysis of FDM multi-cell inserts and hybrid structures,” *Thin-Walled Struct.*, vol. 129, pp. 197–212, Aug. 2018.
- [22] D. Popescu, A. Zapciu, C. Amza, F. Baci, and R. Marinescu, “FDM process parameters influence over the mechanical properties of polymer specimens: A review,” *Polym. Test.*, vol. 69, pp. 157–166, Aug. 2018.
- [23] J. Borrello, P. Nasser, J. C. Iatridis, and K. D. Costa, “3D printing a mechanically-tunable acrylate resin on a commercial DLP-SLA printer,” *Addit. Manuf.*, vol. 23, pp. 374–380, Oct. 2018.
- [24] R. Bannerman, A. Theiss, and D. Grzybowski, “MAKER: Utilizing 3-D Printing of Nanotechnology Design Project Prototypes to Enhance Undergraduate Learning,” in *2016 ASEE Annual Conference & Exposition Proceedings*, 2016, vol. 2016-June.
- [25] P. Tseng, C. Murray, D. Kim, and D. Di Carlo, “Research highlights: Printing the future of microfabrication,” *Lab Chip*, vol. 14, no. 9, pp. 1491–1495, May 2014.
- [26] T. A. Campbell and O. S. Ivanova, “3D printing of multifunctional nanocomposites,” *Nano Today*, vol. 8, no. 2, pp. 119–120, Apr. 2013.
- [27] S. J. Leigh, R. J. Bradley, C. P. Pursell, D. R. Billson, and D. A. Hutchins, “A Simple, Low-Cost Conductive Composite Material for 3D Printing of Electronic Sensors,” *PLoS One*, vol. 7, no. 11, p. 49365, 2012.
- [28] J. T. Muth *et al.*, “Embedded 3D Printing of Strain Sensors within Highly Stretchable Elastomers,” *Adv. Mater.*, vol. 26, no. 36, pp. 6307–6312, Sep. 2014.
- [29] F. Yavari and N. Koratkar, “Graphene-based chemical sensors,” *Journal of Physical Chemistry Letters*, vol. 3, no. 13. American Chemical Society, pp. 1746–1753, 05-Jul-2012.
- [30] S. Agarwala *et al.*, “Wearable Bandage-Based Strain Sensor for Home Healthcare: Combining 3D Aerosol Jet Printing and Laser Sintering,” *ACS Sensors*, vol. 4, no. 1, pp. 218–226, Jan. 2019.
- [31] C. L. Manzanares Palenzuela and M. Pumera, “(Bio)Analytical chemistry enabled by 3D printing: Sensors and biosensors,” *TrAC - Trends in Analytical Chemistry*, vol. 103. Elsevier B.V., pp. 110–118, 01-Jun-2018.
- [32] M. Areir, Y. Xu, R. Zhang, D. Harrison, J. Fyson, and E. Pei, “A study of 3D printed active carbon electrode for the manufacture of electric double-layer capacitors,” *J. Manuf. Process.*, vol. 25, pp. 351–356, Jan. 2017.
- [33] Y. Yang *et al.*, “Three dimensional printing of high dielectric capacitor using projection based stereolithography method,” *Nano Energy*, vol. 22, pp. 414–421, Apr. 2016.
- [34] A. Tanwilaisiri, Y. Xu, D. Harrison, J. Fyson, and M. Arier, “A Study of Metal Free Supercapacitors Using 3D Printing,” *Int. J. Precis. Eng. Manuf.*, vol. 19, no. 7, pp. 1071–1079, Jul. 2018.
- [35] P. K. Yuen, “Embedding objects during 3D printing to add new functionalities,” *Biomicrofluidics*, vol. 10, no. 4, p. 044104, Jul. 2016.
- [36] A. P. Kuo, N. Bhattacharjee, Y. Lee, K. Castro, Y. T. Kim, and A. Folch, “High-

- Precision Stereolithography of Biomicrofluidic Devices,” *Adv. Mater. Technol.*, vol. 4, no. 6, p. 1800395, Jun. 2019.
- [37] K. Plevniak, M. Campbell, T. Myers, A. Hodges, and M. He, “3D printed auto-mixing chip enables rapid smartphone diagnosis of anemia,” *Biomicrofluidics*, vol. 10, no. 5, p. 054113, Sep. 2016.
- [38] H. Kodama, “Automatic method for fabricating a three-dimensional plastic model with photo-hardening polymer,” *Rev. Sci. Instrum.*, vol. 52, no. 11, pp. 1770–1773, 1981.
- [39] R. Amin *et al.*, “3D-printed microfluidic devices,” *Biofabrication*, vol. 8, no. 2. Institute of Physics Publishing, p. 022001, 20-Jun-2016.
- [40] W. Cheng, J. Y. H. Fuh, A. Y. C. Nee, Y. S. Wong, H. T. Loh, and T. Miyazawa, “Multi-objective optimization of partbuilding orientation in stereolithography,” *Rapid Prototyp. J.*, vol. 1, no. 4, pp. 12–23, Jan. 1995.
- [41] “EBSCOhost | 147473265 | Something old and something new: Transitioning from analogue to digital technologies through 2d and 3d modelling in the classroom.” [Online]. Available: https://web.a.ebscohost.com/abstract?direct=true&profile=ehost&scope=site&auth_type=crawler&jrnl=10321942&AN=147473265&h=EroitAyS1JQzwNjbSDgP7Iq5CB%2Bj5uoXJbTointalbcUr%2FEZxG3oi0xWmiYQU4B0fMO15oO86FmByS0w36rK5g%3D%3D&cr=c&resultNs=AdminWebAuth&resultLocal=ErrCrINotAuth&crIhashurl=login.aspx%3Fdirect%3Dtrue%26profile%3Dehost%26scope%3Dsite%26authtype%3Dcrawler%26jrnl%3D10321942%26AN%3D147473265. [Accessed: 22-Feb-2021].
- [42] J. Aspler, A. Kingsland, L. M. Cormier, and X. Zou, “3D PRINTING – A REVIEW OF TECHNOLOGIES, MARKETS, AND OPPORTUNITIES FOR THE FOREST INDUSTRY,” 2016.
- [43] T. Wohlers and T. Gornet, “History of Additive Manufacturing,” 2016.
- [44] T. Nakamoto and K. Yamaguchi, “Consideration on the producing of high aspect ratio micro parts using UV sensitive photopolymer,” in *Proceedings of the International Symposium on Micro Machine and Human Science*, 1996, pp. 53–58.
- [45] A. Bertsch, S. Zissi, J. Y. Jézéquel, S. Corbel, and J. C. André, “Microstereophotolithography using a liquid crystal display as dynamic mask-generator,” *Microsyst. Technol.*, vol. 3, no. 2, pp. 42–47, 1997.
- [46] M. Krkobabić, D. Medarević, N. Pešić, D. Vasiljević, B. Ivković, and S. Ibrić, “Digital Light Processing (DLP) 3D Printing of Atomoxetine Hydrochloride Tablets Using Photoreactive Suspensions,” *Pharmaceutics*, vol. 12, no. 9, p. 833, Aug. 2020.
- [47] E. Schwarzer, M. Götz, D. Markova, D. Stafford, U. Scheithauer, and T. Moritz, “Lithography-based ceramic manufacturing (LCM) – Viscosity and cleaning as two quality influencing steps in the process chain of printing green parts,” *J. Eur. Ceram. Soc.*, vol. 37, no. 16, pp. 5329–5338, Dec. 2017.
- [48] Z. Chen *et al.*, “3D printing of ceramics: A review,” *Journal of the European Ceramic Society*, vol. 39, no. 4. Elsevier Ltd, pp. 661–687, 01-Apr-2019.
- [49] M. C. Hacker, J. Krieghoff, and A. G. Mikos, “Synthetic Polymers,” in *Principles of Regenerative Medicine*, Elsevier, 2019, pp. 559–590.
- [50] L. M. Rios, C. Moore, and P. R. Jones, “Persistent organic pollutants carried by synthetic polymers in the ocean environment,” *Mar. Pollut. Bull.*, vol. 54, no. 8, pp. 1230–1237, Aug. 2007.
- [51] S. Coveney, *Fundamentals of Phase Separation in Polymer Blend Thin Films*. 2015.
- [52] V. V. Pokropivny and V. V. Skorokhod, “Classification of nanostructures by dimensionality and concept of surface forms engineering in nanomaterial science,” *Mater. Sci. Eng. C*, vol. 27, no. 5-8 SPEC. ISS., pp. 990–993, Sep. 2007.
- [53] Y. Yina and D. Talapin, “The chemistry of functional nanomaterials,” *Chem. Soc. Rev.*, vol. 42, no. 7, pp. 2484–2487, Mar. 2013.

- [54] S. Mukherji, S. Bharti, G. Shukla, and S. Mukherji, "Synthesis and characterization of size- And shape-controlled silver nanoparticles," *Physical Sciences Reviews*, vol. 4, no. 1. De Gruyter, 01-Jan-2019.
- [55] H. J. Hageman, "Photoinitiators for free radical polymerization," *Prog. Org. Coatings*, vol. 13, no. 2, pp. 123–150, Mar. 1985.
- [56] E. Andrzejewska, "Photopolymerization kinetics of multifunctional monomers," *Progress in Polymer Science (Oxford)*, vol. 26, no. 4. Pergamon, pp. 605–665, 01-May-2001.
- [57] N. A. Mohd Radzuan, A. B. Sulong, and J. Sahari, "A review of electrical conductivity models for conductive polymer composite," *Int. J. Hydrogen Energy*, vol. 42, no. 14, pp. 9262–9273, Apr. 2017.
- [58] S. Maity and A. Chatterjee, "Conductive polymer-based electro-conductive textile composites for electromagnetic interference shielding: A review," *J. Ind. Text.*, vol. 47, no. 8, pp. 2228–2252, May 2018.
- [59] Y. Bréchet *et al.*, "Polymer based nanocomposites: Effect of filler-filler and filler-matrix interactions," *Adv. Eng. Mater.*, vol. 3, no. 8, pp. 571–577, Aug. 2001.
- [60] K. Gnanasekaran *et al.*, "3D printing of CNT- and graphene-based conductive polymer nanocomposites by fused deposition modeling," *Appl. Mater. Today*, vol. 9, pp. 21–28, Dec. 2017.
- [61] R. Zhou, P. Li, Z. Fan, D. Du, and J. Ouyang, "Stretchable heaters with composites of an intrinsically conductive polymer, reduced graphene oxide and an elastomer for wearable thermotherapy †," *J. Mater. Chem. C*, vol. 5, p. 1544, 2017.
- [62] G. C. Psarras, E. Manolakaki, and G. M. Tsangaris, "Electrical relaxations in polymeric particulate composites of epoxy resin and metal particles," *Compos. - Part A Appl. Sci. Manuf.*, vol. 33, no. 3, pp. 375–384, Mar. 2002.
- [63] Y. Wang and X. Jing, "Intrinsically conducting polymers for electromagnetic interference shielding," *Polym. Adv. Technol.*, vol. 16, no. 4, pp. 344–351, Apr. 2005.
- [64] C. Li, M. Liu, N. G. Pschirer, M. Baumgarten, and K. Müllen, "Polyphenylene-based materials for organic photovoltaics," *Chem. Rev.*, vol. 110, no. 11, pp. 6817–6855, Nov. 2010.
- [65] "NOPR: Thermal and conducting behaviour of emeraldine base (EB) form of polyaniline (PANI)." [Online]. Available: <http://nopr.niscair.res.in/handle/123456789/11620>. [Accessed: 08-Nov-2020].
- [66] S. Hotta, M. Soga, and N. Sonoda, "Novel organosynthetic routes to polythiophene and its derivatives," *Synth. Met.*, vol. 26, no. 3, pp. 267–279, Nov. 1988.
- [67] D. N. Nguyen and H. Yoon, "Recent advances in nanostructured conducting polymers: From synthesis to practical applications," *Polymers*, vol. 8, no. 4. MDPI AG, p. 118, 31-Mar-2016.
- [68] C. H. Choi, S. H. Park, and S. I. Woo, "Binary and ternary doping of nitrogen, boron, and phosphorus into carbon for enhancing electrochemical oxygen reduction activity," *ACS Nano*, vol. 6, no. 8, pp. 7084–7091, Aug. 2012.
- [69] C. K. Chiang *et al.*, "Electrical conductivity in doped polyacetylene," *Phys. Rev. Lett.*, vol. 39, no. 17, pp. 1098–1101, Oct. 1977.
- [70] R. D. Mccullough, "The Chemistry of Conducting Polythiophenes**."
- [71] R. J. Waltman, J. Bargon, and A. F. Diaz, "Electrochemical studies of some conducting polythiophene films," *J. Phys. Chem.*, vol. 87, no. 8, pp. 1459–1463, Apr. 1983.
- [72] T. Yamamoto, "Electrically conducting and thermally stable π -conjugated poly(arylene)s prepared by organometallic processes," *Progress in Polymer Science*, vol. 17, no. 6. Pergamon, pp. 1153–1205, 01-Jan-1992.
- [73] M. Döbbelin *et al.*, "Electrochemical synthesis of PEDOT derivatives bearing imidazolium-ionic liquid moieties," *J. Polym. Sci. Part A Polym. Chem.*, vol. 47, no. 12, pp. 3010–3021, Jun. 2009.

- [74] S. Akoudad and J. Roncali, "Electrochemical synthesis of poly(3,4-ethylenedioxythiophene) from a dimer precursor," *Synth. Met.*, vol. 93, no. 2, pp. 111–114, Mar. 1998.
- [75] K. Yamamoto *et al.*, "Oligothiophene quinoids containing a benzo[: C] thiophene unit for the stabilization of the quinoidal electronic structure," *J. Mater. Chem. C*, vol. 6, no. 28, pp. 7493–7500, Jul. 2018.
- [76] J. D. Morris and C. K. Payne, "Tuning PEDOT:PSS conductivity with iron oxidants," *Org. Electron.*, vol. 15, no. 7, pp. 1707–1710, Jul. 2014.
- [77] J. Hwang, F. Amy, and A. Kahn, "Spectroscopic study on sputtered PEDOT · PSS: Role of surface PSS layer," *Org. Electron.*, vol. 7, no. 5, pp. 387–396, Oct. 2006.
- [78] L. Groenendaal, F. Jonas, D. Freitag, H. Pielartzik, and J. R. Reynolds, "Poly(3,4-ethylenedioxythiophene) and Its Derivatives: Past, Present, and Future," *Adv. Mater.*, vol. 12, no. 7, pp. 481–494, Apr. 2000.
- [79] I. Cooperstein *et al.*, "Hybrid Materials for Functional 3D Printing," *Adv. Mater. Interfaces*, vol. 5, no. 22, p. 1800996, Nov. 2018.
- [80] X. Li *et al.*, "3D Printing of Flexible Liquid Sensor Based on Swelling Behavior of Hydrogel with Carbon Nanotubes," *Adv. Mater. Technol.*, vol. 4, no. 2, p. 1800476, Feb. 2019.
- [81] J. H. Kim *et al.*, "Three-Dimensional Printing of Highly Conductive Carbon Nanotube Microarchitectures with Fluid Ink," *ACS Nano*, vol. 10, no. 9, pp. 8879–8887, Sep. 2016.
- [82] E. Fantino *et al.*, "3D Printing/Interfacial Polymerization Coupling for the Fabrication of Conductive Hydrogel," *Macromol. Mater. Eng.*, vol. 303, no. 4, p. 1700356, Apr. 2018.
- [83] U. Kalsoom, P. N. Nesterenko, and B. Paull, "Recent developments in 3D printable composite materials," *RSC Advances*, vol. 6, no. 65. Royal Society of Chemistry, pp. 60355–60371, 21-Jun-2016.
- [84] "(8) Electrically Conductive Strain Sensing Polyurethane Nanocomposites with Synergistic Carbon Nanotubes and Graphene Bifillers | Request PDF." [Online]. Available: https://www.researchgate.net/publication/303595291_Electrically_Conductive_Strain_Sensing_Polyurethane_Nanocomposites_with_Synergistic_Carbon_Nanotubes_and_Graphene_Bifillers. [Accessed: 11-Mar-2020].
- [85] Y. Liu, W. Xiong, L. J. Jiang, Y. S. Zhou, and Y. F. Lu, "Precise 3D printing of micro/nanostructures using highly conductive carbon nanotube-thiol-acrylate composites," in *Laser 3D Manufacturing III*, 2016, vol. 9738, p. 973808.
- [86] N. Hu, Z. Masuda, G. Yamamoto, H. Fukunaga, T. Hashida, and J. Qiu, "Effect of fabrication process on electrical properties of polymer/multi-wall carbon nanotube nanocomposites," *Compos. Part A Appl. Sci. Manuf.*, vol. 39, no. 5, pp. 893–903, May 2008.
- [87] S. Ghoshal, "Polymer/carbon nanotubes (CNT) nanocomposites processing using additive manufacturing (three-dimensional printing) technique: An overview," *Fibers*, vol. 5, no. 4. MDPI Multidisciplinary Digital Publishing Institute, p. 40, 01-Dec-2017.
- [88] E. Balliu, H. Andersson, M. Engholm, T. Öhlund, H. E. Nilsson, and H. Olin, "Selective laser sintering of inkjet-printed silver nanoparticle inks on paper substrates to achieve highly conductive patterns," *Sci. Rep.*, vol. 8, no. 1, p. 10408, Dec. 2018.
- [89] M. Mohl, A. Dombovari, R. Vajtai, P. M. Ajayan, and K. Kordas, "Self-assembled large scale metal alloy grid patterns as flexible transparent conductive layers," *Sci. Rep.*, vol. 5, no. 1, p. 13710, Nov. 2015.
- [90] K. Kim *et al.*, "3D Optical Printing of Piezoelectric Nanoparticle–Polymer Composite Materials," 2014.
- [91] A. T. Cullen and A. D. Price, "Digital light processing for the fabrication of 3D intrinsically conductive polymer structures," *Synth. Met.*, vol. 235, pp. 34–41, Jan.

- 2018.
- [92] A. T. Cullen and A. D. Price, "Fabrication of 3D conjugated polymer structures via vat polymerization additive manufacturing," *Smart Mater. Struct.*, vol. 28, no. 10, p. 104007, Sep. 2019.
- [93] S. Politi, E. Tamburri, R. Carcione, T. Lavecchia, M. Angjellari, and M. L. Terranova, "Innovative preparation processes and structural characteristics of 3D printable polymer-based nanocomposites," in *AIP Conference Proceedings*, 2019, vol. 2196, no. 1, p. 020020.
- [94] T. Distler and A. R. Boccaccini, "3D printing of electrically conductive hydrogels for tissue engineering and biosensors – A review," *Acta Biomaterialia*, vol. 101. Acta Materialia Inc, pp. 1–13, 01-Jan-2020.
- [95] Y. Wu *et al.*, "Fabrication of conductive gelatin methacrylate-polyaniline hydrogels," *Acta Biomater.*, vol. 33, pp. 122–130, Mar. 2016.
- [96] Y. Hui, C. Bian, S. Xia, J. Tong, and J. Wang, "Synthesis and electrochemical sensing application of poly(3,4-ethylenedioxythiophene)-based materials: A review," *Analytica Chimica Acta*, vol. 1022. Elsevier B.V., pp. 1–19, 31-Aug-2018.
- [97] V. Bertana *et al.*, "3D-printed microfluidics on thin poly(methyl methacrylate) substrates for genetic applications," *J. Vac. Sci. Technol. B, Nanotechnol. Microelectron. Mater. Process. Meas. Phenom.*, vol. 36, no. 1, p. 01A106, Jan. 2018.
- [98] F. Perrucci, "High Performance & Smart Manufacturing," Sep. 2018.
- [99] H. Xing *et al.*, "Preparation and characterization of UV curable Al₂O₃ suspensions applying for stereolithography 3D printing ceramic microcomponent," *Powder Technol.*, vol. 338, pp. 153–161, Oct. 2018.
- [100] G. Gonzalez *et al.*, "Development of 3D printable formulations containing CNT with enhanced electrical properties," *Polym. (United Kingdom)*, vol. 109, pp. 246–253, Jan. 2017.
- [101] M. G. Neumann, W. G. Miranda, C. C. Schmitt, F. A. Rüggeberg, and I. C. Correa, "Molar extinction coefficients and the photon absorption efficiency of dental photoinitiators and light curing units," *J. Dent.*, vol. 33, no. 6, pp. 525–532, Jul. 2005.
- [102] J. H. Moon, Y. G. Shul, H. S. Han, S. Y. Hong, Y. S. Choi, and H. T. Kim, "A study on UV-curable adhesives for optical pick-up: I. Photo-initiator effects," *Int. J. Adhes. Adhes.*, vol. 25, no. 4, pp. 301–312, Aug. 2005.
- [103] Z. F. Zhang, X. Ma, H. Wang, and F. Ye, "Influence of polymerization conditions on the refractive index of poly(ethylene glycol) diacrylate (PEGDA) hydrogels," *Appl. Phys. A Mater. Sci. Process.*, vol. 124, no. 4, pp. 1–6, Apr. 2018.
- [104] V. B. Morris, S. Nimbalkar, M. Younesi, P. McClellan, and O. Akkus, "Mechanical Properties, Cytocompatibility and Manufacturability of Chitosan:PEGDA Hybrid-Gel Scaffolds by Stereolithography," *Ann. Biomed. Eng.*, vol. 45, no. 1, pp. 286–296, Jan. 2017.
- [105] J. Kim, J. G. Jang, J. I. Hong, S. H. Kim, and J. Kwak, "Sulfuric acid vapor treatment for enhancing the thermoelectric properties of PEDOT:PSS thin-films," *J. Mater. Sci. Mater. Electron.*, vol. 27, no. 6, pp. 6122–6127, Jun. 2016.
- [106] J. Ouyang, "'secondary doping' methods to significantly enhance the conductivity of PEDOT:PSS for its application as transparent electrode of optoelectronic devices," *Displays*, vol. 34, no. 5, pp. 423–436, Dec. 2013.
- [107] H. Shi, C. Liu, Q. Jiang, and J. Xu, "Effective Approaches to Improve the Electrical Conductivity of PEDOT:PSS: A Review," *Adv. Electron. Mater.*, vol. 1, no. 4, p. 1500017, Apr. 2015.
- [108] S. Duan, L. Zhang, Z. Wang, and C. Li, "One-step rod coating of high-performance silver nanowire-PEDOT:PSS flexible electrodes with enhanced adhesion after sulfuric acid post-treatment," *RSC Adv.*, vol. 5, no. 115, pp. 95280–95286, Nov. 2015.
- [109] W. Meng *et al.*, "Conductivity Enhancement of PEDOT:PSS Films via Phosphoric

- Acid Treatment for Flexible All-Plastic Solar Cells,” *ACS Appl. Mater. Interfaces*, vol. 7, no. 25, pp. 14089–14094, Jul. 2015.
- [110] C. S. Pathak, J. P. Singh, and R. Singh, “Optimizing the electrical properties of PEDOT:PSS films by co-solvents and their application in polymer photovoltaic cells,” *Appl. Phys. Lett.*, vol. 111, no. 10, p. 102107, Sep. 2017.
- [111] Y. Xia, K. Sun, and J. Ouyang, “Solution-Processed Metallic Conducting Polymer Films as Transparent Electrode of Optoelectronic Devices,” *Adv. Mater.*, vol. 24, no. 18, pp. 2436–2440, May 2012.
- [112] T. H. Chiang and T. E. Hsieh, “A study of encapsulation resin containing hexagonal boron nitride (hBN) as inorganic filler,” *J. Inorg. Organomet. Polym. Mater.*, vol. 16, no. 2, pp. 175–183, Jun. 2006.
- [113] H. Sun *et al.*, “Interfacial polarization and dielectric properties of aligned carbon nanotubes/polymer composites: The role of molecular polarity,” *Compos. Sci. Technol.*, vol. 154, pp. 145–153, Jan. 2018.
- [114] F. Tan, J. Liu, M. Liu, and J. Wang, “Charge density is more important than charge polarity in enhancing osteoblast-like cell attachment on poly(ethylene glycol)-diacrylate hydrogel,” *Mater. Sci. Eng. C*, vol. 76, pp. 330–339, Jul. 2017.
- [115] L. He, D. Lin, Y. Wang, Y. Xiao, and J. Che, “Electroactive SWNT/PEGDA hybrid hydrogel coating for bio-electrode interface,” *Colloids Surfaces B Biointerfaces*, vol. 87, no. 2, pp. 273–279, Oct. 2011.
- [116] P. Wilson, C. Lekakou, and J. F. Watts, “In-plane conduction characterisation and charge transport model of DMSO co-doped, inkjet printed Poly(3,4-ethylenedioxythiophene): Polystyrene sulfonate (PEDOT:PSS),” *Org. Electron.*, vol. 14, no. 12, pp. 3277–3285, Dec. 2013.
- [117] J. Parameswaranpillai, S. Thomas, and Y. Grohens, “Polymer Blends: State of the Art, New Challenges, and Opportunities,” in *Characterization of Polymer Blends*, Weinheim, Germany: Wiley-VCH Verlag GmbH & Co. KGaA, 2014, pp. 1–6.
- [118] C. V Adake, P. Bhargava, and P. Gandhi, “Effect of surfactant on dispersion of alumina in photopolymerizable monomers and their UV curing behavior for microstereolithography,” *Ceram. Int.*, vol. 41, no. 4, pp. 5301–5308, May 2015.
- [119] F. Inam, A. Heaton, P. Brown, T. Peijs, and M. J. Reece, “Effects of dispersion surfactants on the properties of ceramic-carbon nanotube (CNT) nanocomposites,” *Ceram. Int.*, vol. 40, no. 1, pp. 511–516, 2014.
- [120] J.-B. Lee, K. Rana, B. H. Seo, J. Y. Oh, U. Jeong, and J.-H. Ahn, “Influence of nonionic surfactant-modified PEDOT:PSS on graphene,” *Carbon N. Y.*, vol. 85, pp. 261–268, 2015.
- [121] N. Razali, D. Merom, M. Sawawi, ... M. M.-... O. I. A., and undefined 2018, “Effect of Surfactants to The Electrical Properties of The Hole Transporting Layer of Organic Solar Cells.”
- [122] Z. Fan, D. Du, Z. Yu, P. Li, Y. Xia, and J. Ouyang, “Significant Enhancement in the Thermoelectric Properties of PEDOT:PSS Films through a Treatment with Organic Solutions of Inorganic Salts,” *ACS Appl. Mater. Interfaces*, vol. 8, no. 35, pp. 23204–23211, Sep. 2016.
- [123] C. Gong, H. Bin Yang, Q. L. Song, Z. S. Lu, and C. M. Li, “Mechanism for dimethylformamide-treatment of poly(3,4-ethylenedioxythiophene): poly(styrene sulfonate) layer to enhance short circuit current of polymer solar cells,” *Sol. Energy Mater. Sol. Cells*, vol. 100, pp. 115–119, May 2012.
- [124] J. Park, A. Lee, Y. Yim, and E. Han, “Electrical and thermal properties of PEDOT:PSS films doped with carbon nanotubes,” *Synth. Met.*, vol. 161, no. 5, pp. 523–527, 2011.
- [125] I. Cruz-Cruz, M. Reyes-Reyes, M. A. Aguilar-Frutis, A. G. Rodriguez, and R. López-Sandoval, “Study of the effect of DMSO concentration on the thickness of the PSS insulating barrier in PEDOT:PSS thin films,” *Synth. Met.*, vol. 160, no. 13–14, pp. 1501–1506, Jul. 2010.
- [126] S.-S. Yoon and D.-Y. Khang, “Roles of Nonionic Surfactant Additives in PEDOT:PSS Thin Films,” *J. Phys. Chem. C*, vol. 120, no. 51, pp. 29525–29532,

Dec. 2016.

- [127] I. Lee, G. W. Kim, M. Yang, and T. S. Kim, "Simultaneously Enhancing the Cohesion and Electrical Conductivity of PEDOT:PSS Conductive Polymer Films using DMSO Additives," *ACS Appl. Mater. Interfaces*, vol. 8, no. 1, pp. 302–310, Jan. 2016.
- [128] A. B. Jódar-Reyes, A. Martín-Rodríguez, and J. L. Ortega-Vinuesa, "Effect of the ionic surfactant concentration on the stabilization/destabilization of polystyrene colloidal particles," *J. Colloid Interface Sci.*, vol. 298, no. 1, pp. 248–257, Jun. 2006.
- [129] Ö. Topel, B. A. Çakir, L. Budama, and N. Hoda, "Determination of critical micelle concentration of polybutadiene-block-poly(ethyleneoxide) diblock copolymer by fluorescence spectroscopy and dynamic light scattering," *J. Mol. Liq.*, vol. 177, pp. 40–43, Jan. 2013.
- [130] M. Z. Seyedin, J. M. Razal, P. C. Innis, and G. G. Wallace, "Strain-Responsive Polyurethane/PEDOT:PSS Elastomeric Composite Fibers with High Electrical Conductivity," *Adv. Funct. Mater.*, vol. 24, no. 20, pp. 2957–2966, May 2014.
- [131] K. Kurselis, R. Kiyani, V. N. Bagratashvili, V. K. Popov, and B. N. Chichkov, "3D fabrication of all-polymer conductive microstructures by two photon polymerization," *Opt. Express*, vol. 21, no. 25, p. 31029, Dec. 2013.
- [132] C. Sciancalepore, F. Moroni, M. Messori, and F. Bondioli, "Acrylate-based silver nanocomposite by simultaneous polymerization–reduction approach via 3D stereolithography," *Compos. Commun.*, vol. 6, pp. 11–16, Dec. 2017.
- [133] Z. Weng, Y. Zhou, W. Lin, T. Senthil, and L. Wu, "Structure-property relationship of nano enhanced stereolithography resin for desktop SLA 3D printer," *Compos. Part A Appl. Sci. Manuf.*, vol. 88, no. 88, pp. 234–242, Sep. 2016.
- [134] A. Priola, G. Gozzelino, F. Ferrero, and G. Malucelli, "Properties of polymeric films obtained from u.v. cured poly(ethylene glycol) diacrylates," *Polymer (Guildf.)*, vol. 34, no. 17, pp. 3653–3657, Sep. 1993.
- [135] T. Scherzer, R. Mehnert, and H. Lucht, "On-line monitoring of the acrylate conversion in UV photopolymerization by near-infrared reflection spectroscopy," *Macromol. Symp.*, vol. 205, no. 1, pp. 151–162, Jan. 2004.
- [136] R. Nazar, M. Sangermano, A. Vitale, and R. Bongiovanni, "Silver polymer nanocomposites by photoreduction of AgNO₃ and simultaneous photocrosslinking of the acrylic matrix: Effect of PVP on Ag particle formation," *J. Polym. Eng.*, vol. 38, no. 8, pp. 803–809, Sep. 2018.
- [137] S. Molina-Gutiérrez *et al.*, "Photoinduced Polymerization of Eugenol-Derived Methacrylates," *Molecules*, vol. 25, no. 15, p. 3444, Jul. 2020.
- [138] Y. Xia, K. Sun, and J. Ouyang, "Solution-Processed Metallic Conducting Polymer Films as Transparent Electrode of Optoelectronic Devices," *Adv. Mater.*, vol. 24, no. 18, pp. 2436–2440, May 2012.
- [139] N. Saxena, J. Keilhofer, A. K. Maurya, G. Fortunato, J. Overbeck, and P. Müller-Buschbaum, "Facile Optimization of Thermoelectric Properties in PEDOT:PSS Thin Films through Acido-Base and Redox Dedoping Using Readily Available Salts," *ACS Appl. Energy Mater.*, vol. 1, no. 2, pp. 336–342, Feb. 2018.
- [140] J. Ouyang, C. W. Chu, F. C. Chen, Q. Xu, and Y. Yang, "Polymer optoelectronic devices with high-conductivity poly(3,4-ethylenedioxythiophene) anodes," in *Journal of Macromolecular Science - Pure and Applied Chemistry*, 2004, vol. 41 A, no. 12, pp. 1497–1511.
- [141] M. Łapkowski and A. Proń, "Electrochemical oxidation of poly(3,4-ethylenedioxythiophene) - 'in situ' conductivity and spectroscopic investigations," *Synth. Met.*, vol. 110, no. 1, pp. 79–83, Mar. 2000.
- [142] J. Zhang *et al.*, "Fast and scalable wet-spinning of highly conductive PEDOT:PSS fibers enables versatile applications," *J. Mater. Chem. A*, vol. 7, no. 11, pp. 6401–6410, Mar. 2019.
- [143] P.-W. Sze, K.-W. Lee, P.-C. Huang, D.-W. Chou, B.-S. Kao, and C.-J. Huang, "The Investigation of High Quality PEDOT:PSS Film by Multilayer-Processing

- and Acid Treatment,” *Energies*, vol. 10, no. 5, p. 716, May 2017.
- [144] D. A. Mengistie, C.-H. Chen, K. M. Boopathi, F. W. Pranoto, L.-J. Li, and C.-W. Chu, “Enhanced Thermoelectric Performance of PEDOT:PSS Flexible Bulky Papers by Treatment with Secondary Dopants,” *ACS Appl. Mater. Interfaces*, vol. 7, no. 1, pp. 94–100, Jan. 2015.
- [145] D. A. Mengistie, P.-C. Wang, and C.-W. Chu, “Highly Conductive PEDOT: PSS Electrode Treated with Polyethylene Glycol for ITO-Free Polymer Solar Cells,” *ECS Trans.*, vol. 58, no. 11, pp. 49–56, Aug. 2013.
- [146] M. A. Siguan and R. Fischer, “Development and Characterization of a Hydrogel for Flexible and Stretchable Substrates.”
- [147] Y. Li *et al.*, “Fabrication of high-aspect-ratio 3D hydrogel microstructures using optically induced electrokinetics,” *Micromachines*, vol. 7, no. 4, Apr. 2016.
- [148] E. Azad, M. Atai, M. Zandi, P. Shokrollahi, and L. Solhi, “Structure–properties relationships in dental adhesives: Effect of initiator, matrix monomer structure, and nano-filler incorporation,” *Dent. Mater.*, vol. 34, no. 9, pp. 1263–1270, Sep. 2018.
- [149] A. V. Genis and A. V. Kuznetsov, “The relationship of the activity of the filler and the structure of the polymer matrix with the properties of composite fibre material,” *Int. Polym. Sci. Technol.*, vol. 44, no. 12, pp. T39–T46, Sep. 2017.
- [150] N. Kim *et al.*, “Highly Conductive PEDOT:PSS Nanofibrils Induced by Solution-Processed Crystallization,” *Adv. Mater.*, vol. 26, no. 14, pp. 2268–2272, Apr. 2014.
- [151] C. M. Cheah, J. Y. H. Fuh, A. Y. C. Nee, and L. Lu, “Mechanical characteristics of fiber-filled photo-polymer used in stereolithography,” *Rapid Prototyp. J.*, vol. 5, no. 3, pp. 112–119, 1999.
- [152] J. Zhou, Z. Yao, Y. Chen, D. Wei, Y. Wu, and T. Xu, “Mechanical and thermal properties of graphene oxide/phenolic resin composite,” *Polym. Compos.*, vol. 34, no. 8, pp. 1245–1249, Aug. 2013.
- [153] S. L. Marasso *et al.*, “PLA conductive filament for 3D printed smart sensing applications,” *Rapid Prototyp. J.*, vol. 24, no. 4, pp. 739–743, May 2018.
- [154] C. Zhu *et al.*, “Highly compressible 3D periodic graphene aerogel microlattices,” *Nat. Commun.*, vol. 6, no. 1, pp. 1–8, Apr. 2015.
- [155] J. R. C. Dizon, A. H. Espera, Q. Chen, and R. C. Advincula, “Mechanical characterization of 3D-printed polymers,” *Additive Manufacturing*, vol. 20. Elsevier B.V., pp. 44–67, 01-Mar-2018.
- [156] N. G. Tanikella, B. Wittbrodt, and J. M. Pearce, “Tensile strength of commercial polymer materials for fused filament fabrication 3D printing,” *Addit. Manuf.*, vol. 15, pp. 40–47, May 2017.
- [157] H. J. O’Connor, A. N. Dickson, and D. P. Dowling, “Evaluation of the mechanical performance of polymer parts fabricated using a production scale multi jet fusion printing process,” *Addit. Manuf.*, vol. 22, pp. 381–387, Aug. 2018.
- [158] Y. Xiao, L. He, and J. Che, “An effective approach for the fabrication of reinforced composite hydrogel engineered with SWNTs, polypyrrole and PEGDA hydrogel,” *J. Mater. Chem.*, vol. 22, no. 16, pp. 8076–8082, Apr. 2012.
- [159] Z. Drira, “INVESTIGATION OF THE MECHANICAL PROPERTIES OF POLY (ETHYLENE GLYCOL) DIACRYLATE BY NANOINDENTATION USING ATOMIC FORCE MICROSCOPY USING ATOMIC FORCE MICROSCOPY
Downloaded from Downloaded from.”
- [160] M. ElMahmoudy, S. Inal, A. Charrier, I. Uguz, G. G. Malliaras, and S. Sanaur, “Tailoring the Electrochemical and Mechanical Properties of PEDOT:PSS Films for Bioelectronics,” *Macromol. Mater. Eng.*, vol. 302, no. 5, p. 1600497, May 2017.
- [161] E. Fantino *et al.*, “3D Printing/Interfacial Polymerization Coupling for the Fabrication of Conductive Hydrogel,” *Macromol. Mater. Eng.*, vol. 303, no. 4, p.

- 1700356, Apr. 2018.
- [162] M. Sudheer, R. Prabhu, K. Raju, and T. Bhat, "Effect of filler content on the performance of epoxy/PTW composites," *Adv. Mater. Sci. Eng.*, vol. 2014, 2014.
- [163] A. Pegoretti, A. Dorigato, M. Brugnara, and A. Penati, "Contact angle measurements as a tool to investigate the filler-matrix interactions in polyurethane-clay nanocomposites from blocked prepolymer," *Eur. Polym. J.*, vol. 44, no. 6, pp. 1662–1672, Jun. 2008.
- [164] D. Castro, D. Conchouso, Y. Fan, and I. G. Foulds, "SURFACE TREATMENTS OF SOFT MOLDS FOR HIGH ASPECT RATIO MOLDING OF POLY-PEGDA." 2012.
- [165] S. Gholami, A. Rezvani, V. Vatanpour, and J. L. Cortina, "Improving the chlorine resistance property of polyamide TFC RO membrane by polyethylene glycol diacrylate (PEGDA) coating," *Desalination*, vol. 443, pp. 245–255, Oct. 2018.
- [166] S. H. Lee, J. S. Sohn, S. B. Kulkarni, U. M. Patil, S. C. Jun, and J. H. Kim, "Modified physico-chemical properties and supercapacitive performance via DMSO inducement to PEDOT:PSS active layer," *Org. Electron.*, vol. 15, no. 12, pp. 3423–3430, 2014.
- [167] V. Karagkiozaki *et al.*, "Bioelectronics meets nanomedicine for cardiovascular implants: PEDOT-based nanocoatings for tissue regeneration," *Biochim. Biophys. Acta - Gen. Subj.*, vol. 1830, no. 9, pp. 4294–4304, Sep. 2013.
- [168] S. Wu, *Polymer interface and adhesion*. CRC Press, 2017.
- [169] C. Duc, A. Vlandas, G. G. Malliaras, and V. Senez, "Wettability of PEDOT:PSS films," *Soft Matter*, vol. 12, no. 23, pp. 5146–5153, Jun. 2016.
- [170] R. N. Wenzel, "Surface roughness and contact angle," *J. Phys. Colloid Chem.*, vol. 53, no. 9, pp. 1466–1467, 1949.
- [171] G. Tan, Y. Wang, J. Li, and S. Zhang, "Synthesis and characterization of injectable photocrosslinking poly (ethylene glycol) diacrylate based hydrogels," *Polym. Bull.*, vol. 61, no. 1, pp. 91–98, Jul. 2008.
- [172] F. Alifui-Segbaya, S. Varma, G. J. Lieschke, and R. George, "Biocompatibility of Photopolymers in 3D Printing," *3D Print. Addit. Manuf.*, vol. 4, no. 4, pp. 185–191, Dec. 2017.
- [173] H. Schweikl, G. Spagnuolo, and G. Schmalz, "Genetic and cellular toxicology of dental resin monomers," *Journal of Dental Research*, vol. 85, no. 10. SAGE Publications Inc., pp. 870–877, 12-Oct-2006.
- [174] M. Carve and D. Wlodkovic, "3D-Printed Chips: Compatibility of Additive Manufacturing Photopolymeric Substrata with Biological Applications," *Micromachines*, vol. 9, no. 2, p. 91, Feb. 2018.
- [175] A. Cavallo, M. Madaghiale, U. Masullo, M. G. Lionetto, and A. Sannino, "Photocrosslinked poly(ethylene glycol) diacrylate (PEGDA) hydrogels from low molecular weight prepolymer: Swelling and permeation studies," *J. Appl. Polym. Sci.*, vol. 134, no. 2, Jan. 2017.
- [176] K. McAvoy, D. Jones, and R. R. S. Thakur, "Synthesis and Characterisation of Photocrosslinked poly(ethylene glycol) diacrylate Implants for Sustained Ocular Drug Delivery," *Pharm. Res.*, vol. 35, no. 2, pp. 1–17, Feb. 2018.
- [177] Z. N. Wang, S. L. Shen, A. Zhou, and H. M. Lyu, "Experimental investigation of water-swelling characteristics of polymer materials for tunnel sealing gasket," *Constr. Build. Mater.*, vol. 256, p. 119473, Sep. 2020.
- [178] B. Verhaagen, T. Zanderink, and D. Fernandez Rivas, "Ultrasonic cleaning of 3D printed objects and Cleaning Challenge Devices," *Appl. Acoust.*, vol. 103, pp. 172–181, Feb. 2016.
- [179] J. Liu *et al.*, "Fullerene pipes," *Science (80-.)*, vol. 280, no. 5367, pp. 1253–1256, May 1998.
- [180] Royal College of Physicians, "Every breath we take: the lifelong impact of air pollution," 2016.
- [181] B. Szulczyński and J. Gębicki, "Currently Commercially Available Chemical Sensors Employed for Detection of Volatile Organic Compounds in Outdoor and

- Indoor Air,” *Environments*, vol. 4, no. 1, p. 21, Mar. 2017.
- [182] “Quartz Crystal Microbalance–Based Sensors,” *Handb. Immunoass. Technol.*, pp. 333–357, Jan. 2018.
- [183] J. C. Cates, “United States Patent Office CUMULATIVE DETECTOR FOR CHLORINE GAS,” Dec. 1963.
- [184] W. Small IV, D. J. Maitland, T. S. Wilson, J. P. Bearinger, S. A. Letts, and J. E. Trebes, “Development of a prototype optical hydrogen gas sensor using a getter-doped polymer transducer for monitoring cumulative exposure: Preliminary results,” *Sensors Actuators, B Chem.*, vol. 139, no. 2, pp. 375–379, Jun. 2009.
- [185] U. Lange and V. M. Mirsky, “Chemiresistors based on conducting polymers: A review on measurement techniques,” *Analytica Chimica Acta*, vol. 687, no. 2. Elsevier, pp. 105–113, 21-Feb-2011.
- [186] M. Hartwig, R. Zichner, and Y. Joseph, “Inkjet-Printed Wireless Chemiresistive Sensors—A Review,” *Chemosensors*, vol. 6, no. 4, p. 66, Dec. 2018.
- [187] Y. Seekaew, S. Lokavee, D. Phokharatkul, A. Wisitsoraat, T. Kerdcharoen, and C. Wongchoosuk, “Low-cost and flexible printed graphene-PEDOT:PSS gas sensor for ammonia detection,” *Org. Electron.*, vol. 15, no. 11, pp. 2971–2981, Nov. 2014.
- [188] S. Meng, J. Ma, and Y. Jiang, “Solvent effects on electronic structures and chain conformations of α -oligothiophenes in polar and apolar solutions,” *J. Phys. Chem. B*, vol. 111, no. 16, pp. 4128–4136, Apr. 2007.
- [189] H. Yoon, J. Y. Hong, and J. Jang, “Charge-transport behavior in shape-controlled poly(3,4- ethylenedioxythiophene) nanomaterials: Intrinsic and extrinsic factors,” *Small*, vol. 3, no. 10, pp. 1774–1783, Oct. 2007.
- [190] J. P. Thomas, L. Zhao, D. McGillivray, and K. T. Leung, “High-efficiency hybrid solar cells by nanostructural modification in PEDOT:PSS with co-solvent addition,” *J. Mater. Chem. A*, vol. 2, no. 7, pp. 2383–2389, Feb. 2014.
- [191] C. Dincer *et al.*, “Disposable Sensors in Diagnostics, Food, and Environmental Monitoring,” *Advanced Materials*, vol. 31, no. 30. Wiley-VCH Verlag, 26-Jul-2019.
- [192] M. F. Farooqui, M. A. Karimi, K. N. Salama, and A. Shamim, “3D-Printed Disposable Wireless Sensors with Integrated Microelectronics for Large Area Environmental Monitoring,” *Adv. Mater. Technol.*, vol. 2, no. 8, p. 1700051, Aug. 2017.
- [193] M. F. Mabrook, C. Pearson, and M. C. Petty, “Inkjet-printed polymer films for the detection of organic vapors,” *IEEE Sens. J.*, vol. 6, no. 6, pp. 1435–1443, Dec. 2006.
- [194] K. Dunst, J. Karczewski, and P. Jasiński, “Nitrogen dioxide sensing properties of PEDOT polymer films,” *Sensors Actuators B Chem.*, vol. 247, pp. 108–113, Aug. 2017.
- [195] V. Bertana *et al.*, “3D Printed Active Objects based on the Promising PEDOT: PSS Resin: Investigation of their Integration inside an Electronic Circuit,” *Int. J. Eng. Res. Technol.*, vol. 13, no. 3, pp. 462–469, 2020.
- [196] T. Villmow, S. Pegel, A. John, R. Rentenberger, and P. Pötschke, “Liquid sensing: Smart polymer/CNT composites,” *Mater. Today*, vol. 14, no. 7–8, pp. 340–345, Jul. 2011.
- [197] Z. C. Kennedy *et al.*, “3D-printed poly(vinylidene fluoride)/carbon nanotube composites as a tunable, low-cost chemical vapour sensing platform,” *Nanoscale*, vol. 9, no. 17, pp. 5458–5466, 2017.
- [198] S. Jambhulkar, W. Xu, R. Franklin, D. Ravichandran, Y. Zhu, and K. Song, “Integrating 3D printing and self-assembly for layered polymer/nanoparticle microstructures as high-performance sensors,” *J. Mater. Chem. C*, vol. 8, no. 28, pp. 9495–9501, Jul. 2020.
- [199] A. Falco, M. Petrelli, E. Bezzeccheri, A. Abdelhalim, and P. Lugli, “Towards 3D-printed organic electronics: Planarization and spray-deposition of functional layers onto 3D-printed objects,” *Org. Electron.*, vol. 39, pp. 340–347, Dec. 2016.

- [200] Y. Huang *et al.*, “Assembly and applications of 3D conformal electronics on curvilinear surfaces,” *Materials Horizons*, vol. 6, no. 4. Royal Society of Chemistry, pp. 642–683, 01-May-2019.
- [201] H. Baig, N. Sellami, D. Chemisana, J. Rosell, and T. K. Mallick, “Performance analysis of a dielectric based 3D building integrated concentrating photovoltaic system,” *Sol. Energy*, vol. 103, pp. 525–540, May 2014.
- [202] J. T. Muth *et al.*, “Embedded 3D printing of strain sensors within highly stretchable elastomers,” *Adv. Mater.*, vol. 26, no. 36, pp. 6307–6312, Sep. 2014.
- [203] S. Derakhshanfar, R. Mbeleck, K. Xu, X. Zhang, W. Zhong, and M. Xing, “3D bioprinting for biomedical devices and tissue engineering: A review of recent trends and advances,” *Bioactive Materials*, vol. 3, no. 2. KeAi Communications Co., pp. 144–156, 01-Jun-2018.
- [204] V. Bertana *et al.*, “Rapid prototyping of 3D Organic Electrochemical Transistors by composite photocurable resin,” *Sci. Rep.*, vol. 10, no. 1, p. 13335, Dec. 2020.
- [205] E. Bihar *et al.*, “Fully printed all-polymer tattoo/textile electronics for electromyography,” *Flex. Print. Electron.*, vol. 3, no. 3, p. 034004, Sep. 2018.
- [206] G. Tarabella, D. Vurro, S. Lai, P. D’Angelo, L. Ascari, and S. Iannotta, “Aerosol jet printing of PEDOT:PSS for large area flexible electronics,” *Flex. Print. Electron.*, vol. 5, no. 1, p. 014005, Jan. 2020.
- [207] G. Tarabella *et al.*, “Multifunctional operation of an organic device with three-dimensional architecture,” *Materials*, vol. 12, no. 8. MDPI AG, 2019.
- [208] J. Fan, C. Montemagno, and M. Gupta, “3D printed high transconductance organic electrochemical transistors on flexible substrates,” *Org. Electron.*, vol. 73, pp. 122–129, Oct. 2019.
- [209] M. Lyons and G. Keeley, “The Redox Behaviour of Randomly Dispersed Single Walled Carbon Nanotubes both in the Absence and in the Presence of Adsorbed Glucose Oxidase,” *Sensors*, vol. 6, no. 12, pp. 1791–1826, Dec. 2006.
- [210] J. Moldenhauer, M. Meier, and D. W. Paul, “Rapid and Direct Determination of Diffusion Coefficients Using Microelectrode Arrays,” *J. Electrochem. Soc.*, vol. 163, no. 8, pp. H672–H678, May 2016.
- [211] C. Liao, M. Zhang, L. Niu, Z. Zheng, and F. Yan, “Organic electrochemical transistors with graphene-modified gate electrodes for highly sensitive and selective dopamine sensors,” *J. Mater. Chem. B*, vol. 2, no. 2, pp. 191–200, 2014.
- [212] I. Gualandi, D. Tonelli, F. Mariani, E. Scavetta, M. Marzocchi, and B. Fraboni, “Selective detection of dopamine with an all PEDOT:PSS Organic Electrochemical Transistor,” *Sci. Rep.*, vol. 6, no. 1, p. 35419, 2016.
- [213] K. Tybrandt, S. B. Kollipara, and M. Berggren, “Organic electrochemical transistors for signal amplification in fast scan cyclic voltammetry,” *Sensors Actuators, B Chem.*, vol. 195, pp. 651–656, 2014.
- [214] W. Ji *et al.*, “Carbonized silk fabric-based flexible organic electrochemical transistors for highly sensitive and selective dopamine detection,” *Sensors Actuators B Chem.*, vol. 304, p. 127414, 2019.
- [215] S. Chumillas, M. C. Figueiredo, V. Climent, and J. M. Feliu, “Study of dopamine reactivity on platinum single crystalline electrode surfaces,” *Electrochim. Acta*, vol. 109, pp. 577–586, 2013.
- [216] H. Tang, P. Lin, H. L. W. Chan, and F. Yan, “Highly sensitive dopamine biosensors based on organic electrochemical transistors,” *Biosens. Bioelectron.*, vol. 26, no. 11, pp. 4559–4563, 2011.
- [217] D. A. Bernardis, D. J. Macaya, M. Nikolou, J. a. DeFranco, S. Takamatsu, and G. G. Malliaras, “Enzymatic sensing with organic electrochemical transistors,” *J. Mater. Chem.*, vol. 18, no. 1, p. 116, 2008.
- [218] P. D’Angelo *et al.*, “Nanomolar detection of the antitumor drug tamoxifen by flexible organic electrochemical devices,” *AIP Conf. Proc.*, vol. 1990, 2018.
- [219] N. Wang, Y. Liu, Y. Fu, and F. Yan, “AC Measurements Using Organic Electrochemical Transistors for Accurate Sensing,” *ACS Appl. Mater. Interfaces*, vol. 10, no. 31, pp. 25834–25840, 2018.

- [220] H. Yang, W. R. Leow, and X. Chen, "3D Printing of Flexible Electronic Devices," *Small Methods*, vol. 2, no. 1, p. 1700259, Jan. 2018.
- [221] N. Vargas-Alfredo, H. Reinecke, A. Gallardo, A. del Campo, and J. Rodríguez-Hernández, "Fabrication of 3D printed objects with controlled surface chemistry and topography," *Eur. Polym. J.*, vol. 98, pp. 21–27, Jan. 2018.
- [222] A. E. Jakus, N. R. Geisendorfer, P. L. Lewis, and R. N. Shah, "3D-printing porosity: A new approach to creating elevated porosity materials and structures," *Acta Biomater.*, vol. 72, pp. 94–109, May 2018.
- [223] "Capacitive energy storage in micro-scale devices: recent advances in design and fabrication of micro-supercapacitors - Energy & Environmental Science (RSC Publishing)." [Online]. Available: <https://pubs.rsc.org/en/content/articlelanding/2013/ee/c3ee43526a/unauth#!divAbstract>. [Accessed: 14-Sep-2020].
- [224] A. Tanwilaisiri, Y. Xu, R. Zhang, D. Harrison, J. Fyson, and M. Areir, "Design and fabrication of modular supercapacitors using 3D printing," *J. Energy Storage*, vol. 16, pp. 1–7, Apr. 2018.
- [225] M. Areir, Y. Xu, D. Harrison, and J. Fyson, "3D printing of highly flexible supercapacitor designed for wearable energy storage," *Mater. Sci. Eng. B Solid-State Mater. Adv. Technol.*, vol. 226, pp. 29–38, Dec. 2017.
- [226] X. Tian, J. Jin, S. Yuan, C. K. Chua, S. B. Tor, and K. Zhou, "Emerging 3D-Printed Electrochemical Energy Storage Devices: A Critical Review," *Advanced Energy Materials*, vol. 7, no. 17. Wiley-VCH Verlag, 06-Sep-2017.
- [227] S. Kholghi Eshkalak, A. Chinnappan, W. A. D. M. Jayathilaka, M. Khatibzadeh, E. Kowsari, and S. Ramakrishna, "A review on inkjet printing of CNT composites for smart applications," *Applied Materials Today*, vol. 9. Elsevier Ltd, pp. 372–386, 01-Dec-2017.
- [228] X. Li *et al.*, "Layer-by-layer inkjet printing GO film anchored Ni(OH)₂ nanoflakes for high-performance supercapacitors," *Chem. Eng. J.*, vol. 375, p. 121988, Nov. 2019.
- [229] S. H. Park, M. Kaur, D. Yun, and W. S. Kim, "Hierarchically Designed Electron Paths in 3D Printed Energy Storage Devices," *Langmuir*, vol. 34, no. 37, pp. 10897–10904, Sep. 2018.
- [230] Y. Jin, H. Chen, M. Chen, N. Liu, and Q. Li, "Graphene-patched CNT/MnO₂ nanocomposite papers for the electrode of high-performance flexible asymmetric supercapacitors," *ACS Appl. Mater. Interfaces*, vol. 5, no. 8, pp. 3408–3416, Apr. 2013.
- [231] F. Zhang *et al.*, "3D printing technologies for electrochemical energy storage," *Nano Energy*, vol. 40. Elsevier Ltd, pp. 418–431, 01-Oct-2017.